**A Highly Reliable Radio Communication System
for Wireless Sensor and Actuator Networks**

Von der Fakultät für Ingenieurwissenschaften

Abteilung Elektrotechnik und Informationstechnik

der Universität Duisburg-Essen

zur Erlangung des akademischen Grades

Doktor der Ingenieurwissenschaften

genehmigte Dissertation

von

Hamad Fadhel Hamad Naser Alwadaani Aldoseri
aus
Bahrain

Abstract

The reliability of Wireless Sensor and Actuator Networks (WSANs) is an essential aspect of wireless communications. To achieve a robust communication, the reliability of Filter Bank Multicarrier (FBMC) modulation that uses Offset Quadrature Amplitude Modulation (OQAM) is enhanced by spreading as done in the process of Code Division Multiple Access (CDMA). Although, the spectral efficiency is downscaled by the spreading code length, the Bit Error Ratio (BER) of the system is significantly improved by spreading in time or frequency domain.

In this dissertation, a highly reliable WSAN based on spread FBMC is introduced. The selection of FBMC is based on its ability to solve some drawbacks of Orthogonal Frequency Division Multiplexing (OFDM) such as the need of the Cyclic Prefix (CP) and the high Out-Of-Band (OOB) emissions. After the implementation of Frequency Spreading (FS) and Time Spreading (TS) on FBMC, the effects of using different industrial channel models are discussed. It is proven by simulations that real and complex variants of spread FBMC can be used to establish a reliable communication between different nodes of the network.

The joint effect of quantization and clipping of the Analog-to-Digital Converter (ADC) for spread FBMC is also discussed in this thesis. It is shown that an optimal clipping level for the received signal maximizes the Signal-to-Quantization Noise power Ratio (SQNR). Depending on the ADC resolution, an optimal range of clipping levels can be used to minimize the BER.

Subsequently, the performance of spread FBMC in uplink and full-sized downlink under several types of jamming is investigated. When the transmission is attacked by White Gaussian Noise (WGN) methods such as Barrage Noise Jamming (BNJ) and Partial Band Jamming (PBJ), it is proven that spread FBMC outperforms spread OFDM variants. When tone jamming is implemented using time-invariant schemes such as All Tone Jamming (ATJ), Multitone Jamming (MTJ), and Random Multitone Jamming (RMTJ), spread FBMC usually outperforms spread OFDM variants.

However, it is shown that spreading is less effective as the number of targeted resource blocks decreases when the system is targeted by some time-variant tone jamming techniques such as Sweep Multitone Jamming (SMTJ) and Random Frequency Hopping Jamming (RFHJ). When a Carrier Frequency Offset (CFO) is present between the system and the jamming signal, it is shown that spreading, alongside the improvement of the system robustness, decreases the sensitivity of both OFDM and FBMC to the CFO.

A practical implementation of FS-FBMC using the Universal Serial Radio Peripheral (USRP) is also done to verify how the robustness of the FBMC transmission is enhanced by spreading. In addition to the reliability enhancement, it is proven that spreading can be applied to overcome the high Error Vector Magnitude (EVM) of the In-phase/Quadrature (I/Q) demodulator when the received signal power is low.

Kurzfassung

Die Zuverlässigkeit von drahtlosen Sensor- und Aktornetzwerken (WSANs) ist ein wesentlicher Aspekt der drahtlosen industriellen Kommunikation. Um eine robuste Kommunikation zu erzielen, kann die Zuverlässigkeit der Filterbank-Mehrträger(FBMC)-Modulation, die Offset-Quadratur-Amplitudenmodulation (OQAM) verwendet, durch Spreizen verbessert werden, wie es beim Verfahren des Codemultiplex-Mehrfachzugriffs (CDMA) erfolgt. Obwohl die spektrale Effizienz durch die Spreizcodelänge herunterskaliert wird, wird das Bitfehlerverhältnis (BER) des Systems durch Spreizung (Spread) im Zeit- oder Frequenzbereich erheblich verbessert.

In dieser Dissertation wird ein hochzuverlässiges WSAN auf Basis von Spread FBMC vorgestellt. Die Auswahl von FBMC basiert auf seiner Fähigkeit, einige Nachteile des Orthogonal Frequency Division Multiplexing (OFDM) zu lösen, wie z. B. die Notwendigkeit des Cyclic Prefix (CP) und die hohen Out-Of-Band (OOB)-Emissionen. Nach der Implementierung von Frequency Spreading (FS) und Time Spreading (TS) auf FBMC werden die Auswirkungen verschiedener industrieller Kanalmodelle diskutiert. Es wird durch Simulationen nachgewiesen, dass reelle und komplexe Varianten von gespreiztem FBMC verwendet werden können, um eine zuverlässige Kommunikation zwischen verschiedenen Knoten des Netzwerks herzustellen.

Die gemeinsame Wirkung von Quantisierung und Clipping des Analog-Digital-Wandlers (ADC) für gespreiztes FBMC wird ebenfalls in dieser Arbeit diskutiert. Es wird gezeigt, dass ein optimaler Clipping-Pegel für das empfangene Signal das Signal-zu-Quantisierungsrauschleistungsverhältnis (SQNR) maximiert. Abhängig von der ADC-Auflösung kann ein optimaler Bereich für den Clipping-Pegel bestimmt werden, was erlaubt, das BER zu minimieren.

Anschließend wurde die Leistungsfähigkeit von gespreiztem FBMC im Uplink und Full-Size-Downlink unter verschiedenen Störtypen untersucht. Wenn die Übertragung durch White Gaussian Noise (WGN)-Methoden wie Barrage Noise Jamming (BNJ) und Partial Band Jamming (PBJ) angegriffen wird, wurde nachgewiesen, dass Spread FBMC Spread-OFDM-Varianten übertrifft. Bei Störungen unter Verwendung zeitinvarianter Störmethoden wie All Tone Jamming (ATJ), Multitone Jamming (MTJ) und Random Multitone Jamming (RMTJ), übertrifft Spread FBMC in den meisten Fällen Spread OFDM-Varianten.

Es wird jedoch gezeigt, dass das Spreizen weniger effektiv ist, wenn bei reduzierter Anzahl von gestörten Ressourcenblöcken, das System mit einigen zeitvarianten Störungstechniken wie Sweep Multitone Jamming (SMTJ) und Random Frequency Hopping Jamming (RFHJ) angegriffen wird. Wenn ein Trägerfrequenzversatz (CFO) zwischen dem System und dem Störsignal vorhanden ist, zeigt sich, dass das Spreizen neben der Verbesserung der Systemrobustheit die Empfindlichkeit sowohl von OFDM als auch von FBMC gegenüber dem CFO verringert.

Eine praktische Implementierung von FS-FBMC unter Verwendung des Universal Serial Radio Peripheral (USRP) wird ebenfalls durchgeführt, um zu verifizieren, wie die Robustheit der FBMC-Übertragung durch Signalspreizung verbessert wird. Zusätzlich zur Verbesserung der Zuverlässigkeit hat sich gezeigt, dass die Signalspreizung angewendet werden kann, um die hohe Fehlervektoramplitude (EVM) des In-Phase/Quadratur (I/Q)-Demodulators zu reduzieren, wenn die empfangene Signalleistung niedrig ist.

Acknowledgment

Contents

Chapter 1

Introduction

1.1 Motivation

Wireless Sensor and Actuator Networks (WSANs) shown in Figure 1.1 consist of a number of sensors which are considered to be low-power devices with limited computational capabilities. WSANs also have a group of actuators which have higher processing abilities and transmission power as mentioned in [1]. In some cases, sensors and actuators can also operate bidirectionally. Similar to any radio network, some of the main aspects which are considered in the network design are:

- flexible resource allocation in time and/or frequency,

- reliable transmission between different nodes,

- maximize the spectral efficiency,

- minimize the latency.

One of the challenges facing WSANs is to have a reliable communication under jamming. The jamming resistivity is one of the main aspects of the Physical layer (PHY) security in the Electronic Warefare (EW) literature which are summarized as [2]:

- low probability of detection,

- low probability of interception,

- anti-jamming techniques.

The idea behind this work is to establish a reliable anti-jamming communication link based on Filter Bank Multicarrier (FBMC) transmission for industrial applications that can be used to transmit emergency signals in hostile environments.
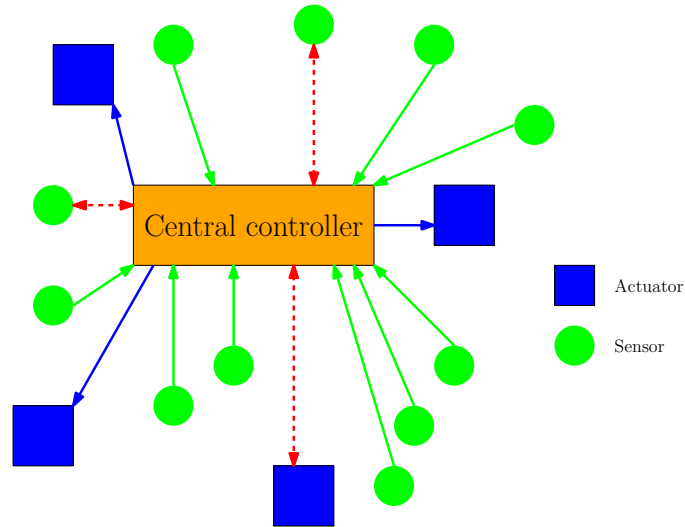
Figure 1.1: WSAN with single (green or blue) and bidirectional (red) transmissions

To create a robust transmission, Orthogonal Frequency Division Multiplexing (OFDM) was combined with Code Division Multiple Access (CDMA) that uses Frequency Spreading (FS) in [3]. As the throughput decreases due to the use of spreading, the reliability of the network is improved in terms of Bit Error Ratio (BER). Since Conventional OFDM has high Out-Of-Band (OOB) emissions as well as the need of a Cyclic Prefix (CP) to eliminate Inter Symbol Interference (ISI), both reliability and spectral efficiency of CDMA-OFDM are improved when FBMC that uses Offset Quadrature Amplitude Modulation (OQAM) is combined with CDMA as shown in [4].

Instead of transmitting real bits in spread FBMC, which can also be called CDMA-OQAM-OFDM, a novel method to restore the complex orthogonality by an optimal code selection from a Walsh-Hadamard (W-H) code matrix was introduced in [5] allowing complex symbols to be transmitted. In [6], it was shown that the reliability is improved under frequency selective channels when Time spreading (TS) was applied on spread FBMC. Also in [6], it was proven that spread FBMC can be applied with Alamouti transmission. In [7], Inter Carrier Interference (ICI) was almost eliminated for multipath fading channels by the implementation of an Alamouti FS scheme. TS Alamouti scheme was applied in [8] and [9] were it provided a significant improvement under a doubly selective channel.

The W-H Transform was used as a linear combiner for the input data in [10] to reduce the loss of spectral efficiency caused by the spreading code. In [11], the W-H transform was applied as a precoder for a Multiple-Input Multiple-Output (MIMO)-FS scheme with a single guard subcarrier. However, the orthogonality is lost when the channel is frequency selective within the spreading band.

Moreover, in spreading applications, the Fast Fourier Transform (FFT) was used to spread data in [12] and [13] to eliminate the intrinsic interference. Discrete Fourier Transform (DFT)-FBMC with FS was introduced as a high efficiency variant in [14] to enhance the FBMC transmission with the advantages of Single Carrier Frequency Division Multiple Access (SC-FDMA). However, some drawbacks such as the need of a high complexity MIMO equalizer and the availability of residual interference are still present.

Jamming attacks are one of the main threats to the operation of communication systems as shown in Figure 1.2 and classified in [15] and [16]. The resiliency in OFDM systems was investigated thoroughly in [17], where it was shown that many intentional and unintentional sources of interference can affect the performance negatively. In [18], closed-forms for the BER of OFDM were obtained when the system was interfered with Barrage Noise Jamming (BNJ), Partial Band Jamming (PBJ) and Multitone Jamming (MTJ). The Power Spectral Density (PSD) of these techniques are shown in Figure 1.3. PBJ attacks were investigated in [19] demonstrating that coding can be useful as a countermeasure against jamming attacks. In [20], the joint effect of nonlinear distortion and PBJ for a Rayleigh fading channel was discussed. MTJ attacks on OFDM were discussed in [21] where it was shown that the BER is proportional to the Jammer-to-Signal power Ratio (JSR) when worst case jamming was applied. Also in [21], it was shown that frequency diversity and channel coding can lower the performance loss caused by the jamming signal. The effects of the previously mentioned jamming techniques on spread FBMC were discussed in [22].
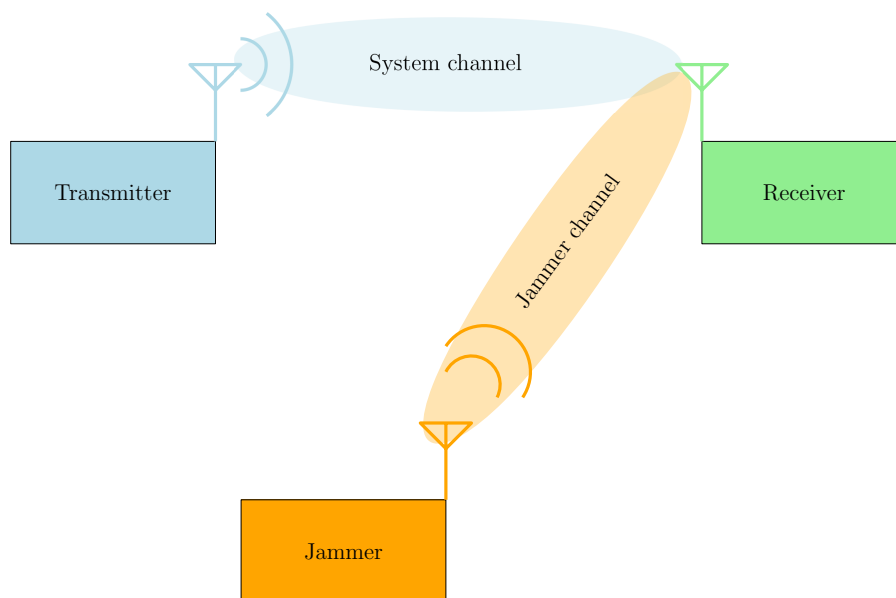

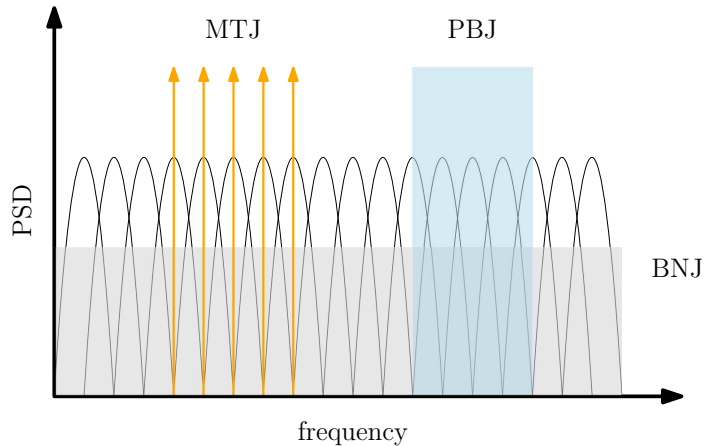Figure 1.2: A transmission chain under jamming attack

Figure 1.3: PSD of BNJ, MTJ and PBJ

Time-variant jamming, such as the methods shown in Figure 1.4, that targets OFDM-based systems was investigated in several studies. The effects of sweep and pulsed jamming were studied in [23], where it was shown that narrow band jamming with a slow sweep increases the BER of the targeted system significantly. It was also found in [23] that pulsed jamming requires a long pulse duration to make a significant distortion at the receiver. In [24], it was proven that Single Off-Tone Jamming (SOTJ) and Multi Off-Tone Jamming (MOTJ), where a Carrier Frequency Offset (CFO) is present between the jamming tones and the OFDM subcarriers, create a higher ICI than a perfectly aligned jamming signal. This is also an advantage of FBMC systems since they are less sensitive to CFO. However, it was proven in [25] that OQAM-OFDM is more sensitive to time-variant perfectly aligned interference tones, although, spreading was used to improve the FBMC reliability so that it usually outperforms spread OFDM [25]. The Automatic Gain Control (AGC) at the receiver can also be targeted by a low duty cycle jammer as discussed in [26]. From the jammer point of view, this can save power and make the detection of the jamming source more difficult as shown in [27].

As discussed in [17], protocol-aware jamming is proven to be more effective than uncorrelated jamming. Time synchronization attacks discussed in [28] are mainly designed to interrupt the symbol timing by the transmission of a false preamble signal which can cancel the timing peak, create a peak in a false location, or cancel the correlation between the preamble halves. For example, the frequency synchronization attack shown in [29] is done by transmitting a preamble with a frequency shift to generate a false frequency estimation. It was also demonstrated in [29], that coarse frequency estimation can be negatively affected by a scrambling attack that changes the phase error between the two halves of the first transmitted symbol.

Examples of equalization attacks were discussed in [17] and [26] as protocol-aware attacks against OFDM transmission. It was proven in [30] that pilot jamming by rising the noise floor of the pilot tone was more effective than BNJ by 2 dB. Pilot nulling attack was also implemented in [30] and was found more effective than BNJ by 7.5 dB.

While the CP is considered to be an essential part of OFDM transmission, it can be targeted by a low duty cycle jamming signal instead of a continuous signal as shown in Figure 1.5. CP jamming, as discussed in [31], was more effective than BNJ when an OFDM receiver that uses a Maximum Likelihood (ML) estimator was attacked.

As a protocol-aware attack, the jamming of control signals can be used as a Denial of Service (DoS) attack against OFDM-based systems. This type of attacks requires a deep knowledge of the targeted system. As an example, the authors in [32] analyzed the components of Long Term Evolution (LTE) uplink and downlink signals to find the easiest way to attack both links. In [33], several attacks on LTE signals were discussed including jamming the Physical Uplink Control Channel (PUCCH) which is used to send hybrid automatic repeat Request acknowledgement, channel quality indicator, and scheduling requests.

(a) Pulsed jamming   (b) Sweep jamming
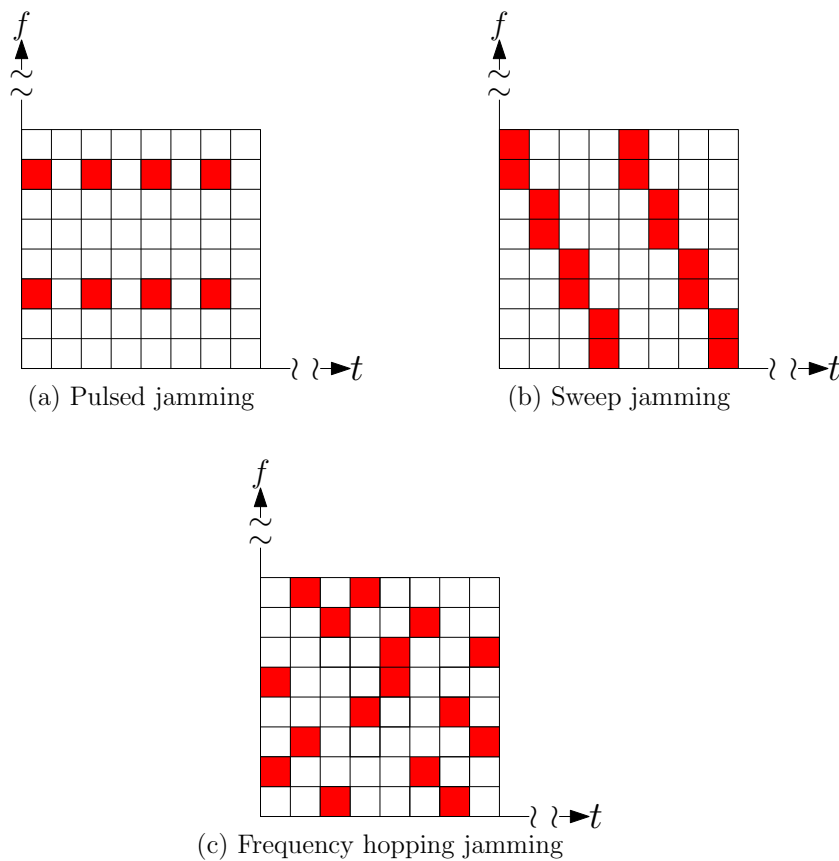
(c) Frequency hopping jamming

Figure 1.4: Some time-variant jamming techniques on a time-frequency lattice
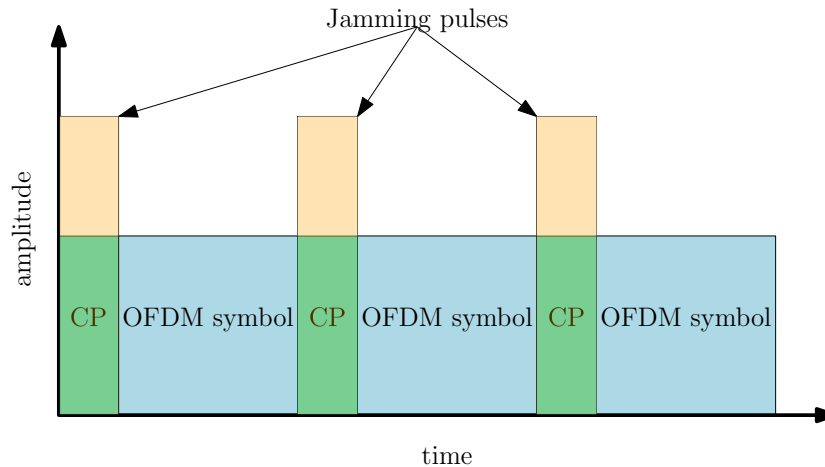
Figure 1.5: CP jamming using a low duty cycle jammer

In addition to the reliability of the spread FBMC communication system, this dissertation focuses on the Analog-to-Digital Converter (ADC) at the receiver side as it is considered to be one of the main sources of non-linearity. Since the sensors are usually low-power devices, lowering the ADC resolution can be used as a power-saving method as long as the Signal-to-Quantization Noise power Ratio (SQNR) varies in an acceptable level.

It was shown in [34–36] that the SQNR of an OFDM receiver can be maximized for a certain ADC resolution and a certain SNR level. This is done by the setting of an optimal clipping level for the received signal. Moreover, for a certain ADC resolution, a maximum SQNR can be obtained using a closed-form expression as shown in [37]. Since spreading is used to improve the reliability of OQAM-OFDM in this thesis, it was proven in [38] that the joint effect of quantization and clipping performed by the ADC in the OFDM receiver can be reduced by frequency diversity when a low-order constellation is implemented. The quantization and clipping effects on FS-FBMC networks were studied in [39], where it was shown that spread FBMC usually outperforms spread OFDM schemes with and without the presence of jamming. However, this work was limited to FS only and did not show how the clipping level has to be optimized for a wide range of Signal-to-Noise power Ratio (SNR) levels.

As this dissertation discusses how spread FBMC systems can be a solution for a reliable transmission in the presence of jamming signals, a practical implementation of spread FBMC is used to validate the theoretical results for its performance under jamming. It was proven in [40] that FBMC can be a good candidate for future wireless networks and problems such as doubly selective channels can be managed practically in many cases by a single-tap equalizer. Furthermore, pilot-aided channel estimation and multiple antenna scenarios for FBMC transmission were also studied in [40].

Several practical implementations of FBMC on Software Defined Radios (SDRs) were discussed in [41]. As the Universal Software Radio Peripheral (USRP) is one of the most common used SDRs, FBMC was implemented on USRP to verify its advantages in [42] and [43]. In this work, the performance of FS-FBMC under jamming is evaluated practically using USRP radios as published in [44].

1.2   Contribution and Thesis Outline

This work investigates the use of spread FBMC as a candidate for a reliable industrial WSAN. The dissertation covers several novel research aspects that can be summarized in:

- the reliability of spread FBMC under several industrial propagation channels in the presence of jamming signals,

- the quantization and clipping effects on spread FBMC.

- a practical implementation for spread FBMC under the influence of MTJ.

To arrive at corresponding results, four master theses and two bachelor projects were co-supervised. The scientific contribution done in the qualification phase consists of a journal article and three conference papers which are organized by the time of the publication as:

- H. Aldoseri, L. Häring, and A. Czylwik, "A reliable industrial wireless sensor and actor network based on CDMA-OQAM-OFDM," in *IEEE 31st Annu. Int. Symp. Pers., Indoor, and Mobile Radio Commun. (PIMRC)*, London, United Kingdom, Aug. 2020, pp. 1714–1718. The paper compared spread FBMC and spread OFDM variants under the presence of BNJ, PBJ, and MTJ. Similar to the results in chapter 4, spread FBMC usually outperforms spread OFDM for the investigated propagation scenarios.

- H. Aldoseri, L. Häring, and A. Czylwik, "On the reliability of spread FBMC systems for off-tone jamming," in *IEEE 32nd Annu. Int. Symp. Pers., Indoor, and Mobile Radio Commun. (PIMRC)*, Oulu, Finland, Sep. 2021, pp. 1329–1333. This paper demonstrated that spread FBMC usually outperforms spread OFDM variants when both are attacked by an off-tone jamming signal. The same conclusions were achieved by the work done in chapter 4.

- H. Aldoseri, L. Häring, and A. Czylwik, "Analysis of ADC quantization and clipping effects on CDMA-OQAM-OFDM based WSAN," in *Int. J. of Interdisciplinary Telecommun. and Netw. (IJITN)*, vol. 14, no. 1, 2022. The effects of ADC quantization and clipping effects on spread FBMC were discussed in this paper as done in chapter 3.

- H. Aldoseri, T. Wu, and A. Czylwik, "A practical implementation of spread FBMC in a multitone jamming scenario using USRP radios" in *15th Int. Congr. Ultra Modern Telecommun. and Control Syst. and Workshops (ICUMT)*, Ghent, Belgium, Nov. 2023, pp. 81–84. This paper includes a summary of the work done in chapter 5 which shows the improvement made by spreading to the FBMC transmission practically.

The following chapters of this dissertation are described as follows.

In chapter 2, a detailed survey of the Multicarrier (MC) modulation is discussed followed by a review on OFDM and FBMC. This is followed by a description of the spread FBMC system model which is applied in this thesis. The chapter also includes a performance analysis of spread FBMC under several industrial propagation channels.

Chapter 3 discusses the effects of clipping and quantization, caused by the ADC at the receiver, on the performance of the spread FBMC transmission under industrial propagation channels. The performance of spread FBMC under several types of jamming is investigated in chapter 4. In this chapter, a high SQNR was ensured by the adjustment of the clipping level at the receiver to minimize the error caused by the ADC.

In chapter 5, the reliability of spread FBMC under jamming was proven practically by an implementation using USRP radios. Finally, in chapter 6, the dissertation concludes that spread FBMC can be a candidate for a reliable industrial WSAN. Many open issues for further research are also mentioned.

Chapter 2

Theoretical Background

This chapter starts with a description of MC modulation techniques. Due to its ability to ensure a high spectral efficieny and a low-complexity discrete implementation, the basic theory of OFDM is discussed. However, conventional OFDM's need for a CP and high OOB emissions are drawbacks that require a solution. Therefore, FBMC is investigated as a solution with a focus on OQAM-OFDM. This is followed by a discussion of spread FBMC techniques, followed by a demonstration of the spreading gain in industrial environments.

2.1 Multicarrier Modulation

For a more flexible resource allocation, MC modulation has been introduced since the late 1950s for military High Frequency (HF) radios [45]. As mentioned in [46], some early works were also done in [47] and [48]. In MC modulation, the system bandwidth B_{s} is divided into subchannels as shown in Figure 2.1. This shows the magnitude of the Channel Transfer Function (CTF) $|H_{\mathrm{s}}(f)|$, where $|\,|$ is the absolute value operator and f is the frequency. The number of subcarriers N is selected to ensure the flatness of the fading at each subchannel. This requires the subchannel bandwidth $B_n = B_{\mathrm{s}}/N$, where $n \in 0, 1, \cdots, N-1$ is the subchannel index, to be less than the coherence bandwidth of the channel B_{c} as:

$$B_n \ll B_{\mathrm{c}}. \tag{2.1}$$

Similarly, the throughput R of the MC transmitter shown in Figure 2.2 where the initial binary data $\mathbf{d}$ are divided on N branches by the Serial-to-Parallel (S/P) converter. The throughput per subcarrier R_n is calculated by:
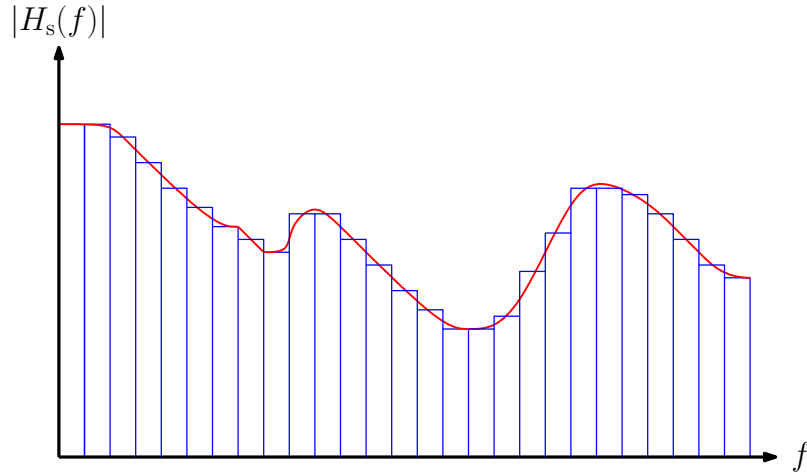
$$R_n = \frac{R}{N}. \tag{2.2}$$

Figure 2.1: The division of a transmission channel (red) into subchannels (blue)

In any branch, the parallel signal $d_{n,m}$, where m is the time sample index for the sampling time T_{s}, is digitally modulated by a mapper. The resultant modulated signal $d'_{n,m}$ is usually a Quadrature Amplitude Modulation (QAM) signal or a Phase Shift Keying (PSK) signal. This is followed by the conversion of the modulated signal to an analog signal $s_{\mathrm{a},n}(t)$ by the Digital-to-Analog Converter (DAC). Afterwards, a Pulse Shaping Filter (PSF) with a pulse shaping function $g(t)$ and a bandwidth of B_n is used to generate the complex-valued baseband subchannel signal $s_n(t)$ as:

$$s_n(t) = s_{\mathrm{a},n}(t) * g(t) , \tag{2.3}$$

where $*$ is the convolution operator and the PSF is assumed to have the same $g(t)$ for all branches. Later on, the resultant filtered signals $s_n(t)$ are upconverted and sent through the wireless channel. The transmitted MC signal $s(t)$ is obtained by:

$$s(t) = \sum_{n=0}^{N-1} \left[\Re\left\{s_n(t)\right\} \cos(2\pi f_n t + \theta_n) - \Im\left\{s_n(t)\right\} \sin(2\pi f_n t + \theta_n) \right] , \tag{2.4}$$

where f_n is the n-th subcarrier frequency, θ_n is the phase offset the n-th subcarrier, $\Re\{\,\}$ is the real part, and $\Im\{\,\}$ is the imaginary part. Since this basic topology needs guard bands between subcarriers, the spectral efficiency is reduced. However, the subcarriers can overlap if they are orthogonal so that the receiver can separate them correctly.

As the symbol rate for each subcarrier is less than the input symbol rate, the effect of the delay spread of the transmission channel is reduced. This reduction results in a significant reduction of the ISI. To achieve this, the symbol duration T_{sym} needs to be set as:

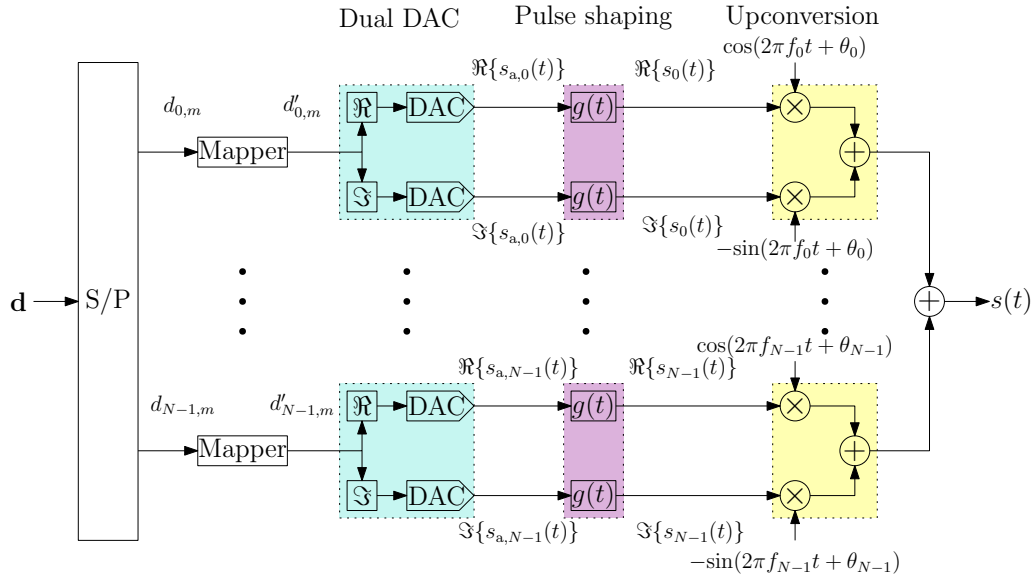$$T_{\mathrm{sym}} \gg T_{\mathrm{max}} , \tag{2.5}$$

Figure 2.2: Basic MC transmitter

where the maximum delay spread of the channel T_{max} is approximated by:

$$T_{\mathrm{max}} \approx \frac{1}{B_{\mathrm{c}}} \, . \tag{2.6}$$

The MC signal is then sent through a wireless channel with the Channel Impulse Response (CIR) of $h_{\mathrm{s}}(t)$. When the channel is assumed to be affected by Additive White Gaussian Noise (AWGN), the received MC signal $r(t)$ can be represented as:

$$r(t) = s(t) * h_{\mathrm{s}}(t) + w(t) \, , \tag{2.7}$$

where $w(t)$ is the AWGN. At the basic MC receiver shown in Figure 2.3, the received MC signal is filtered by N Bandpass Filters (BPFs). The center frequency of each filter is set to be equal to the upconversion (UC) frequency of each subcarrier. If the subcarriers are overlapped as done in [49], the downconversion (DC) is done before filtering by a pulse shaping function of $g^{*}(-t)$, where $(\,)^{*}$ is the complex conjugate operator. After the DC of the filtered signals $r_{\mathrm{bpf},n}(t)$, the downconverted signals $r_{\mathrm{dc},n}(t)$ are filtered by Low-Pass Filters (LPFs). The filtered signals $r_{\mathrm{f},n}(t)$ are digitalized by the ADCs. Afterwards, the digital signals $r_{\mathrm{d},n,m}$ are detected. The detected real signals $\hat{d}_{n,m}$ are then converted by the Parallel-to-Serial (P/S) converter to get the serial binary data $\hat{\mathbf{d}}$.

As the channel is almost flat for each subcarrier, some weak subcarriers may have a high degradation in performance, thus, a high BER per subcarrier. Several techniques can be applied to overcome this problem as discussed in [49] such as frequency equalization where the CTF per subcarrier is compensated. However, as the noise on the equalized subcarrier is also multiplied by the same factor, the SNR is not improved by the equalization process.
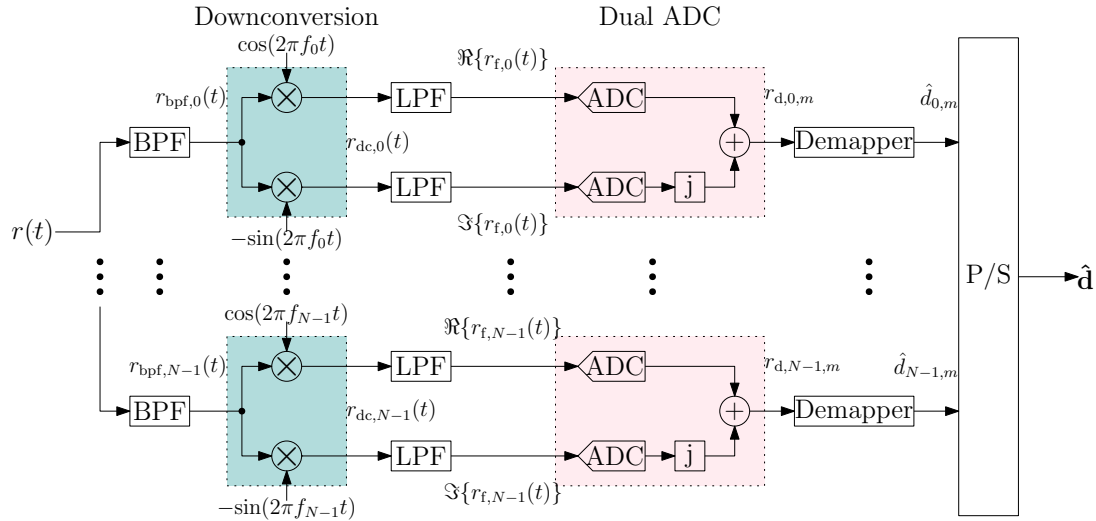
Figure 2.3: Basic MC receiver

The mitigation of the frequency flat fading at each subcarrier can be done in the transmitter instead of the receiver by the implementation of precoding as done in [50]. This can also be done by adaptive loading where more bits are allocated to the better subcarriers, in terms of SNR, as introduced in [51]. However, these techniques require prior knowledge of the transmission channel. Another solution to overcome the individual subcarrier fading is the implementation of coding and interleaving as discussed in [52–54]. Although, the probability of the correct decoding of the received codeword depends on the number of subcarriers with high SNR levels.

Although the MC transmission provides a good solution to the multipath fading problem, it has a number of disadvantages that limit its performance as follows:

- the spectral efficiency is relatively low if the subcarriers are not overlapped,

- a high number of modulators/demodulators as well as other hardware elements (filters, ADCs, DACs, ..) are required to realize the system practically,

- the Peak-to-Average Power Ratio (PAPR) is proportional to the number of subcarriers and the ADC resolution needs to be increased in most cases,

- a high sensitivity to time and frequency offsets.

The following section shows how to reduce the hardware complexity and improve the spectral efficiency by the implementation of OFDM.

2.2   Orthogonal Frequency Division Multiplexing

As mentioned in the previous section, the overlapping of subcarriers can be done if the subcarriers are orthogonal to each other to enhance the spectral efficiency of the MC transmission. For a number of periodic cycles with a duration of $T_{\mathrm{N}} = NT_{\mathrm{s}}$, this is done by setting the subcarrier spacing Δf to a multiple of $\frac{1}{T_{\mathrm{N}}}$. The earliest works on orthogonal frequency subcarriers, as investigated in [55], can be backtraced to several military projects [56–58] while the OFDM patent [59] was issued in 1970.

Another disadvantage of the conventional MC transmission is the large number of hardware needed to realize the system practically. An affordable solution to this problem was discussed in [60] by the application of the DFT and the Inverse Discrete Fourier Transform (IDFT) to the MC transmission chain. This allows the cancellation of the ICI due to the fact that at the frequency of the peak of any subcarrier, the amplitudes of all other subcarriers are equal to zero. To reduce the mathematical complexity of the DFT/IDFT, the FFT and the Inverse Fast Fourier Transform (IFFT) are implemented as discussed in [61].

In the OFDM transmitter shown in Figure 2.4, a stream of mapped data $\mathbf{d'}$ are converted to a parallel signal by the S/P converter as done previously in the MC transmitter. Afterwards, the IFFT is applied on the parallel streams $d'_{n,m}$ over N-points so that the output for the mth OFDM symbol $x_m[i]$ is given by:

$$x_m[i] = \frac{1}{\sqrt{N}} \sum_{n=0}^{N-1} d'_{n,m} \mathrm{e}^{\frac{\mathrm{j}2\pi ni}{N}} \text{ , for } i = 0, 1, \cdots, N-1 \,, \tag{2.8}$$

where i is the discrete time index for the OFDM symbol which is sampled at $mT_{\mathrm{N}}+iT_s$. As the multipath channel causes a temporal spread at the receiver, a guard time T_{G} between OFDM symbols that contain the transmitted data is needed to avoid ISI. Therefore, the resultant OFDM symbol duration is extended from T_{N} to $T_{\mathrm{sym}} = T_{\mathrm{N}} + T_{\mathrm{G}}$.
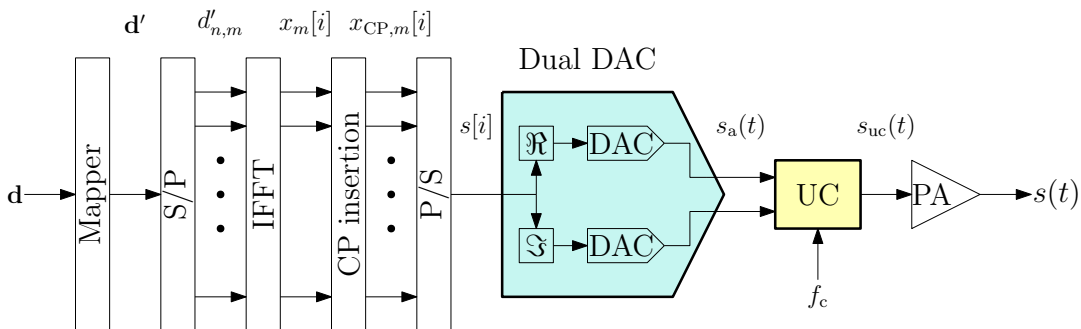

Figure 2.4: OFDM transmitter

One of the possibilities of the guard interval application is to send zeros on the guard interval which is called Zero Padding (ZP) as done in [62]. When ZP is applied as illustrated in Figure 2.5 (a), the signal can be recovered correctly on the channel zero locations [62]. However, a more complicated receiver is needed than the conventional DFT receiver as done in [63, 64]. Therefore, as done recently in [65], ZP can be effective for non-orthogonal systems such as Spectrally Efficient Frequency Division Multiplexing (SEFDM). A major ZP drawback is that the SNR decreases since the channel noise is present without any useful signal at the ZP duration [49].

Another method is to apply CP, which is a copy of the last part of the OFDM symbol, to the front of it as shown in Figure 2.5 (b). In [66], it was proven that when the CP duration $T_{\mathrm{CP}} \geq T_{\max}$, the ISI is avoided as the OFDM signal is recovered correctly after the optimal application of the FFT window. By the CP insertion, the extended OFDM symbol $x_{\mathrm{CP},m}[i]$ is obtained by:

$$x_{\mathrm{CP},m}[i] = x_m[N - N_{\mathrm{CP}}], x_m[N - N_{\mathrm{CP}} + 1], \cdots, x_m[N - 1], x_m[0], x_m[1], \cdots, x_m[N - 1],$$
(2.9)

where $N_{\mathrm{CP}} = \frac{NT_{\mathrm{CP}}}{T_{\mathrm{N}}}$ is the CP length. The extended OFDM symbol is then converted to the complex-valued serial digital OFDM signal $s[i]$ by the P/S converter. The resultant signal is converted to an analog signal by the DAC. Later on, the analog signal is upconverted by the carrier frequency f_{c}. This is followed by a power amplification stage where the upconverted signal $s_{\mathrm{uc}}(t)$ is amplified by the Power Amplifier (PA). At the end of the transmitter path, the amplified signal is transmitted through the system channel.
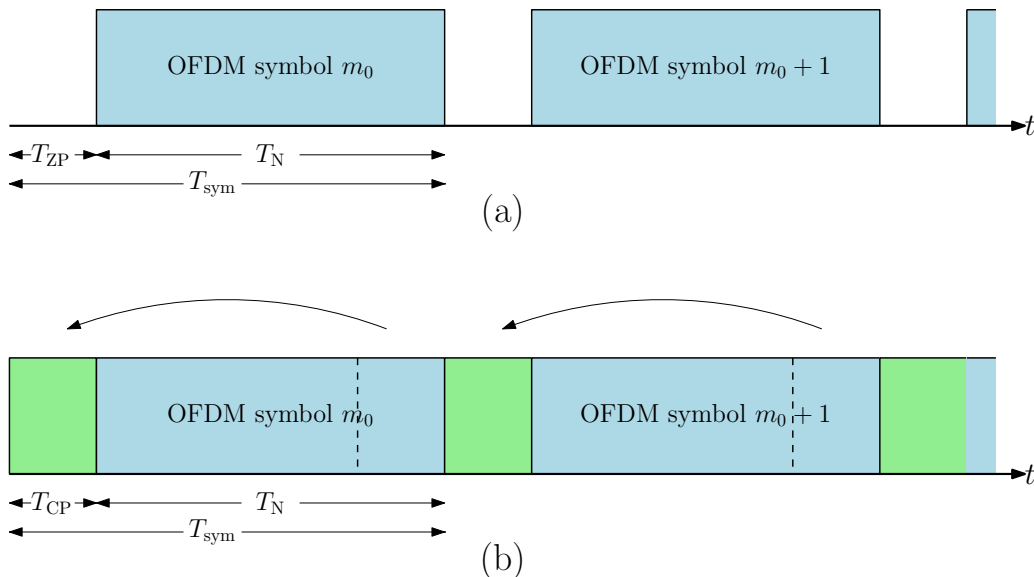

Figure 2.5: OFDM transmission with ZP (a) and CP (b)

In the receiver shown in Figure 2.6, the received signal is regulated by the AGC. The regulated signal $r_{\text{gc}}(t)$ is then downconverted and filtered. The filtered signal is converted to a digital signal by the ADC. The CP is later removed to have the received OFDM serial signal $y[i]$. If the channel is assumed to be known, this signal can be described by a circular convolution between the transmitted signal and the sampled CIR $h_{\text{s}}[i]$ instead of the linear convolution as:

$$y[i] = s[i] \circledast h_{\text{s}}[i] + w[i] \,, \tag{2.10}$$

where $\circledast$ is the circular convolution operator. The digital serial signal is converted to parallel by the S/P converter. Then, FFT is performed on the parallel signal. The FFT output $y_{n,m}$ is obtained by:

$$y_{n,m} = \frac{1}{\sqrt{N}} \sum_{i=0}^{N-1} y_m[i] \mathrm{e}^{\frac{-\mathrm{j}2\pi ni}{N}} \,, \tag{2.11}$$

where $y_m[i]$ is the sampled received signal $y[i]$ at $mT_{\text{sym}} + iT_s$. The FFT output can be equalized by Zero Forcing (ZF). This is done by the division by the CTF $H_{\text{s},n,m}$ [67]:

$$\hat{y}_{n,m} = \frac{y_{n,m}}{H_{\text{s},n,m}} \,. \tag{2.12}$$

The output of the equalizer is then converted to serial by the P/S converter and demapped to obtain the received data.

As it has been shown that the CP is an effective way to overcome the multipath fading, it also has some implementation problems. If $T_{\text{CP}} < T_{\text{max}}$, the transmission is affected by ISI. ICI can also be present with or without ISI if $T_{\text{CP}} > T_{\text{max}}$ and the FFT window starts after the CP reception as discussed in [66, 68]. The CP also increases the power consumption compared to the ZP. However, CP requires less clipping at the PA than ZP as discussed in [62].
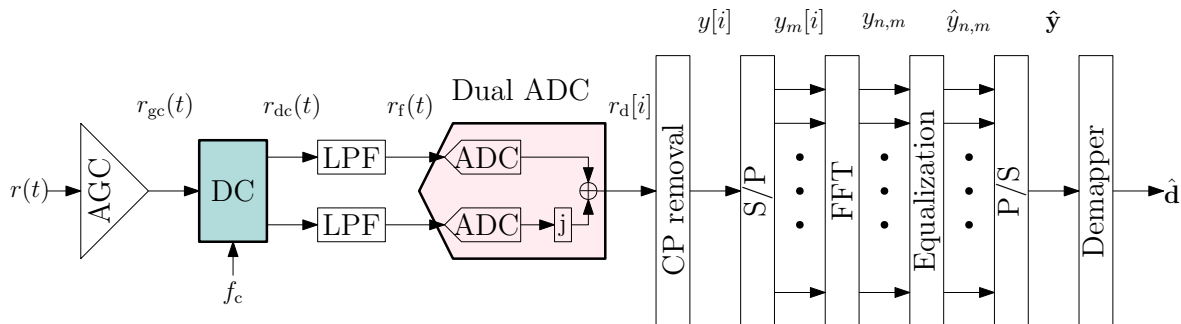
Figure 2.6: OFDM receiver

In general, either with CP or ZP, the spectral efficiency of the OFDM transmission is reduced under multipath environments due to the need of the guard interval. This is considered as one of the major drawbacks for OFDM.

Since each subcarrier is assumed to be multiplied by a rectangular-shaped time window with a length of T_N in time domain at the transmitter, the spectrum of the transmitted OFDM signal is a sum of sinc functions which are shifted by $\frac{1}{T_\mathrm{N}}$ if the minimum frequency spacing is applied. This causes high OOB emissions that affect the neighboring channels negatively because the amplitude spectrum of the sinc function decreases slowly as shown in Figure 2.7.

As the high OOB power is one of the major disadvantages related to the structure of the OFDM signals, the allocation of guard bands that separate the OFDM signal from the neighboring channels has to be considered. However, the spectral efficiency is reduced due to the reduction of the bandwidth which is allocated for data transmission. Another solution is to apply a window that has a more rapid decrease of the amplitude spectrum than a rectangular window. One of the most often used windows to reduce the OOB emissions is the Raised Cosine (RC) window $w_\mathrm{RC}(t)$ which is defined as [55]:
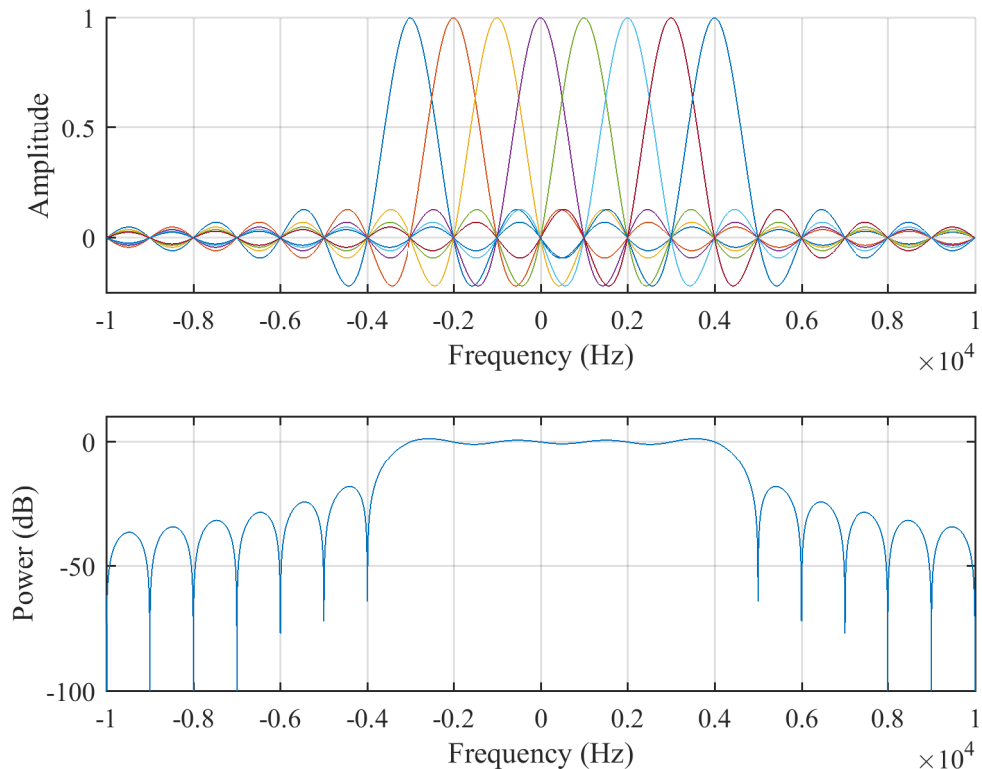
Figure 2.7: OFDM spectrum for 8 subcarriers, $\Delta f{=}1\mathrm{kHz}$

$$w_{\mathrm{RC}}(t) = \begin{cases} \frac{1}{2}\left[1 + \cos\left(\pi + \frac{\pi t}{\beta_{\mathrm{R}} T_{\mathrm{sym}}}\right)\right], & 0 \leq t \leq \beta_{\mathrm{R}} T_{\mathrm{sym}} \\ 1, & \beta_{\mathrm{R}} T_{\mathrm{sym}} \leq t \leq T_{\mathrm{sym}} \\ \frac{1}{2}\left[1 + \cos\left(\pi + \frac{\pi(t - T_{\mathrm{sym}})}{\beta_{\mathrm{R}} T_{\mathrm{sym}}}\right)\right], & T_{\mathrm{sym}} \leq t \leq (1 + \beta_{\mathrm{R}}) T_{\mathrm{sym}}, \end{cases} \tag{2.13}$$

where β_{R} is the roll-off factor of the RC window. As β_{R} increases, the OOB emissions decrease as shown in Figure 2.8. However, this also has a negative effect on the spectral efficiency since the time window increases by $T_{\mathrm{RC}} = \beta_{\mathrm{R}}(T_{\mathrm{N}} + T_{\mathrm{CP}})$. This increment is not used for data transmission as shown in Figure 2.9.

Another drawback of the conventional OFDM system is the sensitivity to the Time Offset (TO) Δm_{s} or CFO Δn_{s} between the transmitter and the receiver as shown in Figure 2.10 for a wide range of SNR γ_{sn} which is obtained by:

$$\gamma_{\mathrm{sn}} = \frac{\mathrm{E}\{|s(t) * h_{\mathrm{s}}(t)|^2\}}{\mathrm{E}\{|w(t)|^2\}}, \tag{2.14}$$

Figure 2.8: PSD of filtered OFDM, Δf=1kHz
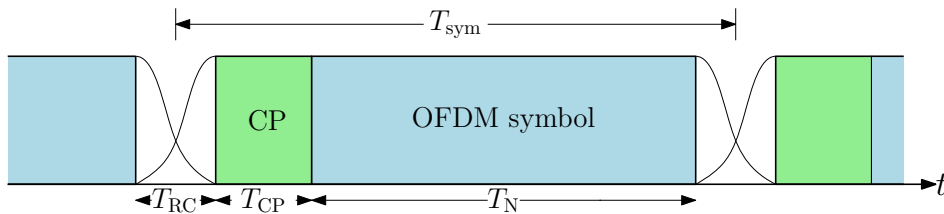
Figure 2.9: Time representation of filtered OFDM

where E{ } is the expectation operator. The CFO correction can be achieved by implementing pilot-aided synchronization [69, 70] or bl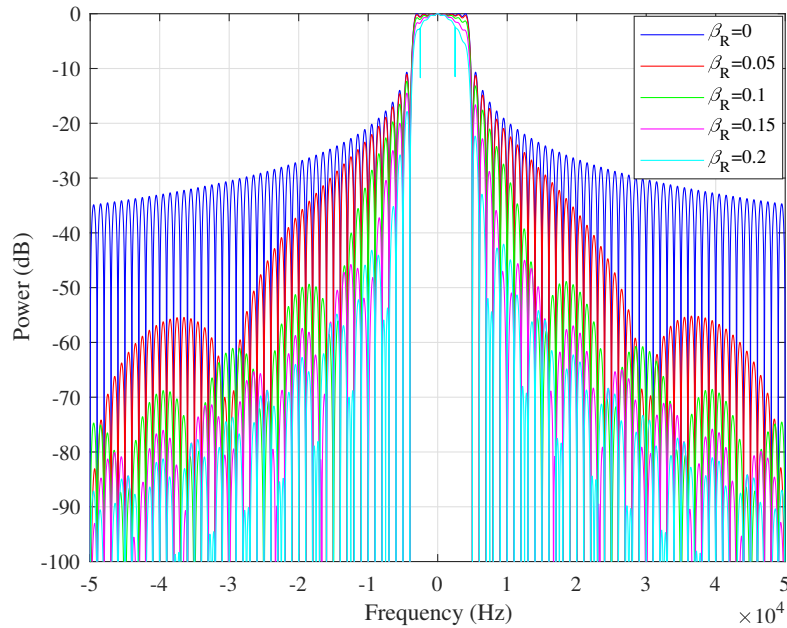ind synchronization, as done in [71, 72], which does not require additional pilots. Similarly, an accurate time synchronization is required between the transmitter and the receiver. To correct the TO, some reference symbols, which are known at the receiver, can be added before the data frames to allocate the start of the frames as done in [70] where an ML estimation was used. However, another stage of offset correction may be needed to do fine time synchronization as done in [73]. The dependency of OFDM transmission on an accurate time and frequency estimation usually causes a further loss in the spectral efficiency. To reduce this loss, CP was used to estimate the CFO in [74] if the transmission is perfectly synchronized in time. However, this can only be achieved if $\Delta n_{\mathrm{s}} \leq 0.5$.

In addition to the previously mentioned drawbacks, OFDM systems suffer from a high PAPR η of the transmitted signal which is given by:

$$\eta = \frac{\max\{|s(t)|^2\}}{\mathrm{E}\{|s(t)|^2\}} \, . \tag{2.15}$$

It is known that a high PAPR can force the PA to operate non-linearly and needs a high ADC resolution to maximize the SQNR. Therefore, some solutions such as coding [75, 76], clipping [77], and DFT-spreading [78] were suggested to minimize the PAPR effect.

Figure 2.10: CFO and TO effects on OFDM transmission using QPSK modulation for AWGN, N=32

2.3   Filterbank Multicarrier Modulation

In the previous section, the disadvantages of OFDM systems show that a more spectrally efficient transmission is needed to cope with the rece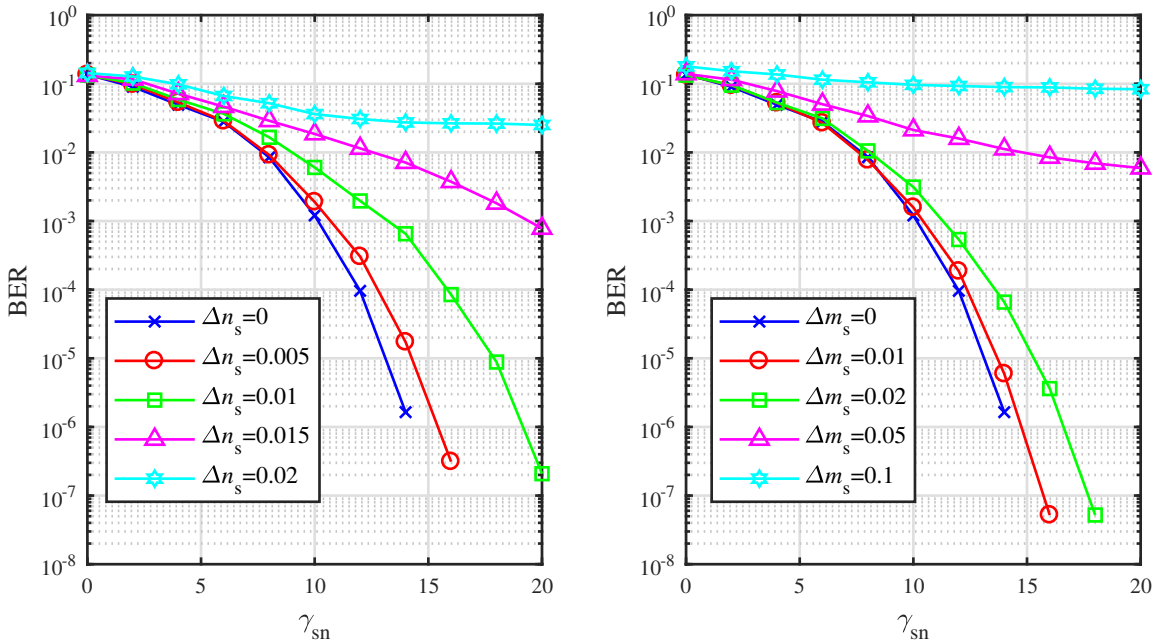nt fast-growing demands of wireless communications. Therefore, FBMC was introduced as an alternative transmission technique to overcome the shortcomings of OFDM as shown in [79] where it was proven that FBMC is more suitable to the Internet of Things (IoT) applications.

FBMC modulation consists of a block of identical filters in the transmitter to filter the data on each subcarrier separately. At the receiver, a block of filters is used to recover the received signal before performing the FFT or IFFT. As the history of FBMC explained in [80], the earliest FBMC models can be backtraced to [47] in the mid 1960s where parallel filters were used to transmit Pulse Amplitude Modulation (PAM) signals using a Vestigial Sideband (VSB) transmission on an ICI/ISI-free channel. Moreover in [47], the spectral efficiency improved as the subcarrier spacing was set to half of the symbol rate. In [81], it was shown that when the work in [47] was expanded to operate on Double Sideband (DSB), the transmission had a higher throughput over the same bandwidth. However, the practical implementation was complicated.

After the DFT implementation of an OFDM system in [60] which reduced the complexity significantly, the polyphase digital implementation of FBMC was first introduced in [82] where it was shown that the DFT implementation to a 60-subcarrier transmission system reduced the computational complexity and gave better results as the number of subcarriers was close to a power of 2. Several improvements were done to the previous work in the 1970s as shown in [83].

2.3.1   FBMC-QAM

In the basic FBMC transmission chain shown in Figure 2.11, where M QAM symbols are sent, the digital output of the FBMC transmitter is given by:

$$s[i] = \sum_{m=0}^{M-1} \sum_{n=0}^{N-1} d'_{n,m} g_{\mathrm{T}}[i] \mathrm{e}^{\frac{\mathrm{j}2\pi ni}{N}} \, , \tag{2.16}$$

where $g_{\mathrm{T}}[i]$ is the transmitter prototype filter impulse response. If an ideal channel is assumed alongside an optimal DAC/ADC operation, the transmitted mapped symbols are perfectly received if the orthogonality is satisfied as [80]:

$$\langle g_{\mathrm{T},n}[i - mN], g_{\mathrm{R},n'}[i - m'N] \rangle = \sum_{i=-\infty}^{\infty} g_{\mathrm{T}}[i - mN] \mathrm{e}^{\frac{\mathrm{j}2\pi ni}{N}} g_{\mathrm{R}}^{*}[i - m'N] \mathrm{e}^{\frac{-\mathrm{j}2\pi n'i}{N}} = \delta_{nn'} \delta_{mm'} \, ,$$

$$\tag{2.17}$$
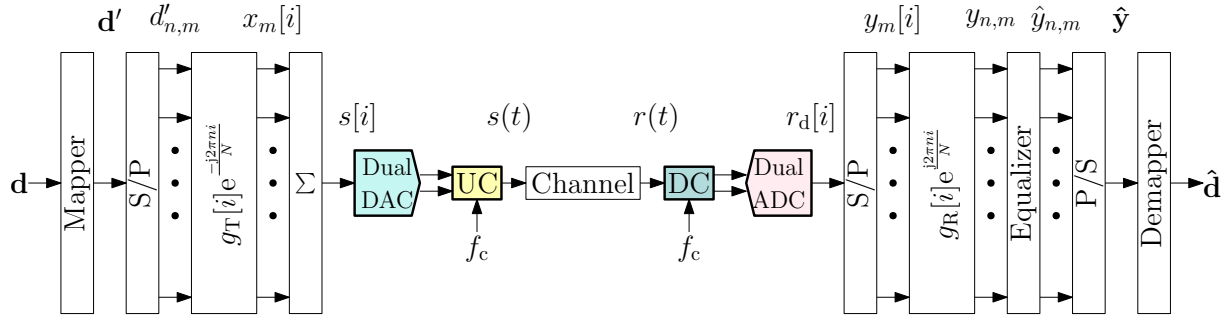
Figure 2.11: Basic FBMC transmission chain

where $g_R[i]$ is the receiver prototype filter impulse response and $\delta_{nn'}$ is the Kronecker delta function which is represented by:

$$\delta_{nn'} = \begin{cases} 1, & n = n' \\ 0, & n \neq n'. \end{cases} \tag{2.18}$$

As discussed in [40], [52], and [80], the transmitter and the receiver filters impulse responses are chosen to be matched so that the filter impulse response $g[i] = g_T[i] = g_R[-i]$ is a symmetric function. Also at the receiver, the received symbol is affected by the interference caused by its neighboring symbols in the frequency-time lattice. Assuming an ideal channel ($H_{s,n,m} = 1$), the interference for the mapped symbol $d'_{n',m'}$ can be obtained by:

$$\sum_{\substack{i=-\infty \\ n' \neq n \\ m' \neq m}}^{\infty} d'_{n',m'} g[i - mN] g^*[i - m'N] e^{\frac{-j2\pi(n-n')i}{N}}. \tag{2.19}$$

To minimize the interference caused by the neighboring symbols, a proper design of the prototype filter need to be done to minimize:

- intrinsic interference caused by the energy distribution in time domain,

- OOB emissions caused by the energy distribution in frequency domain.

Therefore, the time dispersion of the prototype filter σ_i is defined by [84]:

$$\sigma_i = \sqrt{\sum_{i=-\infty}^{\infty} (i - \bar{i})^2 |g[i]|^2}, \tag{2.20}$$

where $\bar{i}$ is obtained by [40]:

$$\bar{i} = \sum_{i=-\infty}^{\infty} i |g[i]|^2. \tag{2.21}$$

and the frequency dispersion σ_{n} is defined by [84]:

$$\sigma_{\mathrm{n}} = \sqrt{\sum_{n=-\infty}^{\infty} (n - \bar{n})^2 |G[n]|^2} \,, \tag{2.22}$$

where $\bar{n}$ is given by [40]:

$$\bar{n} = \sum_{n=-\infty}^{\infty} n|G[n]|^2 \,, \tag{2.23}$$

and $G[n]$ is the frequency response of the prototype filter which is given by [40]:

$$G[n] = \sum_{i=-\infty}^{\infty} g[i] \mathrm{e}^{-\mathrm{j}2\pi ni} \,. \tag{2.24}$$

In terms of time and frequency dispersions, the Heisenberg-Gabor uncertainty parameter ξ gives a measure of the filter localization in the time-frequency lattice as discussed in [85,86]. It can be represented as [84]:

$$\xi = \frac{||g[i]||^2}{4\pi\sigma_{\mathrm{i}}\sigma_{\mathrm{n}}} \leq 1 \,, \tag{2.25}$$

where $|| \; ||$ is the Euclidean norm. The ratio between the time dispersion and the frequency dispersion is defined as the direction parameter ϵ of the prototype filter which is given by [87]:

$$\epsilon = \frac{\sigma_{\mathrm{i}}}{\sigma_{\mathrm{n}}} \,. \tag{2.26}$$

To find the correlation in the time-frequency lattice, the ambiguity function $A_{\mathrm{g}}(\tau, \nu)$ of the prototype filter $g[i]$ is defined as [80]:

$$A_{\mathrm{g}}(\tau, \nu) = \sum_{i=-\infty}^{\infty} g\left[i - \frac{\tau}{2}\right] g^*\left[i + \frac{\tau}{2}\right] \mathrm{e}^{-\mathrm{j}2\pi\nu\tau} \,, \tag{2.27}$$

where ν is the frequency shift and τ is the time shift. As explained in [84], the ambiguity function gives a good measure for the filter's robustness against ICI and ISI. In terms of the ambiguity function, the orthogonality condition is given by [80]:

$$A_{\mathrm{g}}(m'N, n'/N) = \begin{cases} 1, & m' = n' = 0 \\ 0, & \text{otherwise.} \end{cases} \tag{2.28}$$

Due to its ability to transmit complex QAM symbols, many references [40,80] classify this type as a FBMC-QAM system. Conventional OFDM is considered as a variant of this type by applying the rectangular function at both ends. Hermite filters [88] or Isotropic Orthogonal Transform Algorithm (IOTA) filters [52] can also operate as prototype filters in FBMC-QAM systems.

2.3.2   FBMC-OQAM

In [89], the FBMC modulation using OQAM was implemented by DFT providing a major reduction of the computational complexity compared to the earlier FBMC work in [47]. Instead of complex symbols, real symbols were transmitted. To maintain a high throughput, equal to the throughput of an OFDM system without CP as done in [90–92], the symbol rate is doubled at the transmitter shown in Figure 2.12 under special conditions which are achieved through the OQAM processing. Similarly, the frequency spacing between adjacent subcarriers can be halved what doubles the number of subcarriers for the same channel as done in [80] and [82].

The real OQAM symbols $d''_{n,k}$, where k is the OQAM symbol index at a sampling period of $T_s/2$, are generated as illustrated in Figure 2.13 by the staggering of M complex QAM symbols so that the total number of OQAM symbols $K = 2M$. Since the sampling rate is doubled in OQAM modulation, the transmission duration remains constant. The odd OQAM symbols can be represented as:

$$d''_{n,2m+1} = \begin{cases} \Im\{d'_{n,m}\}\phi_{n,2m+1}, & n \in N_e \\ \Re\{d'_{n,m}\}\phi_{n,2m+1}, & n \in N_o, \end{cases} \tag{2.29}$$

where $N_e = \{0, 2, \cdots, N-2\}$ is the set of even subcarriers, $N_o = \{1, 3, \cdots, N-1\}$ is the set of the odd subcarriers, and $\phi_{n,2m+1}$ is a phase shift. Similarly, the even OQAM symbols are generated using a phase shift of $\phi_{n,2m}$ as:

$$d''_{n,2m} = \begin{cases} \Re\{d'_{n,m}\}\phi_{n,2m}, & n \in N_e \\ \Im\{d'_{n,m}\}\phi_{n,2m}, & n \in N_o. \end{cases} \tag{2.30}$$

The phase shift $\phi_{n,k}$ is applied to ensure the phase separation between real and imaginary symbols on the time-frequency lattice shown in Figure 2.14. Together, the process of staggering real symbols and the phase shift is called the OQAM pre-processing [93].
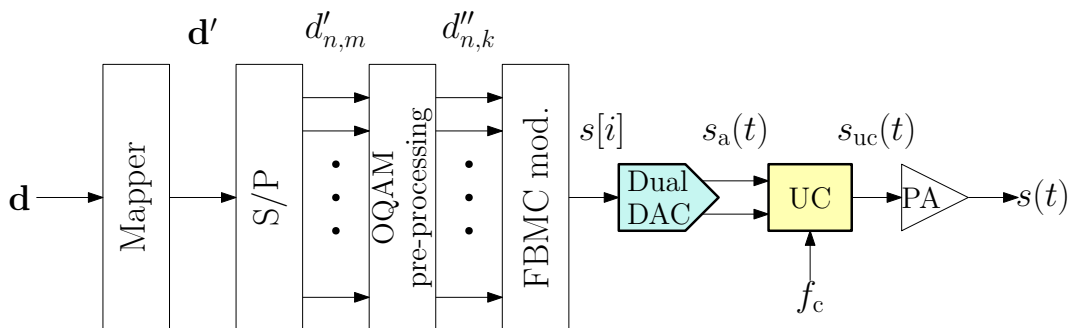

Figure 2.12: FBMC-OQAM transmitter
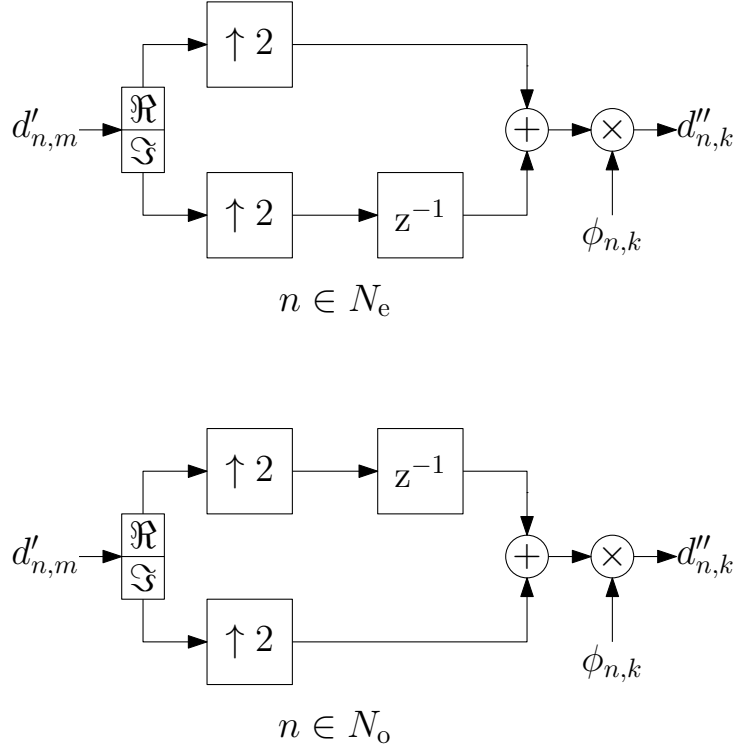
Figure 2.13: OQAM pre-processing

The orthogonality condition which allows the perfect reconstruction of the transmitted symbols in equation (2.17) is reduced to be on the real part only as:

$$\left\langle g_n[i - k\frac{N}{2}], g_{n'}[i - k'\frac{N}{2}] \right\rangle = \Re \left\{ \sum_{i=-\infty}^{\infty} g[i - k\frac{N}{2}] \mathrm{e}^{\frac{\mathrm{j}2\pi n i}{N}} g^*[i - k'\frac{N}{2}] \mathrm{e}^{\frac{-\mathrm{j}2\pi n' i}{N}} \right\} = \delta_{nn'} \delta_{kk'} \,.$$
(2.31)

In this case, the intrinsic interference for $d''_{n,k}$ is given by:

$$\sum_{\substack{i=-\infty \\ n' \neq n \\ k' \neq k}}^{\infty} d''_{n',k'} g[i - k\frac{N}{2}] \mathrm{e}^{\frac{\mathrm{j}2\pi n i}{N}} g^*[i - k'\frac{N}{2}] \mathrm{e}^{\frac{-\mathrm{j}2\pi n' i}{N}} \,.$$
(2.32)

Because only real orthogonality is required, the prototype filter impulse response needs to be a real even symmetric function to achieve the required orthogonality condition. The filter design of the FBMC-OQAM, as done in [94–96], is a critical part of the FBMC-OQAM system since the filter localization in the time-frequency lattice affects its performance in multipath fading channels. Several comparisons [84], [94], and [97] were done between different types of filters for FBMC-OQAM transmission to investigate their capability to operate in radio channels. Different transmission methods such as spreading and MIMO transmission were also investigated. Some of these filters are:
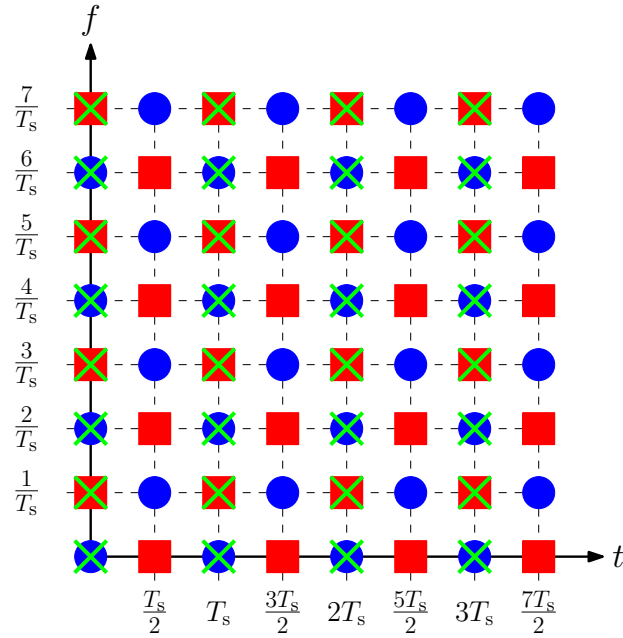
Figure 2.14: Time-frequency lattice of QAM ($\times$), real OQAM($\circ$), and imaginary OQAM ($\square$) symbols, $N = 8$, $M = 4$, $K = 8$

- Extended Gaussian Functions (EGFs) [98–100],

- Hermite filter [88],

- IOTA filter [52],

- Mirabbasi-Martin or PHYsical layer for DYnamic spectrum AcceSs and cognitive radio (PHYDYAS) filter [101–104],

- Optimal Finite Duration Pulses (OFDPs) [105, 106],

- Root Raised Cosine (RRC) filter [107].

The most common implementation for the prototype filters is by the frequency sampling method [108]. In this method, the filter, which is the main part of the FBMC-OQAM modulator shown in Figure 2.15, is assumed to be time-limited with a total length of L_g where the filter impulse response can be represented by a closed-form equation. In this work, it is assumed that $L_\text{g} = NK_\text{g}$ where K_g is the overlapping factor of the filter. For the PHYDYAS filter, the filter impulse response can be written as [109]:

$$g[i] = \grave{g}_0 + 2 \sum_{l=1}^{K_\text{g}-1} (-1)^l \grave{g}_l \cos\left(\frac{2\pi l i}{L_\text{g}}\right), 0 \leq i \leq L_\text{g} - 1, \qquad (2.33)$$

where $\grave{g}_l$ is the magnitude of each frequency sample for $1 \leq l \leq K_\text{g}$. The values of the frequency samples coefficients are obtained from Table 2.1 [109].
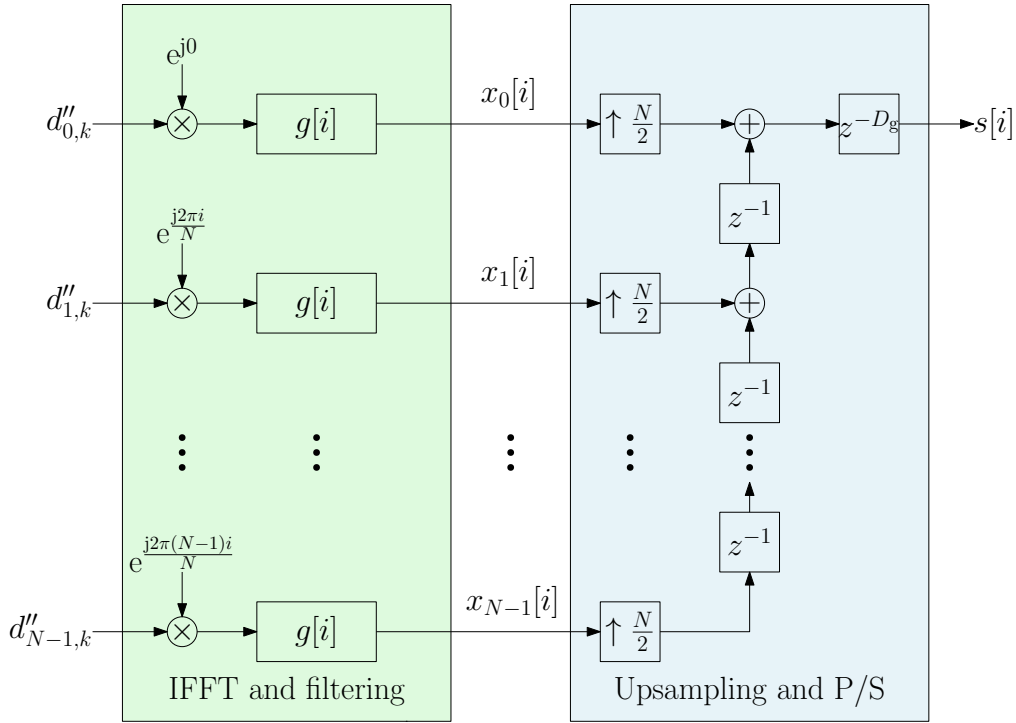
Figure 2.15: FBMC-OQAM modulator

As the overlapping factor increases, the filter length increases as shown in Figure 2.16 for the PHYDYAS filter. The filtering is done in time domain by a linear convolution between the OQAM symbols and the prototype filter. This causes long tails at the start and at the end of the transmission which are not utilized to transmit data. When a short FBMC-OQAM transmission is done, these tails cause significant reduction in the spectral efficiency as discussed in [79]. Moreover, the computational cost also increases significantly as the overlapping factor increases. However, as shown in Figure 2.17, the frequency response of the PHYDYAS filter improves as the overlapping factor increases. It can also be seen that the OOB emissions of PHYDYAS filter are less than those generated by OFDM.

$\grave{g}_l$ \\ K_g	2	3	4
$\grave{g}_0$	1	1	1
$\grave{g}_1$	0.70710678	0.91143783	0.97195983
$\grave{g}_2$		0.41143783	0.70710678
$\grave{g}_3$			0.23514695

Table 2.1: Magnitude coefficients for PHYDYAS filter, $K_g = 2, 3,$ and 4
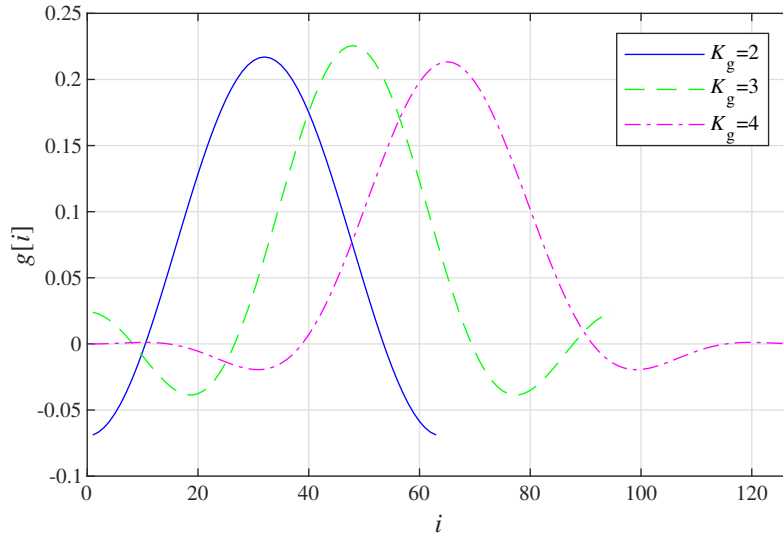
Figure 2.16: Impulse response of the PHYDYAS filter with different K_g values, N=32

To overcome the problems caused by long transmission tails, some solutions were suggested such as hard truncation using a rectangular window in [110]. However, this solution increases the OOB emissions as existing in conventional OFDM. In [111], high OOB emissions were also detected when the circular convolution was applied instead of the linear convolution. Also in [111], windowing was used to reduce the OOB emissions but at the cost of generating new tails.

After the IFFT and filtering stages, upsampling is performed on the filtered signal. The delay D_g caused by the filter needs to be compensated after the P/S conversion at the end of the FBMC-OQAM modulator as done in [94]. Alternatively, the delay can be added at the start of the receiver where:

$$D_\mathrm{g} = L_\mathrm{g} - NK_\mathrm{g} + 1 \,. \tag{2.34}$$

The resultant signal is then converted to an analog signal by the DAC. Afterwards, in the Radio Frequency (RF) section, the signal is upconverted and amplified by the PA. The amplified signal is then sent through the system channel.

At the receiver shown in Figure 2.18, the received signal is regulated by the AGC, downconverted, and filtered in the RF section. The resultant signal is converted to a digital serial signal by the ADC. The serial signal is converted to parallel by the S/P converter which includes an additional stage. In this stage, downsampling by the same factor used in the transmitter ($N/2$) is performed as shown in Figure 2.19. The downsampled data are then filtered by the filterbank. Later on, FFT is performed on the filtered data.
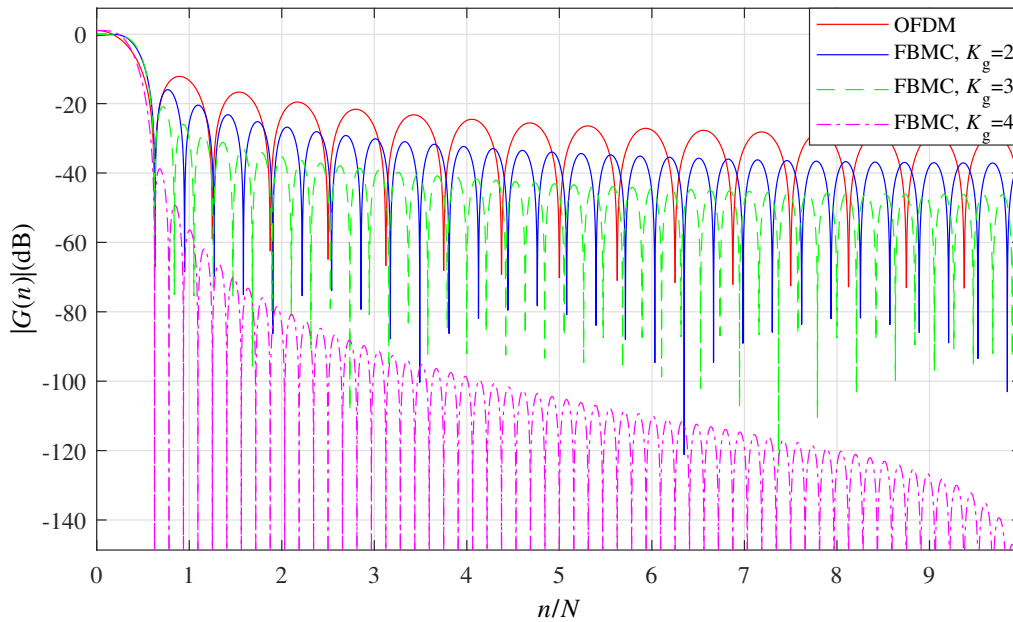
Figure 2.17: Frequency response of the PHYDYAS filter with different K_g values compared to the frequency response of the rectangular window in OFDM, $N{=}32$

After the FFT stage, the parallel data are equalized to compensate the channel effect. For a single tap ZF equalizer, the equalized OQAM data are given by [67]:

$$\hat{y}'_{n,k} = \frac{y'_{n,k}}{H_{\mathrm{s},n,k}} \, . \tag{2.35}$$

To have a better equalization, an automatic equalizer was introduced to eliminate ICI and ISI under certain propagation scenarios in [112]. The Minimum Mean Squared Error (MMSE) Equalizer can also be applied where the channel noise effect is also considered in the cost function that minimizes the mean squared error. The work done in [113] using FBMC-OQAM, for a time-invariant channel, shows that the MMSE can be expressed as a function of the number of subcarriers and the noise power level.
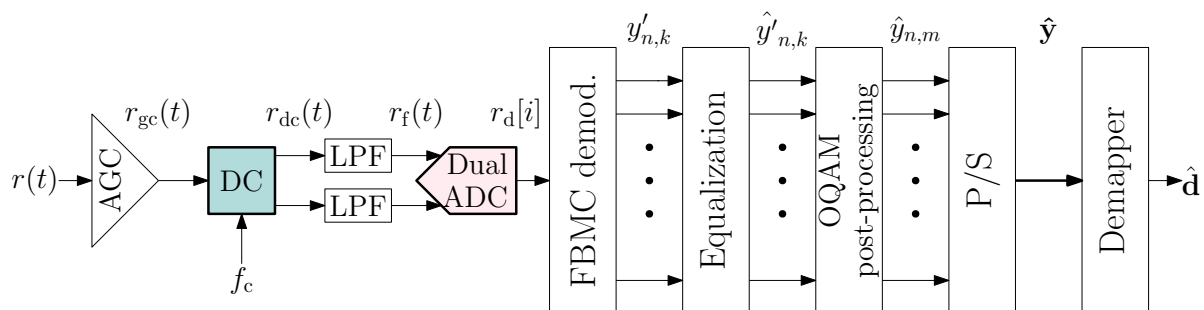
Figure 2.18: FBMC-OQAM receiver
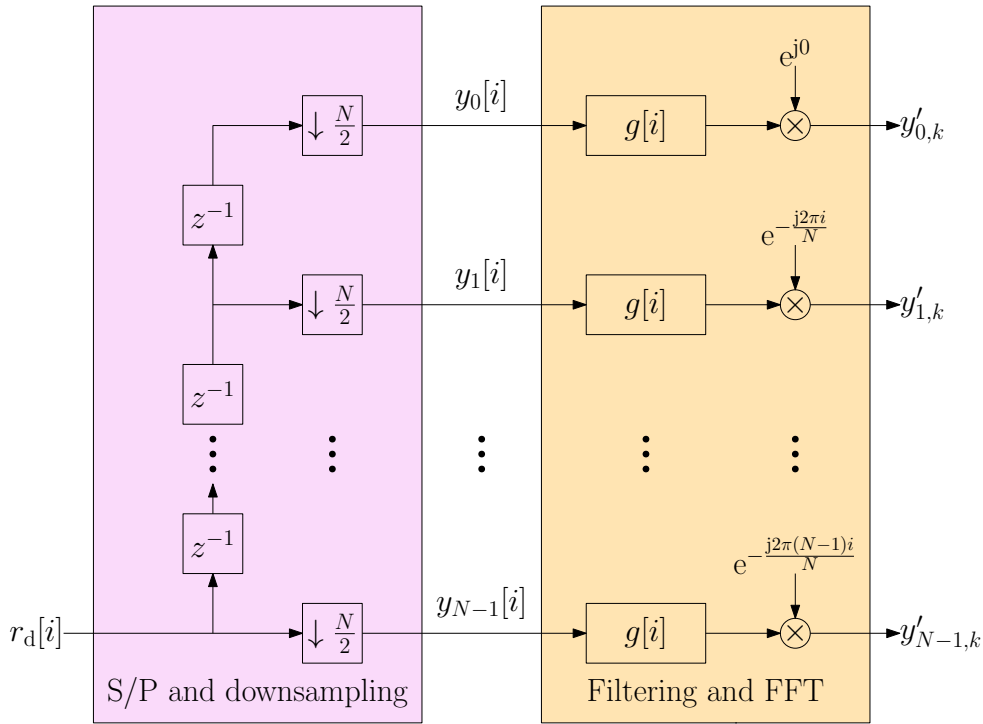
Figure 2.19: FBMC-OQAM demodulator

Practically, it was proven in [40] and [114], that a single-tap equalizer is usually sufficient in doubly dispersive channels when a suitable Δf is applied to maximize the Signal-to-Interference power Ratio (SIR). Moreover, a suitable filter bank selection is useful to overcome the channel selectivity in time and frequency. In this case, the time and frequency localization of the prototype filter need to be related to the channel parameters as [80]:

$$\frac{\sigma_{\mathrm{i}}}{\sigma_{\mathrm{n}}} \approx \frac{T_{\mathrm{rms}}}{f_{\mathrm{rms}}}, \qquad (2.36)$$

where T_{rms} is the Root Mean Square (RMS) delay spread and f_{rms} is the RMS Doppler shift which is, for a Jakes Doppler spectrum, given by [40]:

$$f_{\mathrm{rms}} = \frac{f_{\mathrm{max}}}{\sqrt{2}} = \frac{v f_{\mathrm{c}}}{\sqrt{2} v_{\mathrm{c}}}, \qquad (2.37)$$

where f_{max} is the maximum Doppler shift, v is the velocity and v_{c} is the speed of light. Multitap equalizers for FBMC-OQAM were implemented to improve the single tap equalization as done in [115–118]. However, these equalizers consider the neighboring symbols in time only. This can limit their operation in channels with high Doppler spreads. This was the reason to introduce a 2-dimensional equalizer for FBMC-OQAM in [119] which combines the information from the neighboring resource blocks in time and frequency domains.

However, as discussed in [40] and [80], it is also reasonable to shift from FBMC-OQAM to FBMC-QAM to reduce the symbol density in time. Some equalizers use an interference cancellation matrix which can be obtained for each prototype filter as done in [120]. Another solution is to modify the equalizer coefficients to have an optimal operation for each transmission channel as done in [117]. It was concluded in [80], that FBMC variants offer more flexibility than OFDM for the operation in doubly selective channels.

As the core of the equalization process, many efforts were done to investigate the channel estimation in FBMC-OQAM. In [121–123], aided channel estimation methods using pilots and/or preambles were proposed. However, as these methods reduce the spectral efficiency, blind channel estimation was discussed in [91], [124], and [125]. Although, it may reduce the probability of the accurate channel estimation in time-invariant channels. At the end stage of the receiver, the equalization is followed by the OQAM post-processing as shown in Figure 2.20 and described in [93]. At the OQAM post-processor, the OQAM equalized symbols are shifted by the complex conjugate of $\phi_{n,k}$ which was implemented at the transmitter. Then, the destaggering is done to convert the OQAM symbols into QAM symbols and the sampling time is doubled as:

$$
\hat{y}_{n,m} = \begin{cases} \Re\left\{\hat{y}'_{n,k}\phi^*_{n,k}\right\} + \mathrm{j}\Re\left\{\hat{y}'_{n,k+1}\phi^*_{n,k+1}\right\}, & n \in N_{\mathrm{e}} \\ \Re\left\{\hat{y}'_{n,k+1}\phi^*_{n,k+1}\right\} + \mathrm{j}\Re\left\{\hat{y}'_{n,k}\phi^*_{n,k}\right\}, & n \in N_{\mathrm{o}}. \end{cases} \tag{2.38}
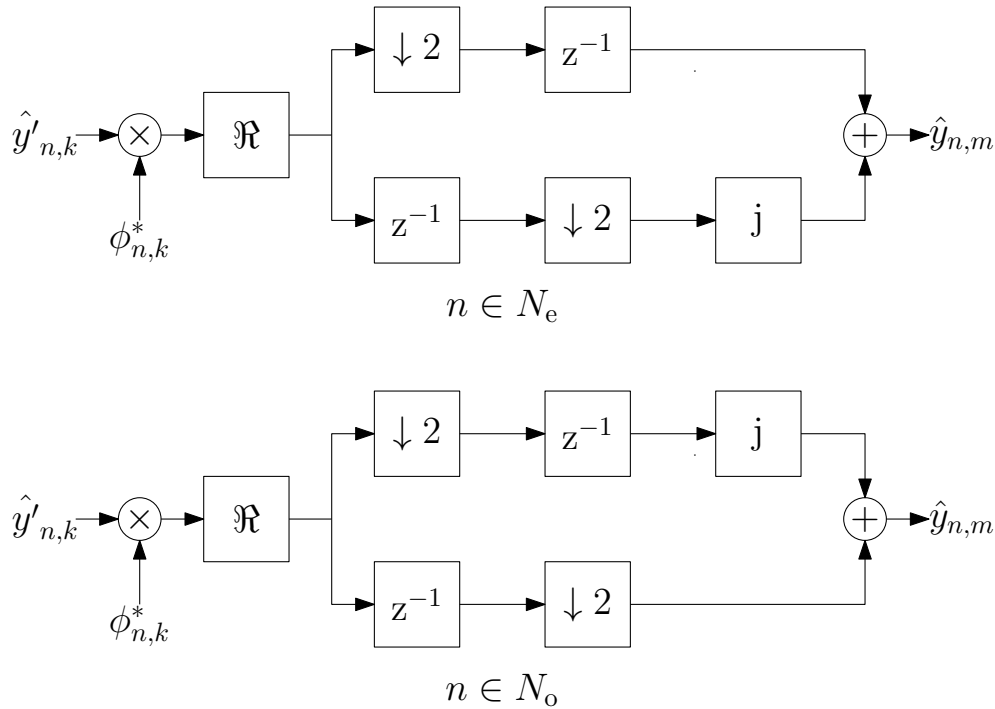$$

Figure 2.20: OQAM post-processing

2.4   Spread FBMC-OQAM

As discussed in the previous chapter, spreading in MC communications was introduced to have a reliable transmission which can operate effectively in selective channels. To improve the performance of MC-CDMA in single and multiuser transmission, the first spread FBMC-OQAM variant was introduced in [4]. This proved that for a full-sized network, an IOTA-based network shows a significant improvement in terms of BER compared to CDMA-OFDM under a multipath fading channel. Spread FBMC-OQAM can be implemented by FS where the transmitted data is spread on subcarriers as done in [4], [5], and [11] or TS where spreading is done on time samples as done in [6], [126], and [127]. Spreading can also be done in both frequency and time dimensions. A good example is the interleaved spreading discussed in [128] where spread data are distributed on different resource blocks. Moreover in FBMC-OQAM, spreading with certain codes can restore the complex orthogonality as done in [5].

2.4.1   Real Spread FBMC-OQAM

In the spread FBMC-OQAM multiuser transmitter which is used in the downlink, the data of U users are transmitted as shown in Figure 2.21. Each user u transmits D_{N} real bits which are PAM modulated to get the mapped data $\mathbf{d}'_{u,k} = [d''_{u,0,k}, d''_{u,1,k}, \cdots, d''_{u,D_{\mathrm{N}}-1,k}]$. The same previously mentioned figure can also describe the uplink transmission if only one user transmits its data. At the OQAM sample index k, the user data are spread on the data subcarriers with a user code $\mathbf{c}_u = [c_{u,0}, c_{u,1}, \cdots, c_{u,L_{\mathrm{c}}-1}]^T$ where L_{c} is the code length and $[]^T$ is the transpose operator. It is also assumed that $N = D_{\mathrm{N}}L_{\mathrm{c}}$ to avoid the overlap between OQAM symbols. If FS is implemented as shown in Figure 2.22(a), the output of the spreader $a_{n,k}$ is given by [4]:

$$a_{n,k} = \sum_{u=0}^{U-1} c_{u,\mathrm{mod}(n,L_{\mathrm{c}})} d''_{u,\lfloor n/L_{\mathrm{c}}\rfloor,k} \phi_{n,k} \,, \tag{2.39}$$

where mod( ) is the modulo operator and $\lfloor\,\rfloor$ is the floor operator. When TS is considered as shown in Figure 2.22(b), D_{K} bits are spread on K OQAM symbols at a single subcarrier as $\mathbf{d}'_{u,n} = [d''_{u,n,0}, d''_{u,n,1}, \cdots, d''_{u,n,D_{\mathrm{K}}-1}]$. Therefore, the overlap in frequency domain is avoided if $K = D_{\mathrm{K}}L_{\mathrm{c}}$. To utilize all subcarriers, the total number of transmitted bits shall be ND_{K}. The output of the spreader in the TS case is [6]:

$$a_{n,k} = \sum_{u=0}^{U-1} c_{u,\mathrm{mod}(k,L_{\mathrm{c}})} d''_{u,n,\lfloor k/L_{\mathrm{c}}\rfloor} \phi_{n,k} \,, \tag{2.40}$$
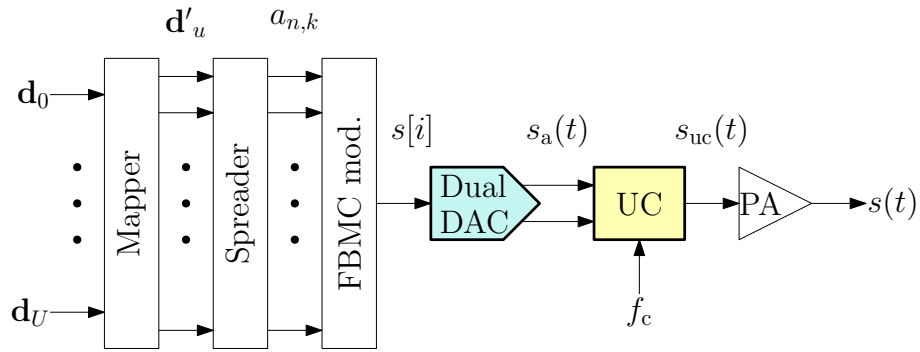
Figure 2.21: Spread FBMC transmitter

As done in CDMA variants, spreading can be done in FBMC-OQAM by several types of codes. The code selection depends on the design requirements such as orthogonality, low cross-correlation, and low PAPR as discussed in [128]. Some of these codes are:

- Gold codes,

- Golay codes,

- Fourier codes,

- low-rate convolutional codes,

- Pseudo-Noise (P-N) codes,

- W-H codes,

- Zadoff-Chu Sequences.
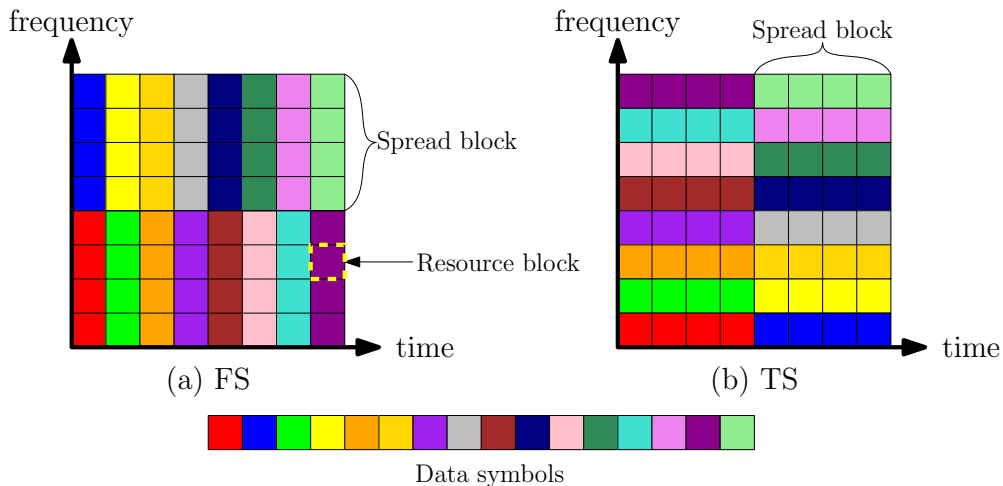
Figure 2.22: Spreading of 16 symbols by FS and TS, $N = 8$, $K = 8$, and $L_{c} = 4$

After spreading, which includes also the phase shift of the OQAM pre-processing, the FBMC-OQAM modulation is done as discussed in the previous section. The signal is then converted to an analog signal and sent by the RF section through the system channel.

At the spread FBMC-OQAM receiver shown in Figure 2.23, the analog signal is amplitude-controlled, down-converted and filtered in the RF section before it is converted to a digital signal by the ADC. The digital serial signal is converted to parallel by the S/P converter and downsampled by $N/2$. Later, filtering and FFT are performed on the downconverted signal. This is followed by the equalization to compensate the channel's effect. Next, despreading is performed according to the selected spreading type and code. When FS is selected, the despread data $\hat{y}_{u,\check{n},k}$ are given by [4]:

$$\hat{y}_{u,\check{n},k} = \sum_{n=0}^{L_c-1} c_{u,n} \hat{y}'_{\check{n}L_c+n,k} \, , \tag{2.41}$$

where $\check{n} \in [0, \cdots, D_N - 1]$. Since the summation in FS is done on resource blocks which are placed on adjacent subcarriers with the same sample index, a weak subcarrier or a high destructive continuous interference tone aimed at a single subcarrier can affect K spread blocks negatively if L_c is not long enough to compensate the error. When TS is applied, a high continuous destructive tone affects D_K TS blocks only. In this case, despreading is done in time domain by [6]:

$$\hat{y}_{u,n,\check{k}} = \sum_{k=0}^{L_c-1} c_{u,k} \hat{y}'_{n,\check{k}L_c+k} \, , \tag{2.42}$$

where $\check{k} \in [0, \cdots, D_K - 1]$. If the transmission is affected by high time selectivity, a destructive interference pulse, or a missed detection at the receiver, N TS spread blocks are affected compared to D_N FS blocks. In both cases, a suitable selection of the code length is required to ensure the robustness of the transmission.
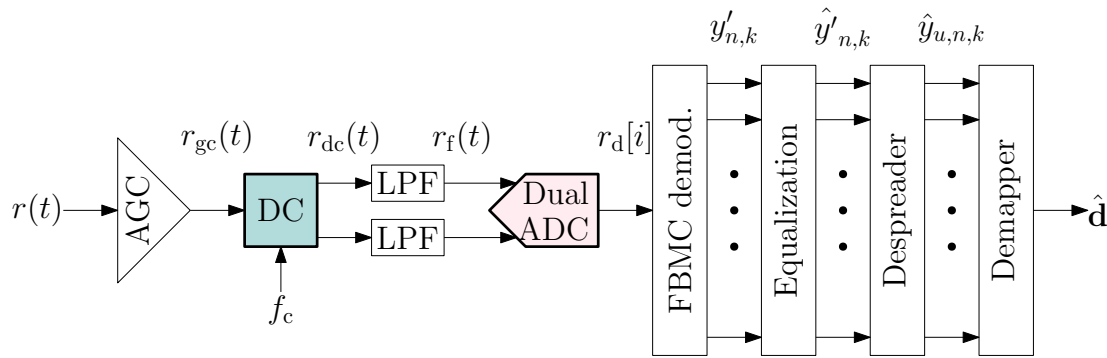

Figure 2.23: Spread FBMC receiver

2.4.2   Complex Spread FBMC-OQAM

Spreading is mainly utilized to enhance the reliability of the MC transmission. However, in the case of FBMC-OQAM, it was proven in [5] and later in [40] that spreading with W-H codes which are optimally chosen can also restore the complex orthogonality. Therefore, a complex symbol can be transmitted in each OQAM resource block.

The optimal code selection is based on a reconstructive rule that splits the W-H matrix in 2 optimal subsets so that the Multiple Access Interference (MAI) is minimized in each subset as done in [5]. Therefore, the maximum number of users in a complex spread FBMC-OQAM network is $L_c/2$ compared to L_c for real spread FBMC-OQAM networks. However, the maximum throughput of both networks is the same due to the fact that in complex spread FBMC-OQAM, a single user transmits a complex symbol every $T_s/2$, while a real spread FBMC-OQAM user transmits a real bit every $T_s/2$. Both full-sized spread FBMC networks are comparable to a full-sized spread OFDM network that uses the same W-H code set without CP. For spread OFDM, the maximum network size is L_c and each user transmits a complex symbol every T_s. This ensures the advantage of the implementation of spread FBMC in multiuser scenarios.

To generate the optimal subsets from the W-H matrix with the minimum order of $L_c = 2$, the row (or column) indeces of the optimal subsets S_1^1 and S_2^1 are [5]:

$$
\begin{aligned}
S_1^1 &= \{1\}\,, \\
S_2^1 &= \{2\}\,.
\end{aligned}
\tag{2.43}
$$

For any order $p = \log_2(L_c)$ of the W-H matrix, the row indeces of the optimal subsets are generated by [5]:

$$
\begin{aligned}
S_1^p &= \left\{\alpha_{1,1}, \alpha_{1,2}, \cdots, \alpha_{1,2^{p-1}}\right\}\,, \\
S_2^p &= \left\{\alpha_{2,1}, \alpha_{2,2}, \cdots, \alpha_{2,2^{p-1}}\right\}\,,
\end{aligned}
\tag{2.44}
$$

where $\alpha_{\psi,\chi}$ is the χ-th row index of the ψ-th optimal subset. The row indeces for the optimal subsets of the next order $p + 1$ are obtained by [5]:

$$
\begin{aligned}
S_1^{p+1} &= S_1^p \cup \overline{S}_1^p\,, \\
S_2^{p+1} &= S_2^p \cup \overline{S}_2^p\,,
\end{aligned}
\tag{2.45}
$$

where $\overline{S}_1^p$ and $\overline{S}_2^p$ are the complements of the optimal subsets with order p. Their row indeces are [5]:

$$
\begin{aligned}
\overline{S}_1^p &= \left\{\alpha_{2,1} + 2^p, \alpha_{2,2} + 2^p, \cdots, \alpha_{2,2^{p-1}} + 2^p\right\}\,, \\
\overline{S}_2^p &= \left\{\alpha_{1,1} + 2^p, \alpha_{1,2} + 2^p, \cdots, \alpha_{1,2^{p-1}} + 2^p\right\}\,.
\end{aligned}
\tag{2.46}
$$

By applying the previously mentioned equations, Table 2.2 summarizes the row indeces for the optimal subsets for W-H matrices of the first four orders. The obtained results for the first three orders are illustrated in Figure 2.24 to show the distribution of the optimal subsets within the W-H matrices.

Subset p	S_1	S_2
1	1	2
2	1,4	2,3
3	1,4,6,7	2,3,5,8
4	1,4,6,7,10,11,13,16	2,3,5,8,9,12,14,15

Table 2.2: Row indeces for the optimal subsets of W-H code matrices

(a) $p{=}1$

(b) $p{=}2$

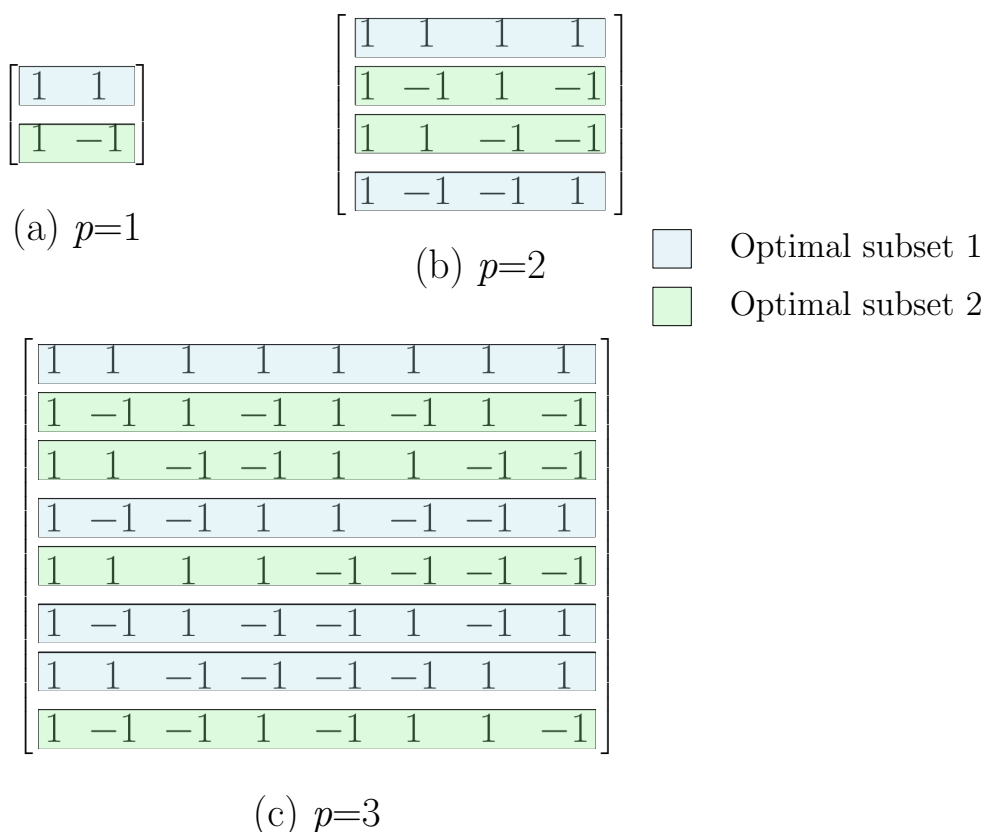Optimal subset 1

Optimal subset 2

(c) $p{=}3$

Figure 2.24: W-H matrices for the first three orders showing the two optimal subsets

2.5   Performance in Industrial Environments

In [129], it was shown that an acceptaple approximation to model wideband indoor prop-
agation can be obtained by the Saleh-Valenzuela (S-V) propagation model introduced
in [130]. The S-V model arranges the received rays, which represent the CIR, into multi-
ple clusters which may have different decays as shown in Figure 2.25. The decay of rays
in a single cluster is defined as the ray decay. The ray decays are taken in consideration
alongside the cluster decay, which represents the decay of the multiple clusters. Modified
S-V channel models were used to model some industrial propagation scenarios as shown
in [131]. For several propagation models, the modifications consist of a closed form for
the cluster decay as obtained in [132]. Moreover, the ray decay is approximated by a
modified power law as done in [133].
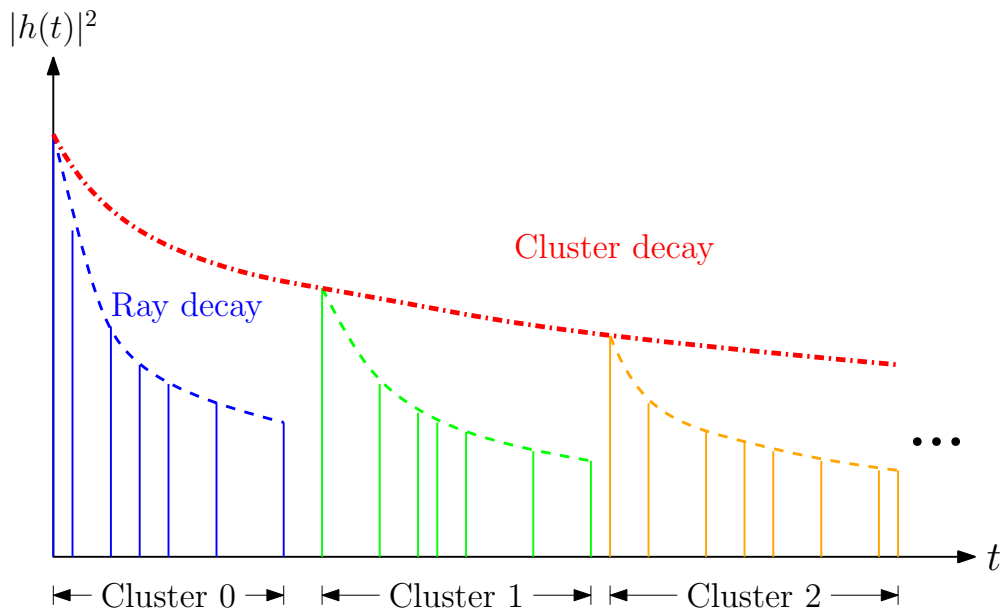
Figure 2.25: S-V channel propagation model

To evaluate the performance of spread FBMC-OQAM using FS and TS, the transmission
chains were simulated and compared with FS and TS schemes based on conventional
CP-OFDM. In the case of CP-OFDM, the application of FS generates an MC-CDMA
scheme while MC-Direct Sequence (DS)-CDMA is obtained by the application of TS. At
the spread OFDM transmitter which is shown in Figure 2.26, the complex QAM data
symbols are spread on the OFDM resource blocks which are separated by T_s in time
domain. In Figure 2.27, the spread OFDM receiver is shown where the equalized symbols
are despread by the user code before the QAM demodulation is performed to estimate
the received data.
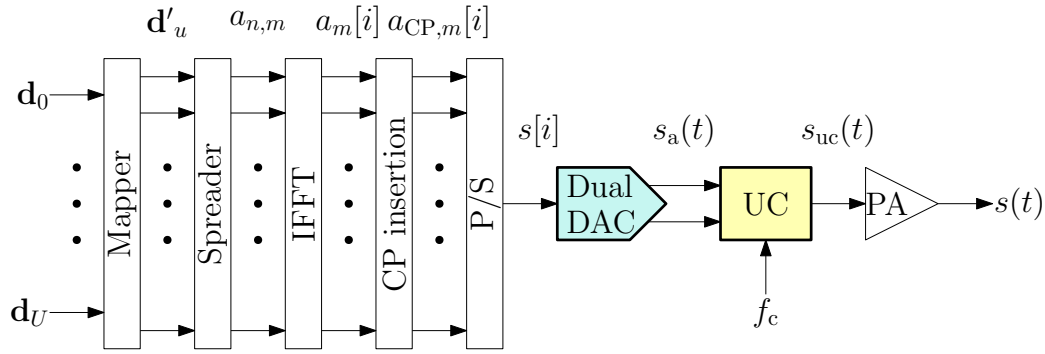
Figure 2.26: Spread OFDM transmitter

Moreover, both real and complex spread FBMC transmission chains were implemented. The simulations were done without channel effects and using both channel models that approximate a Line-Of-Sight (LOS) and a Non Line-Of-Sight (NLOS) propagation scenarios. The implemented channel models are based on measurements taken in an electronics lab [131]. For both channels, T_{max}=200ns and a single-tap ZF equalizer is applied. Several network sizes were tested when the downlink operation is considered. Unless otherwise stated, the simulation parameters are as given in Table 2.3.
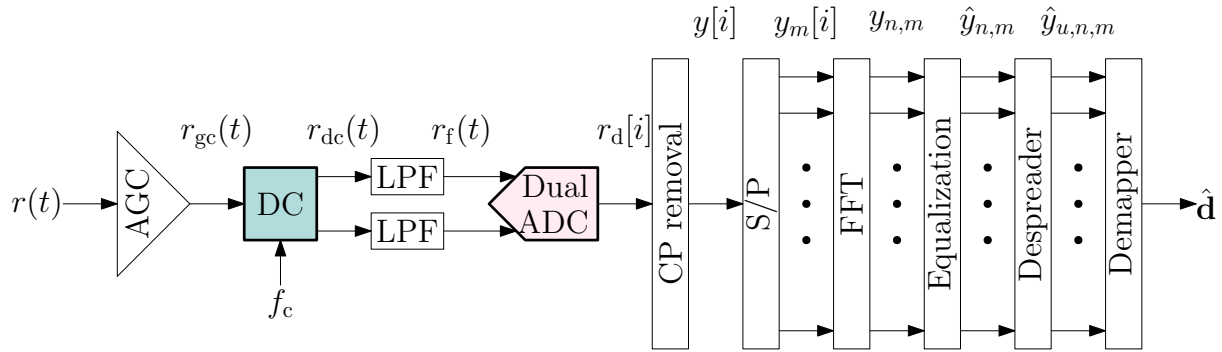
Figure 2.27: Spread OFDM transmitter

Number of subcarriers	32	Number of symbols	32
Modulation type	QPSK	Spreading code	32 bit W-H
FBMC sampling frequency	20 MHz	Filter type	PHYDYAS
OFDM sampling frequency	10 MHz	CP duration	1/16 OFDM symbol
Overlapping factor	4	Number of iterations	10000

Table 2.3: Simulation parameters for spread FBMC

It is proven that the reliability of FBMC is enhanced significantly by the implementation of spreading when a single user transmits its data in the uplink as shown in Figure 2.28. It also indicates that real spread FBMC outperforms all other variants in terms of BER. Complex spread FBMC has the worst performance since the orthogonality is not perfectly restored in the single user scenario. However, a significant spreading gain can be achieved with complex spreading. Moreover, the performance of complex FS-FBMC under the tested industrial propagation channels becomes comparable to MC-CDMA when the SNR is relatively high. When TS is implemented, it can be seen that a more complex equalization is needed to compensate the industrial channels effects. For the downlink scenario with the maximum number of users shown in Figure 2.29, it is shown that the performance of the complex spread FBMC becomes identical to the real spread FBMC as the orthogonality is perfectly restored. Both spread FBMC variants outperform MC-DS-CDMA.

The performance of the spread variants in terms of BER also calls for a discussion of the PAPR performance of spread FBMC using both spreading schemes. The most used measurement of the PAPR performance is the Complementary Cumulative Distribution Function (CCDF). The CCDF of the PAPR is determined by:

$$\Pr\left\{\eta > \eta_0\right\},\qquad\qquad (2.47)$$

where $\Pr\{\ \}$ is the probability operator and η_0 is a given PAPR threshold.

For unspread FBMC, as discussed in [93], the PAPR characteristics are similar to OFDM and filtering has a minor effect. However, the PAPR of the FS variants improves as more users transmit their data in the downlink as shown in Figure 2.30(a). It can also be seen that the single user FS case, which equally represent the uplink scenario, has the worst PAPR. The PAPR of the MC-CDMA remains better than FS-FBMC when the network size is the same. When TS is applied in the downlink transmission, the PAPR improves as the number of users decreases until it reaches the single user case as shown in Figure 2.30(b). Moreover, it is evident that for a certain network size, the PAPR of MC-DS-CDMA is usually lower than the PAPR of TS-FBMC.

In general, it is proven that the PAPR performance of spread FBMC is worse than spread OFDM when the same spreading scheme is implemented. This was also found when DFT spreading was used as discussed in [93] and [134]. However, it was found in [14] that pruned DFT spreading, which is done by clipping at a certain signal power threshold, can lower the PAPR to be comparable to SC-FDMA. When clipping is used, the OOB emissions increase.
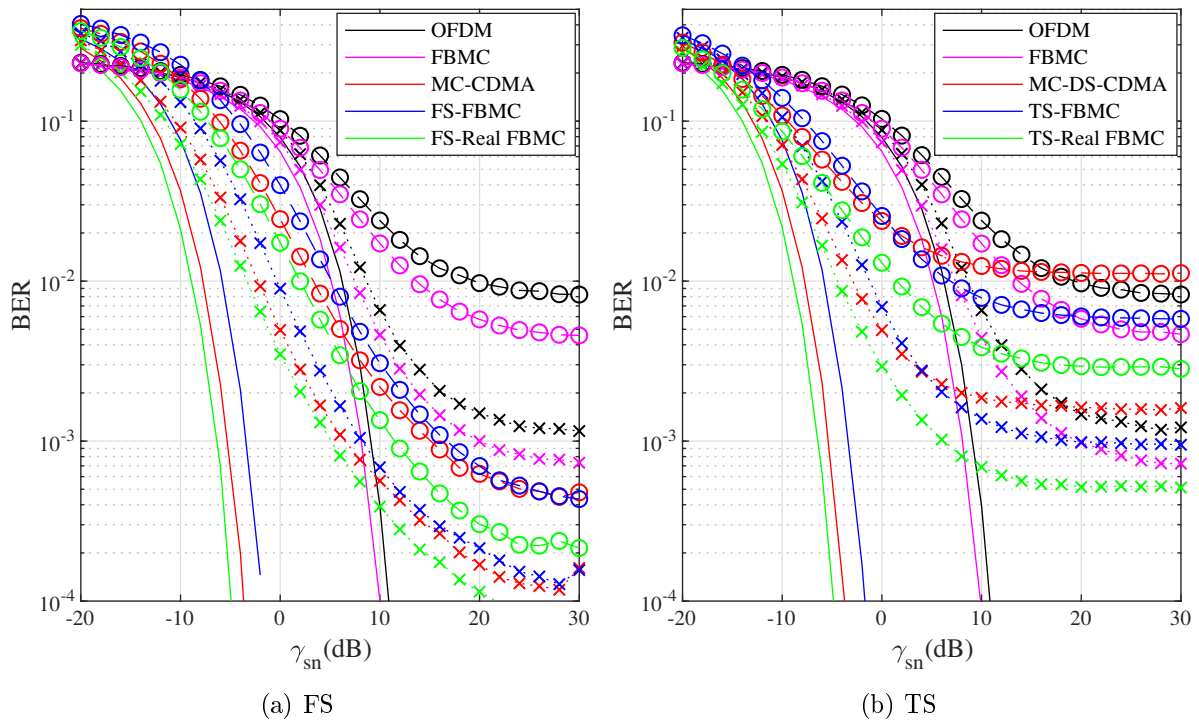
(a) FS

(b) TS

Figure 2.28: Uplink BER without channel effect (no marker), LOS ($\times$), and NLOS ($\circ$) as a function of the signal-to-noise power ratio γ_{sn}

(a) FS

(b) TS
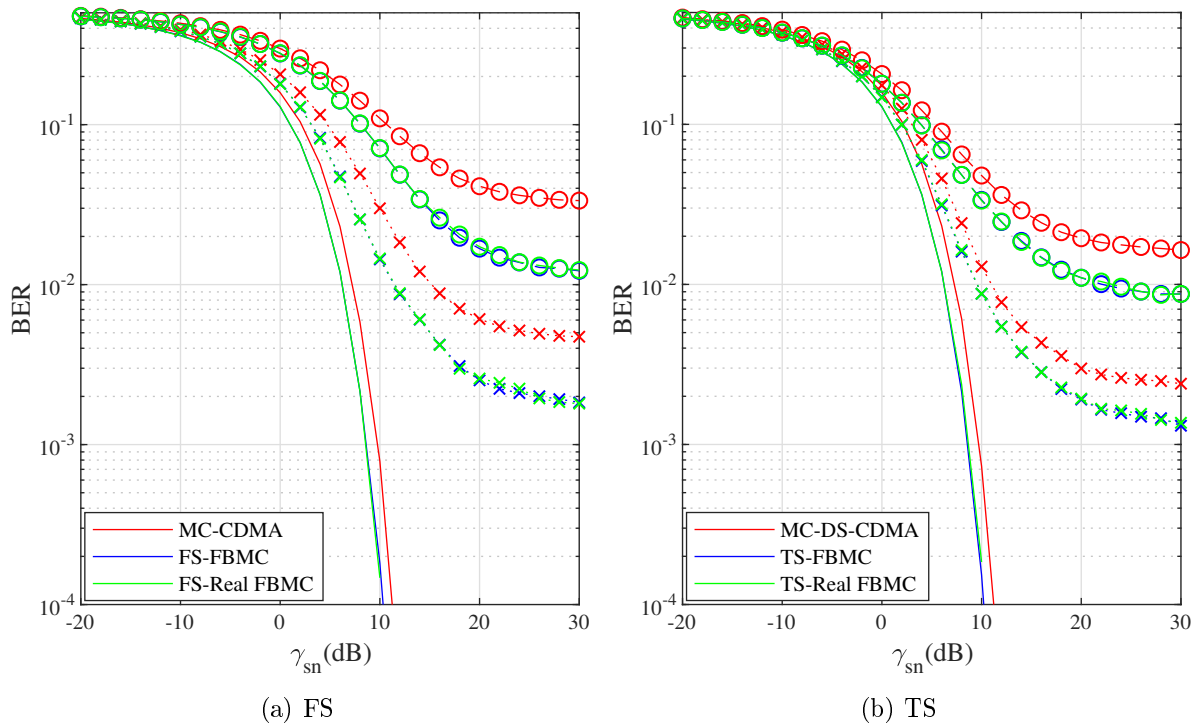
Figure 2.29: Maximum downlink BER without channel effect (no marker), LOS ($\times$), and NLOS ($\circ$) as a function of the signal-to-noise power ratio γ_{sn}

(a) FS   (b) TS
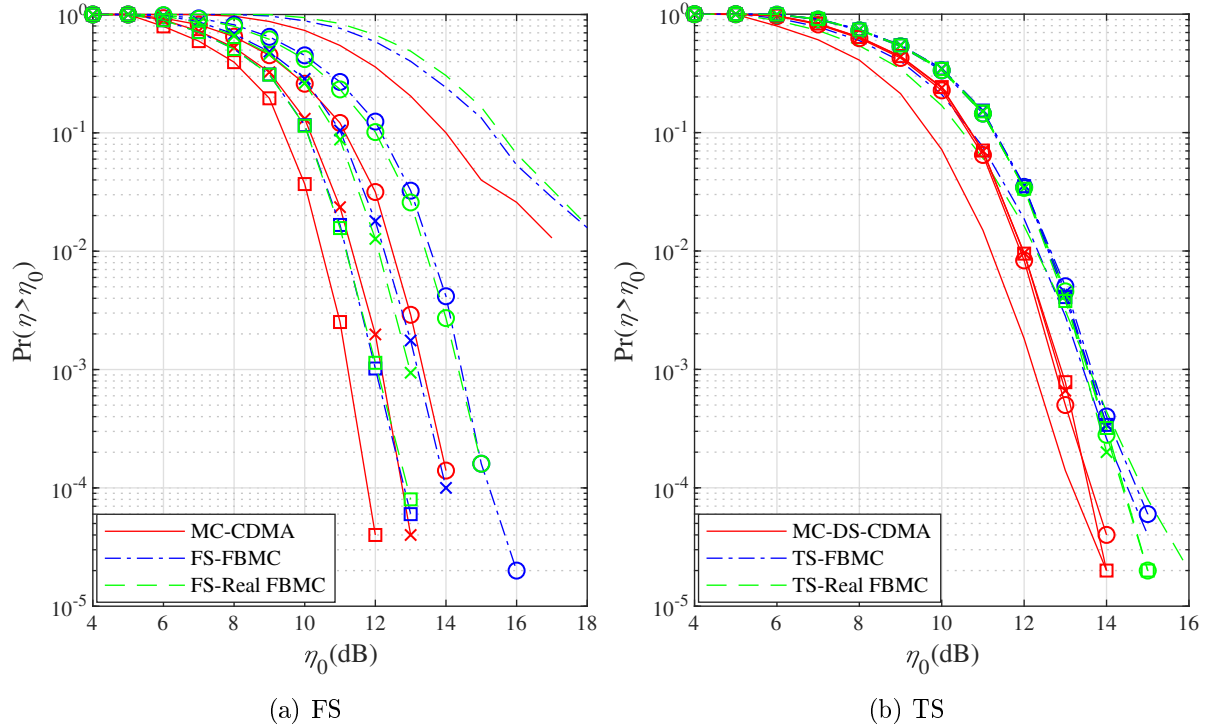
Figure 2.30: CCDF of the PAPR for different network loads using $L_c = 32$, single user (no marker), 25% ($\circ$), 50% ($\times$), and 100% ($\square$)

To validate the industrial channels effects on the spread FBMC transmission, the Probability Density Functions (PDFs) of the amplitudes of the received signals are shown in Figure 2.31 for a single user that uses complex FBMC transmssion. For a large number of samples, both real and imaginary parts of the FBMC transmission have a normal distribution. This results in a Rayleigh distribution for the PDF of the transmitted amplitude as shown in Figure 2.31. It is also shown that when FS is applied in the uplink without considering the channel effect, a higher standard deviation is obtained. However, when the industrial channels are applied, more Gaussian noise is affecting the uplink FS transmission as shown in Figure 2.31(a). The industrial channel effects are less decisive on the uplink transmission when TS is applied in the uplink as shown in Figure 2.31(b). As mentioned in [131], Weibull distribution fits the amplitude PDF of the LOS and the NLOS channels more than other tested statistical distributions.

In Figure 2.32, the received amplitude PDFs of the full-sized complex FBMC transmission are shown. For both spreading types, the received amplitude PDFs are slightly affected by the industrial channels when they are compared to the no-channel scenarios. For the channel effects simulations, the number of samples is increased to 1024 to minimize the effect of the transmission tails and the SNR is fixed at 10dB.

(a) FS

(b) TS

Figure 2.31: Received amplitude PDFs for a single user (uplink) complex spread FBMC transmission using different channels,$\gamma_{\mathrm{sn}} = 10\mathrm{dB}$

(a) FS

(b) TS
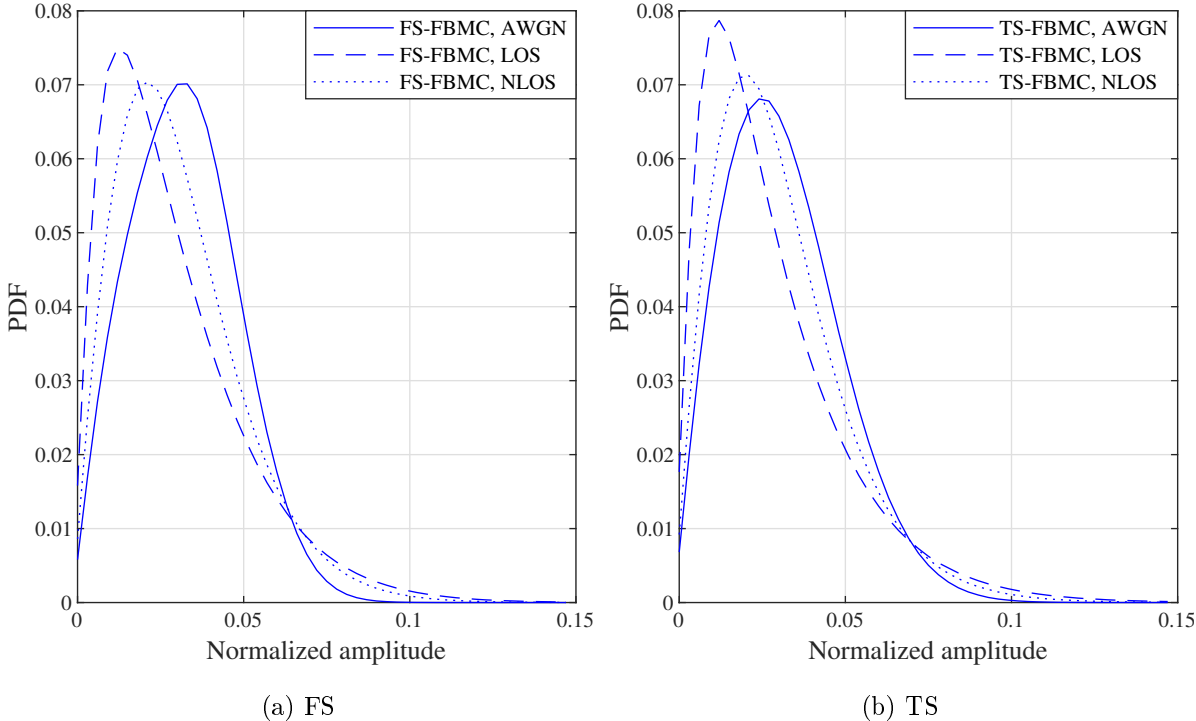
Figure 2.32: Received amplitude PDFs for a full-sized downlink complex spread FBMC transmission using different channels,$\gamma_{\mathrm{sn}} = 10\mathrm{dB}$

2.6   Summary

In this chapter, the MC modulation was discussed as a solution to increase the reliability of wireless communications in frequency selective ch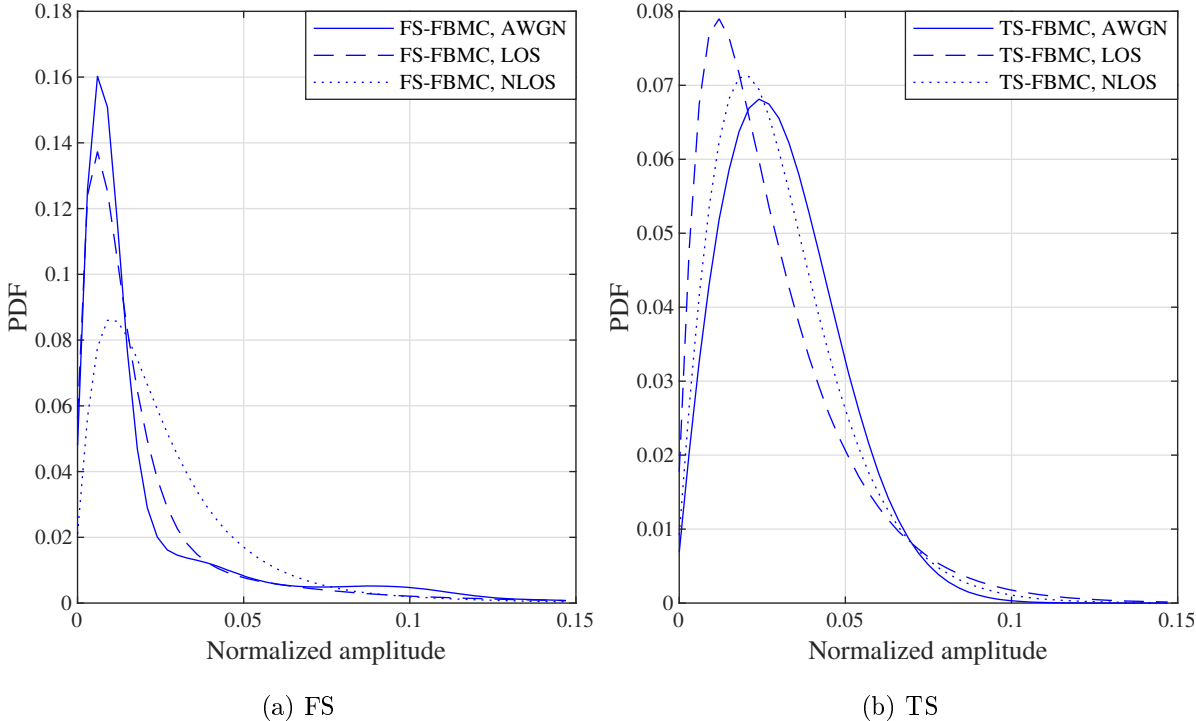annels. OFDM was explained as one of the most applied variants of MC transmission. It also examined the use of orthogonal subcarriers in OFDM through the application of FFT/IFFT resulting in reduced hardware complexity of the MC transmission and increased the spectral efficiency.

However, OFDM has many shortcomings such as the need of a CP when a multipath channel is present, the high OOB emissions which require the use of guard subcarriers or filters to avoid interfering neighboring channels. These disadvantages lead to the degradation of the spectral efficiency of OFDM transmission.

To overcome the previously mentioned problems, FBMC is implemented using prototype filters that have better frequency responses than the rectangular pulse of the conventional OFDM. This reduces the OOB emissions significantly compared to OFDM. By applying OQAM to the FBMC transmission, which needs a doubled sampling frequency, the FBMC transmission is more efficient than conventional OFDM under channels with low delay spread. Moreover, FBMC does not need a CP to avoid ISI created by the multipath channel. Therefore, a higher spectral efficiency can be achieved by the implementation of FBMC.

Later, spread FBMC variants were discussed as candidates for a reliable transmission that merges the advantages of the high throughput FBMC-OQAM and the reliability of CDMA. Under the tested industrial propagation channels, both real and complex spread FBMC networks with full capacity were able to ensure more reliability than MC-CDMA and MC-DS-CDMA in the downlink operation. When the performance of the uplink transmission was investigated, real spread FBMC was more reliable than CP-OFDM variants.

Chapter 3

ADC Effects on Spread FBMC

The joint effect of quantization and clipping created by the ADC at the spread FBMC receiver is discussed in this chapter. It begins with a discussion of the data conversion in the spread FBMC transmission chain, with a focus on the operation characteristics of the ADC to define the quantization and clipping. Next, the performance of spread FBMC in frequency and time domains under several industrial propagation channels is investigated. Using a wide range of ADC resolutions, the simulation results show how the reliability is affected by the clipping level of the ADC. For each channel scenario, the optimal clipping level and the maximum SQNR are obtained for the uplink and the maximum-sized downlink of the spread FBMC network.

3.1   Data Conversion in Spread FBMC

As discussed in the previous chapter, the spread FBMC baseband digital signal need to be converted to an analog signal before the transmission is done by the transmitter RF section. At the receiver, the received analog signal, which is affected by noise, is processed through the receiver's RF section before it is converted to the digital baseband signal by the ADC. Both data conversions as well as the RF sections in the transmitter and the receiver are shown in Figure 3.1.
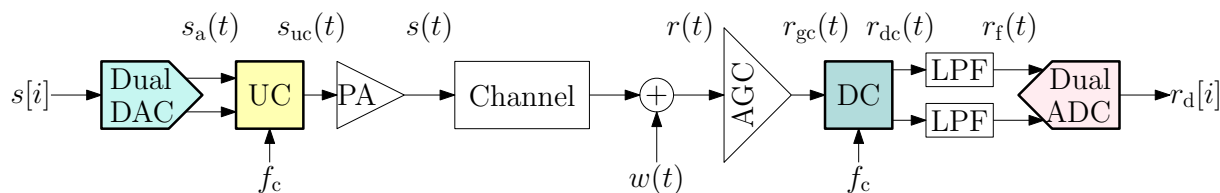
Figure 3.1: Spread FBMC transmission chain section with data conversion

3.1.1   Digital-to-Analog Conversion

In the DAC, the codewords generated by the baseband transmitted signal are converted to their corresponding voltage levels. The voltage levels need to be unique for each codeword to ensure a normal DAC operation. For a uniform DAC, the output voltage levels increase by a fixed level of Δv_a which is defined as the DAC quantization step size [46]. The DAC characteristic, as shown in Figure 3.2 for a 3-bit uniform DAC, consists of a number of $2^{b_\mathrm{dac}} = 8$ discrete points, where b_dac is the DAC resolution.

The input codewords can be coded by a binary representation or other coding types (e.g. Gray coding) as shown in [135]. It is important to note, as discussed in the previous chapter, that $s[i]$ is an upsampled serial signal generated by the IFFT digital parallel output. As discussed in [34] and [136], the digital output of the IFFT has a certain resolution which affects the performance of the transmission. The DAC conversion can be done as unipolar conversion where $0 \leq s_\mathrm{a}(t) \leq A_\mathrm{dac} - \Delta v_\mathrm{a}$, where A_dac is the clipping level of the DAC. For bipolar DAC conversion, it is assumed that $-A_\mathrm{dac} \leq s_\mathrm{a}(t) \leq A_\mathrm{dac} - \Delta v_\mathrm{a}$. The DAC operation can be affected by several types of errors, which are widely discussed in [135], including offset errors where the transfer function is shifted by a constant offset level, gain errors where the slope of the transfer function is different from the ideal one, or non-linearity where a linear approximation is needed by the means of the end points or the best fit of the non-linear curve. These errors are shown in Figure 3.2
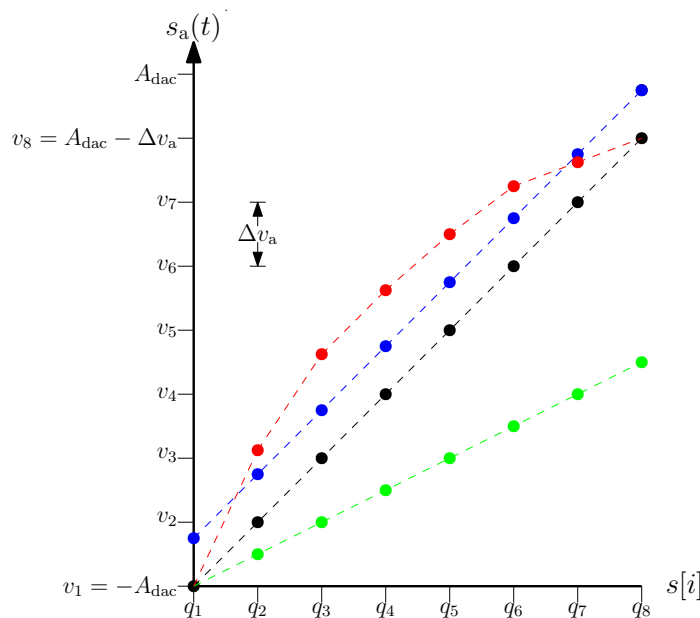
Figure 3.2: 3-Bit bipolar DAC characteristics, ideal (black), offset error (blue), gain error (green), and non-linear operation (red)

3.1.2   Power Amplification

After the DAC conversion, the resultant analog signal is upconverted by a certain carrier frequency. Afterwards, the upconverted signal is amplified by the PA. The operational characteristics of the PA, as illustrated in Figure 3.3, show the presence of non-linear distortion as the input level exceeds the maximum allowed input power for linear operation $P_{\mathrm{uc,lin}}$. The non-linear region can be represented by the Input Back-Off power ratio (IBO) γ_{i} as:

$$\gamma_{\mathrm{i}} = \frac{P_{\mathrm{uc,max}}}{P_{\mathrm{uc,lin}}}\,, \tag{3.1}$$

where $P_{\mathrm{uc,max}}$ is the PA maximum input power. Similarly, the non-linearity of the PA output can be described by the Output Back-Off power ratio (OBO) γ_{o} as:

$$\gamma_{\mathrm{o}} = \frac{P_{\mathrm{pa,max}}}{P_{\mathrm{pa,lin}}}\,, \tag{3.2}$$

where $P_{\mathrm{pa,max}}$ and $P_{\mathrm{pa,lin}}$ are the maximum output power of the PA and the maximum output power of the linear region, respectively. Both IBO and OBO need to be as low as possible to ensure a good PA operation. However, as a perfect linear operation is not possible in practical applications, the PAPR of the transmitted signal need to be reduced to avoid the non-linear PA operation as done in [137–140]. Moreover, as mentioned in the previous chapter, the high PAPR requires a high DAC resolution that minimizes the DAC quantization error to allow an acceptable analog representation of the baseband digital signal. However, a higher resolution DAC increases the power consumption.
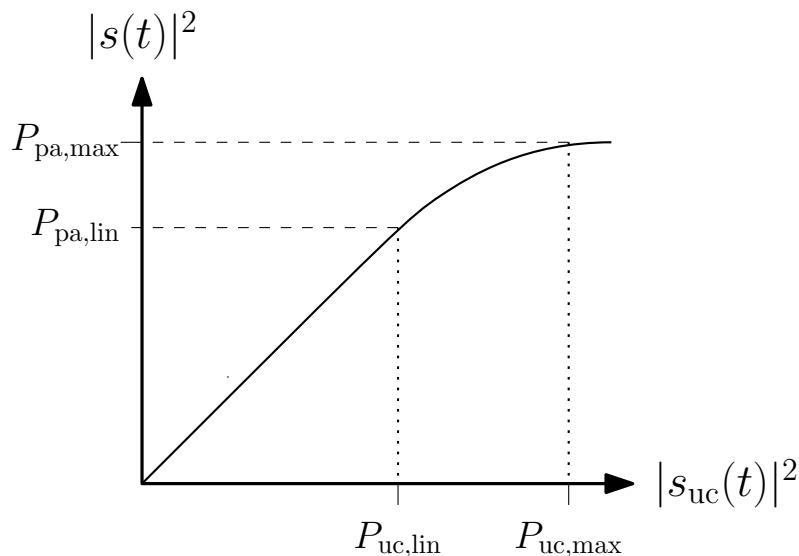
Figure 3.3: PA operational characteristics

3.1.3   Analog-to-Digital Conversion

At the spread FBMC receiver shown in Figure 3.4, the input of the ADC which is the output of the RF section is separated into real and imaginary parts and sampled at the sampling rate of the baseband spread FBMC system $NT_{\mathrm{s}}/2$ as:

$$r_{\mathrm{f}}(iNT_{\mathrm{s}}/2) = \Re\{r_{\mathrm{f}}(iNT_{\mathrm{s}}/2)\} + \mathrm{j}\Im\{r_{\mathrm{f}}(iNT_{\mathrm{s}}/2)\}\,. \tag{3.3}$$

The digital signal is then generated by the quantization function Q_{ad} on each branch as:

$$r_{\mathrm{d}}[i] = Q_{\mathrm{ad}}(\Re\{r_{\mathrm{f}}(iNT_{\mathrm{s}}/2)\}) + \mathrm{j}Q_{\mathrm{ad}}(\Im\{r_{\mathrm{f}}(iNT_{\mathrm{s}}/2)\})\,. \tag{3.4}$$

If perfect sampling is assumed, the quantization error $e_{\mathrm{q}}[i]$ is defined as the difference between the ADC output and its sampled input as:

$$e_{\mathrm{q}}[i] = r_{\mathrm{f}}(iNT_{\mathrm{s}}/2) - r_{\mathrm{d}}[i]\,. \tag{3.5}$$

The SQNR γ_{sq} is the ratio between the power of the sampled signal and the power of the quantization error:

$$\gamma_{\mathrm{sq}} = \frac{\mathrm{E}\{|r_{\mathrm{f}}(iNT_{\mathrm{s}}/2)|^2\}}{\mathrm{E}\{|e_{\mathrm{q}}[i]|^2\}} = \frac{\sigma_{r_{\mathrm{f}}}^2}{\sigma_{e_{\mathrm{q}}}^2}\,, \tag{3.6}$$
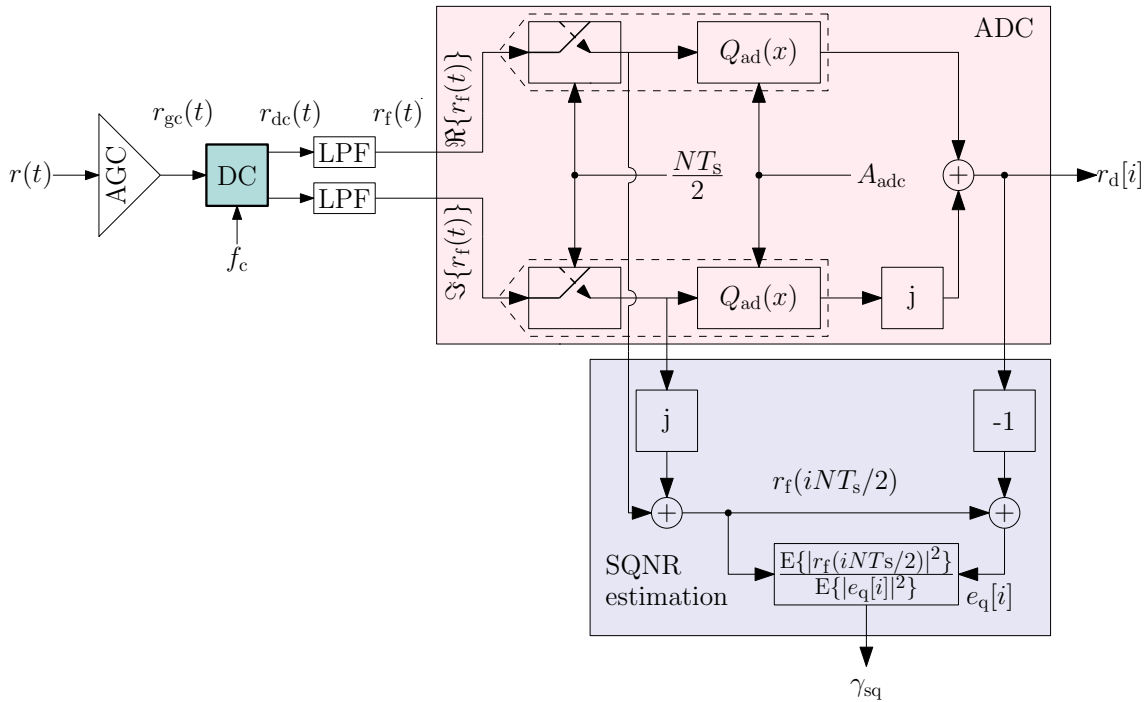
Figure 3.4: Data conversion in a spread FBMC receiver with a detailed ADC block and SQNR estimator

where σ^2 is the signal variance. At the ADC input, the incoming signal is clipped if it exceeds the ADC clipping level A_{adc}. In this case, a perfect AGC operation is assumed which means that the AGC output $A_{\mathrm{agc}} = A_{\mathrm{adc}}$ as shown in Figure 3.5 where some AGC errors are shown as discussed in [141]. If $A_{\mathrm{agc}} < A_{\mathrm{adc}}$, the clipping created by the AGC reduces the number of utilized quantization levels of the ADC. Otherwise, if $A_{\mathrm{agc}} > A_{\mathrm{adc}}$, higher input levels are clipped by the ADC without quantization. The ratio between the standard deviation of the ADC input σ_{r_f} and its clipping level is named the ADC Clipping Factor (CF) μ_{c}, which is given by:

$$\mu_{\mathrm{c}} = \frac{A_{\mathrm{adc}}}{\sigma_{r_f}} . \tag{3.7}$$

Figure 3.6 shows a bipolar ADC with a resolution of b_{adc}-bit so that it has $D = 2^{b_{\mathrm{adc}}}$ quantization levels. The thresholds of the quantizer input v'_ρ are given by [142]:

$$v'_\rho = \begin{cases} -\infty, & \rho = 1 \\ (\rho - \frac{D}{2} - 1)\Delta v', & 2 \leq \rho \leq D \\ \infty, & \rho = D + 1 , \end{cases} \tag{3.8}$$

where $\Delta v' = 2A_{\mathrm{adc}}/(D-1)$ is the quantizer input step size. The quantizer output levels q'_ρ are obtained by:

$$q'_\rho = \left(\rho - \frac{(D+1)}{2}\right)\Delta q', \quad 1 \leq \rho \leq D , \tag{3.9}$$

where $\Delta q'$ is the quantizer output step size. For any input x_{q}, and for $1 \leq \rho \leq D$, the quantization function is given by [142]:

$$Q_{\mathrm{AD}}(x_{\mathrm{q}}) = q'_\rho, \quad v'_\rho \leq x_{\mathrm{q}} < v'_{\rho+1} , \tag{3.10}$$

where $\max(|Q_{\mathrm{ad}}(x_{\mathrm{q}})|) = A_{\mathrm{adc}}$.
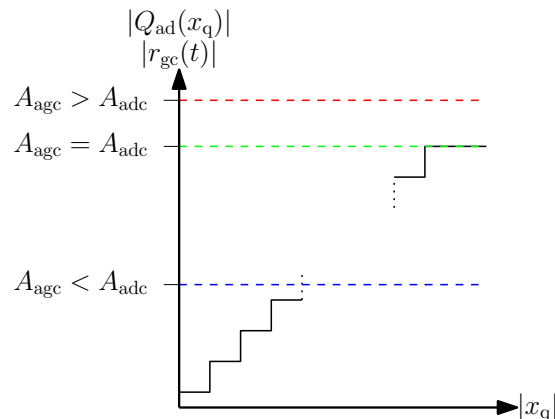
Figure 3.5: AGC operational levels (colored) and the ADC maximum input (black)
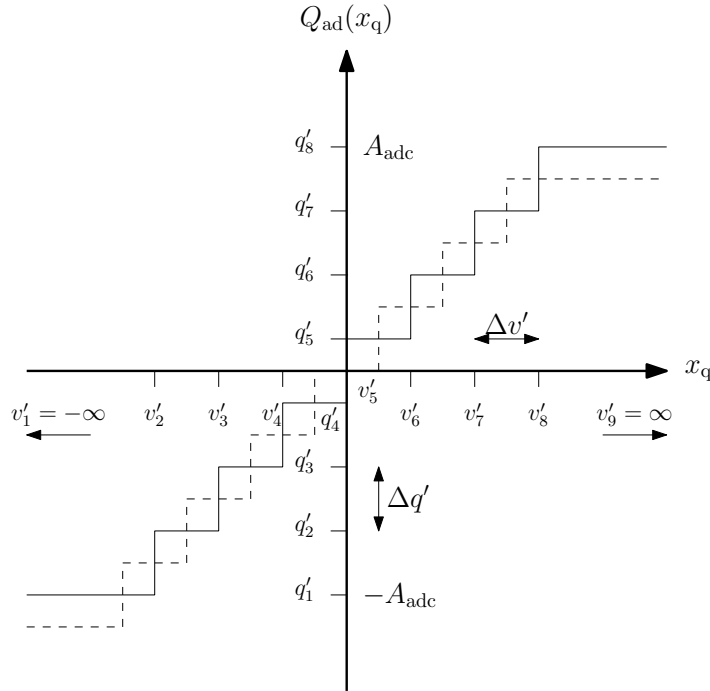
Figure 3.6: 3-Bit midriser (solid) and midtread (dashed) ADC characteristics

Several techniques can be used to restore the clipping done by the ADC as shown in [143]. Although the performance is enhanced, many limitations can affect this enhancement such as fast phase variations or long clipping durations. The ADC is also affected by several operational errors such as discussed for the DAC in section 3.1.

The SQNR and the BER are measured for a wide range of CF using several ADC resolutions. In comparison to the published work in [39] which discussed the FS-FBMC with and without the effect of jamming, the following sections discuss the performance of FS- and TS-FBMC. The effects of the ADC operation under the industrial propagation channels, which were discussed in the previous chapter, are also investigated. It is assumed that the ADC has a mid-riser configuration [144] with a perfect AGC operation in relation to the ADC. A single-tap ZF equalizer is used to compensate the channel effect. The simulation parameters are given in Table 3.1.

Number of subcarriers	32	Number of symbols	32
Modulation type	QPSK	Spreading code	32 bit W-H
FBMC sampling frequency	20 MHz	Filter type	PHYDYAS
OFDM sampling frequency	10 MHz	CP duration	1/16 OFDM symbol
Overlapping factor	4	Number of iterations	10000

Table 3.1: Simulation parameters for the ADC effects on spread FBMC

3.2   Performance for AWGN

The optimal CFs $\mu_{c,opt}$ and their corresponding maximum SQNRs $\gamma_{sq,max}$ for the uplink FS schemes, where a single user transmits its data to the receiver without considering the channel effect, are shown in Figure 3.7. Several iterations are done for μ_c which varies by a step size of $\Delta\mu_c$. The quantization error is minimized as:

$$\mu_{c,opt} = \operatorname*{argmax}_{\mu_c} \left\{ \gamma_{sq}\left(\mu_c\right) \right\} . \tag{3.11}$$

As the SNR increases so that the signal becomes more dominant than noise, the optimal CFs for all schemes increase rapidly until they stabilize as the SNR becomes relatively high (> 10dB). This variation is directly related to the high PAPR for the uplink FS schemes. Since FS-FBMC variants have a larger PAPR, MC-CDMA has a higher SQNR at a lower optimal CF. It is also shown that the optimal CF and the maximum SQNR increase as the ADC resolution increases.

In Figure 3.8, and similar to the results in [39], it is shown that when the CF is extremely low, the signal is affected by high clipping which results in a low SQNR. By comparing the BER, real FS-FBMC outperforms MC-CDMA since the overlapped symbols are more robust to the extremely high clipping than the conventional OFDM symbols. However, as the CF increases, MC-CDMA outperforms real FS-FBMC because of the lower PAPR which leads to a higher maximum SQNR at a lower optimal CF. Moreover, complex FS-FBMC has the worst performance in this case than all other schemes.

As the SQNR approaches its peak value, it is shown that the minimum BER can be obtained by applying a range of CFs. Alongside the transmission type, this range increases as the ADC resolution increases as shown in Figure 3.8. It can be seen that for a moderate or high ADC resolution, a less-strict optimization for the SQNR which reduces the computational complexity can be applied. This is done by determining the CF value which is responsible for the first peak $\mu_{c,fp}$ of the obtained SQNRs as:

$$\gamma_{sq}\left(\mu_{c,fp}\right) > \gamma_{sq}\left(\mu_{c,fp} - \Delta\mu_c\right) , \tag{3.12}$$

and

$$\gamma_{sq}\left(\mu_{c,fp} + \Delta\mu_c\right) \leq \gamma_{sq}\left(\mu_{c,fp}\right) . \tag{3.13}$$

Subsequently, the SQNR usually starts to decrease in a linear-in-dB manner as the quantization error becomes more effective in the BER. This is caused by the increment of the CF so that the highest quantization levels remain without utilization. Therefore, the Effective Number Of Bits (ENOB) of the ADC decreases. The ENOB b_{eff} is given by:

$$b_{eff} = b_{adc} \log_2 \left[\frac{\max\left(|r_f(t)|\right)}{A_{adc}} \right] . \tag{3.14}$$
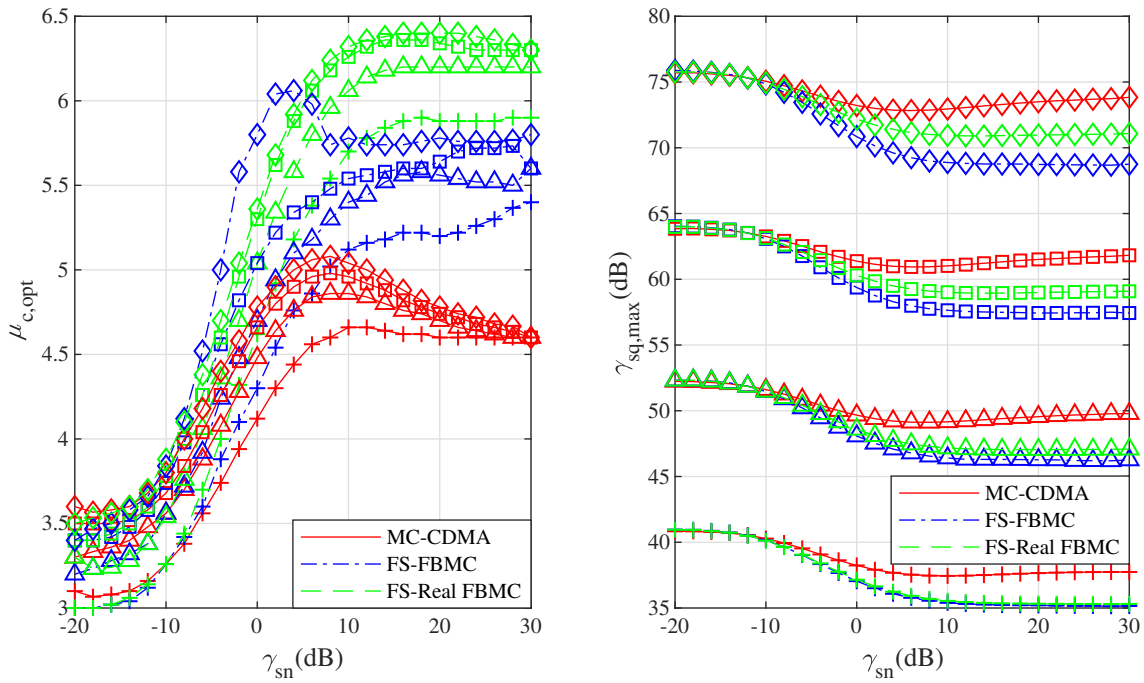
Figure 3.7: Optimal CF and maximum SQNR for FS uplink transmission under AWGN, $b_{\mathrm{adc}} = 8\text{-bit}(+)$, $10\text{-bit}(\triangle)$, $12\text{-bit}(\square)$, and $14\text{-bit}(\diamond)$
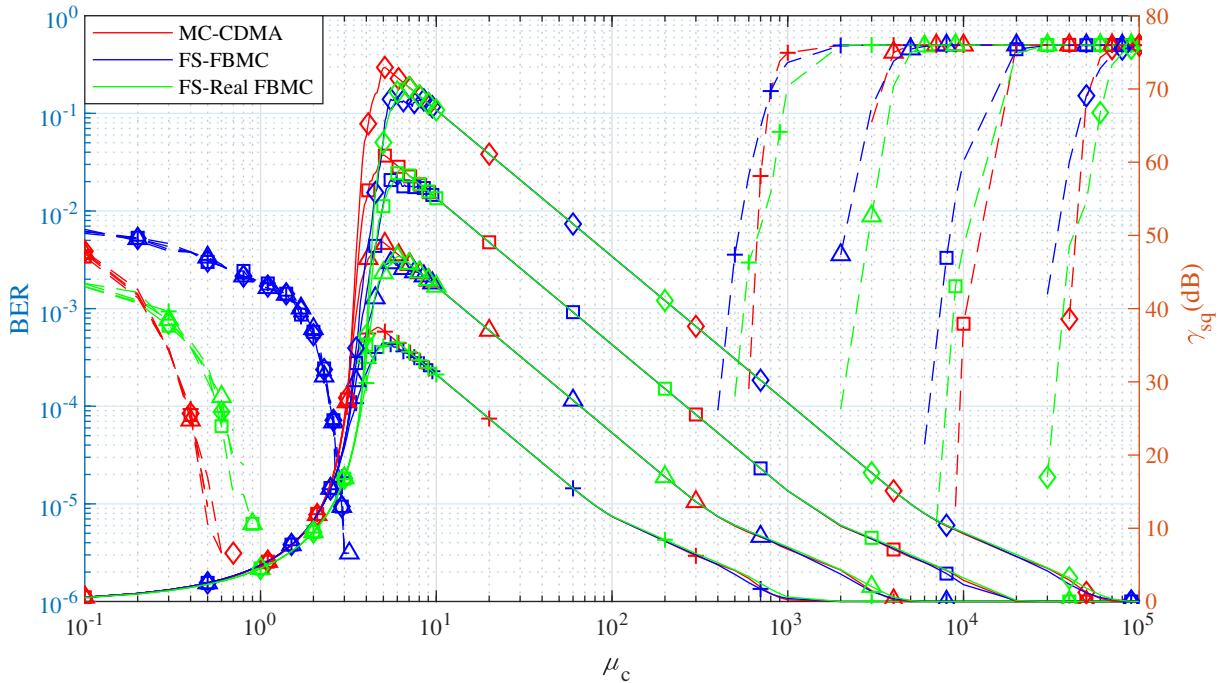
Figure 3.8: BER (dashed) and SQNR (solid) for FS uplink transmission under AWGN, $\gamma_{\mathrm{sn}} = 10\mathrm{dB}$, $b_{\mathrm{adc}} = 8\text{-bit}(+)$, $10\text{-bit}(\triangle)$, $12\text{-bit}(\square)$, and $14\text{-bit}(\diamond)$

As shown in Figure 3.9, when TS is applied in the uplink, the optimal CF for the TS-FBMC variants remains relatively constant as the SNR increases due to the moderate PAPR of the uplink TS-FBMC schemes in comparison to FS-FBMC schemes. This causes less variation in the maximum SQNR. However, as discussed in chapter 2, the relatively low PAPR of MC-DS-CDMA causes a rapid decay in the optimal CF as the signal becomes more dominant at the receiver which reflects in the increase of the maximum SQNR. At SNR= 10dB, Figure 3.10 shows that the performances of TS-FBMC and MC-DS-CDMA are almost equal for low CF levels when the clipping error is dominant. For high CF levels where the error is caused by the large quantization levels, TS-FBMC outperforms MC-DS-CDMA.

In the downlink transmission, where the maximum number of users is implemented, and the PAPR decreases for FS-FBMC when the number of users increases, it is shown in Figure 3.11 that the optimal CF usually decreases when SNR levels increase. This results in a slight increment of the maximum SQNR as the SNR increases. However, since the MC-CDMA downlink has a lower PAPR than FS-FBMC, a higher maximum SQNR can be obtained with a lower optimal CF. When the full capacity downlink is tested with an SNR= 10dB as shown in Figure 3.12, and similar to the results in [39], FS-FBMC variants outperforms MC-CDMA as the SQNR decreases due to the high CF values. The restoration of the orthogonality for the complex FS-FBMC, alongside the PAPR reduction, improve its performance to be similar to real FS-FBMC.

In Figure 3.13, the optimal CFs of the full capacity downlink TS-FBMC variants increase as the SNR increases which cause a slight decay in the corresponding SQNR. For the MC-DS-CDMA downlink, the optimal CF remains approximately constant for each ADC resolution. This results in higher SQNR levels for the MC-DS-CDMA downlink in comparison to the TS-FBMC downlink schemes. As it was proven for the FS full capacity downlink in terms of BER, TS-FBMC variants outperform MC-DS-CDMA, as shown in Figure 3.14, when the CF becomes relatively high for each ADC resolution. Moreover, the performance of the complex TS-FBMC full capacity downlink is similar to the performance of the real TS-FBMC.

The results of the simulations under AWGN show how the performance of the FBMC variants can be affected with both clipping and quantization errors. The optimal CFs and their resultant maximum SQNR levels can be directly related to the PAPR of the transmission scheme, the spreading type, and the network size in the case of the downlink. Moreover, a higher ADC resolution results in a higher maximum SQNR. However, this usually requires a higher optimal CF.
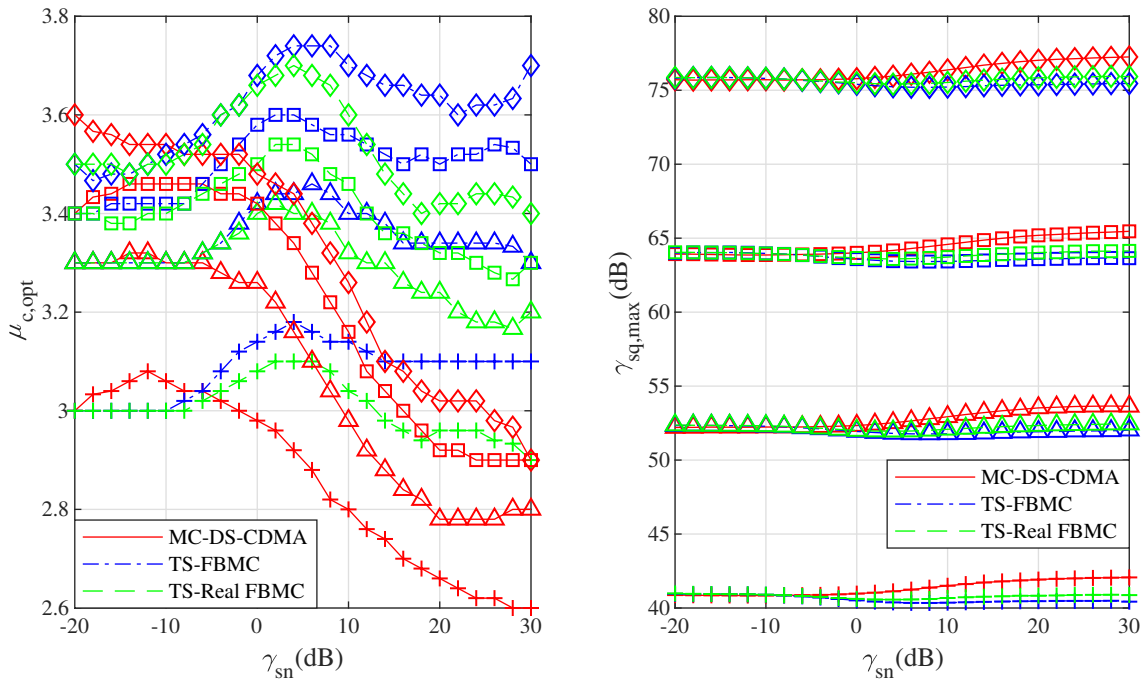
Figure 3.9: Optimal CF and maximum SQNR for TS uplink transmission under AWGN, $b_{\mathrm{adc}} = 8$-bit($+$), 10-bit($\triangle$), 12-bit($\square$), and 14-bit($\diamond$)

Figure 3.10: BER (dashed) and SQNR (solid) for TS uplink transmission under AWGN, $\gamma_{\mathrm{sn}} = 10$dB, $b_{\mathrm{adc}} = 8$-bit($+$), 10-bit($\triangle$), 12-bit($\square$), and 14-bit($\diamond$)

Figure 3.11: Optimal CF and maximum SQNR for FS maximum downlink transmission under AWGN, $b_{adc} = $ 8-bit($+$), 10-bit($\triangle$), 12-bit($\square$), and 14-bit($\diamondsuit$)

Figure 3.12: BER (dashed) and SQNR (solid) for FS maximum downlink transmission under AWGN, $\gamma_{sn} = 10$dB, $b_{adc} = $ 8-bit($+$), 10-bit($\triangle$), 12-bit($\square$), and 14-bit($\diamondsuit$)

Figure 3.13: Optimal CF and maximum SQNR for TS maximum downlink transmission under AWGN, $b_{adc} = 8$-bit($+$), 10-bit($\triangle$), 12-bit($\square$), and 14-bit($\diamondsuit$)
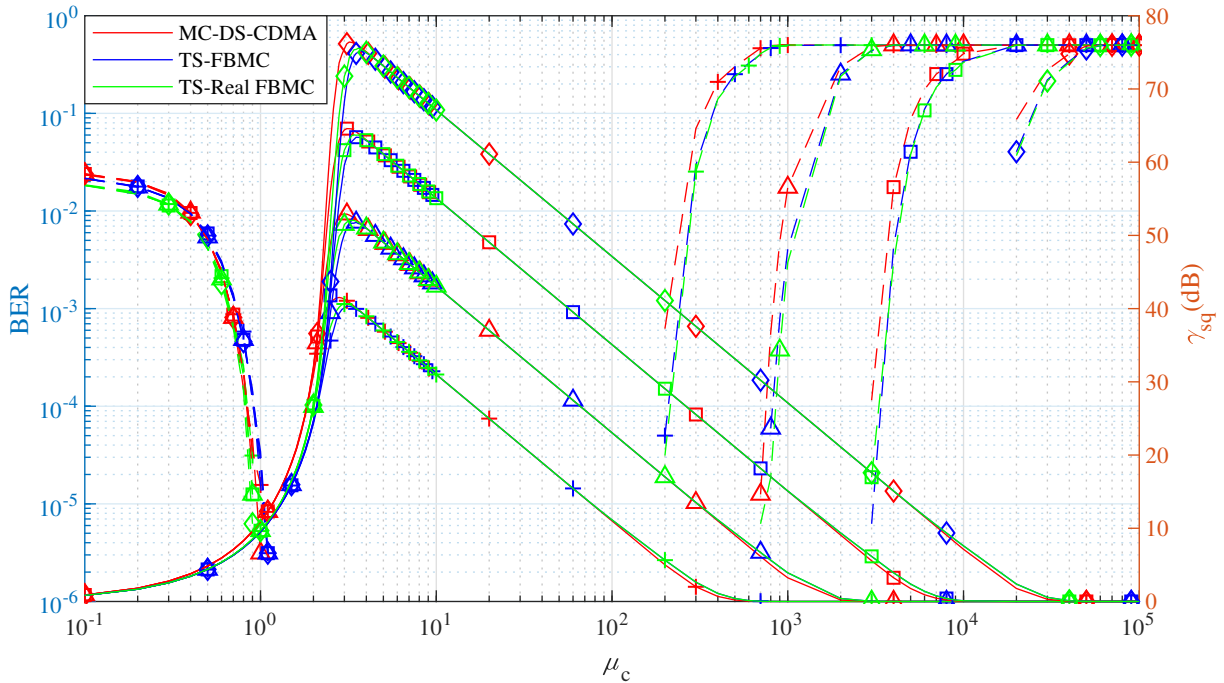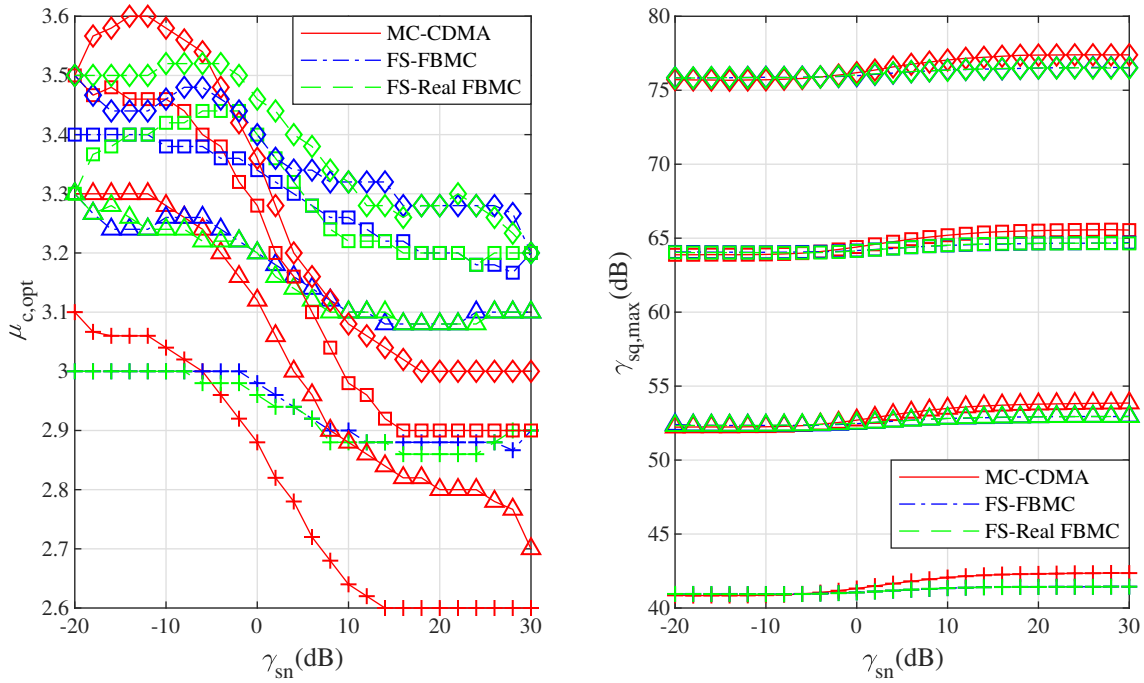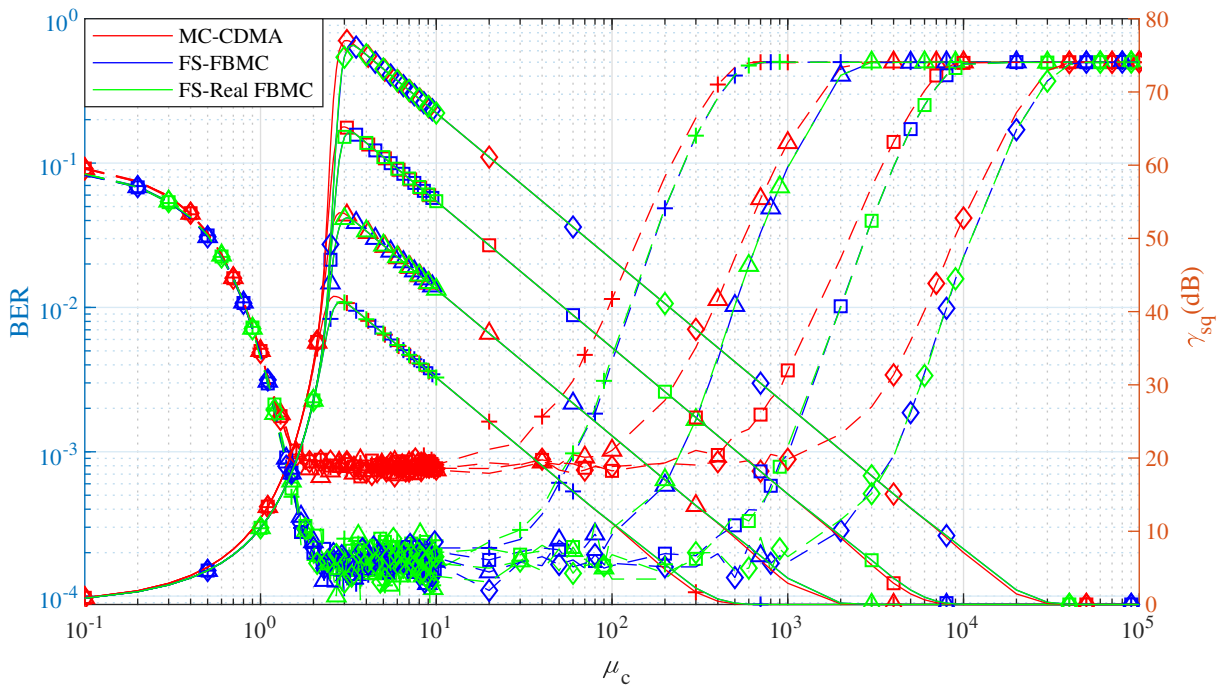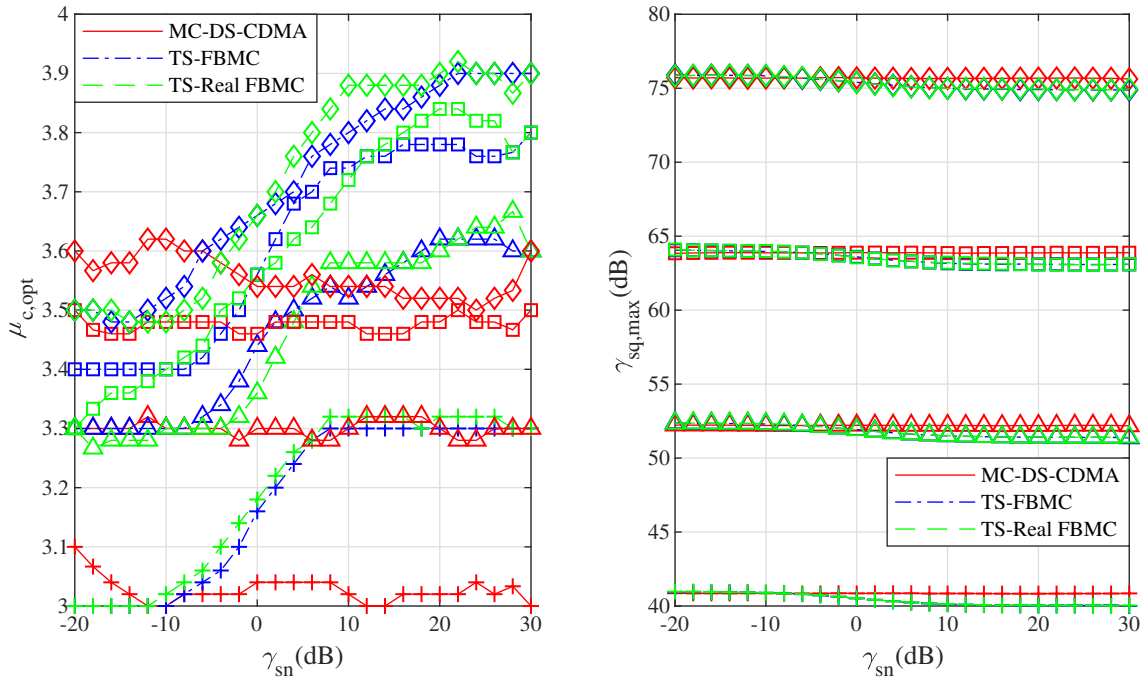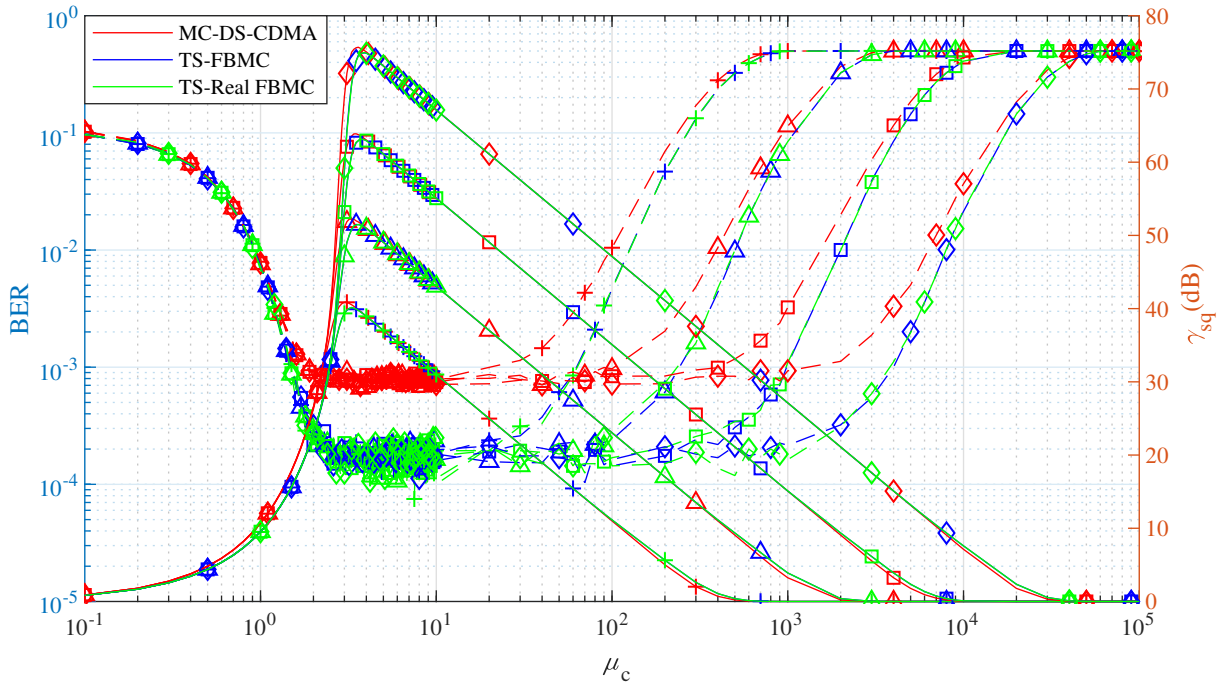

Figure 3.14: BER (dashed) and SQNR (solid) for TS maximum downlink transmission under AWGN, $\gamma_{sn} = 10$dB, $b_{adc} = 8$-bit($+$), 10-bit($\triangle$), 12-bit($\square$), and 14-bit($\diamondsuit$)

3.3   Performance for Industrial Channels

In addition to the parameters which affect the optimal CF and its corresponding SQNR, the effects of the LOS and NLOS industrial propagation channels, which were discussed in the previous chapter, on the performance of the ADC are discussed in this section. As the effect of the ADC resolution was widely shown in the previous section, it is considered to be fixed at 8 bits.

First, when the FS uplink transmission is applied through the industrial propagation channels, it can be seen in Figure 3.15 that the maximum SQNRs are achieved by lower optimal CF values when it is compared to the AWGN scenario. This is caused by the temporal spread of the channel that affects the received signal distribution as discussed in section 2.5. As the SNR increases, it is clear that the maximum SQNR under NLOS is higher than the maximum SQNR under LOS because the NLOS channel creates a more Gaussian distributed received signal. Although MC-CDMA has a higher maximum SQNR at a lower optimal CF, real FS-FBMC usually outperforms MC-CDMA in terms of BER when the SNR is fixed at 10 dB as shown in Figure 3.16.

When TS is applied in the uplink, the maximum SQNR for MC-DS-CDMA increases and can be achieved at a lower optimal CF than TS-FBMC as the SNR increases. On the other hand, it remains relatively constant, as in the no-channel scenario, for both TS-FBMC variants as shown in Figure 3.17. However, when the SNR is fixed at 10 dB as shown in Figure 3.18, MC-DS-CDMA has a similar performance to complex TS-FBMC while real TS-FBMC has the maximum reliability among the tested schemes.

Generally, the downlink operation for FS and TS networks with maximum capacity are similar to their operation without channel effects. When FS is implemented, the optimal CF for the FS-FBMC downlink decreases slightly as the SNR increases. This results in a limited improvement in the maximum SQNR as shown in Figure 3.19. The maximum SQNR under NLOS for FS-FBMC is higher than the maximum SQNR under LOS. In terms of BER, FS-FBMC variants outperform MC-CDMA as shown in Figure 3.20. When TS is implemented in the downlink, the maximum SQNR of TS-FBMC decreases as the SNR increases as shown in Figure 3.21 while the maximum SQNR of MC-DS-CDMA remains almost constant. However, the TS-FBMC variants maintain a better performance than MC-DS-CDMA in terms of BER as shown in Figure 3.22.

For all tested schemes, and as the performance is affected by the propagation channels, it is shown that the CF range which allows an optimal performance in industrial environments is lower than the optimal CF range for AWGN. Therefore, an optimal CF selection becomes more important especially when the ADC resolution is relatively low.

Figure 3.15: Optimal CF and maximum SQNR for FS uplink transmission under LOS (×) and NLOS (○) industrial channels
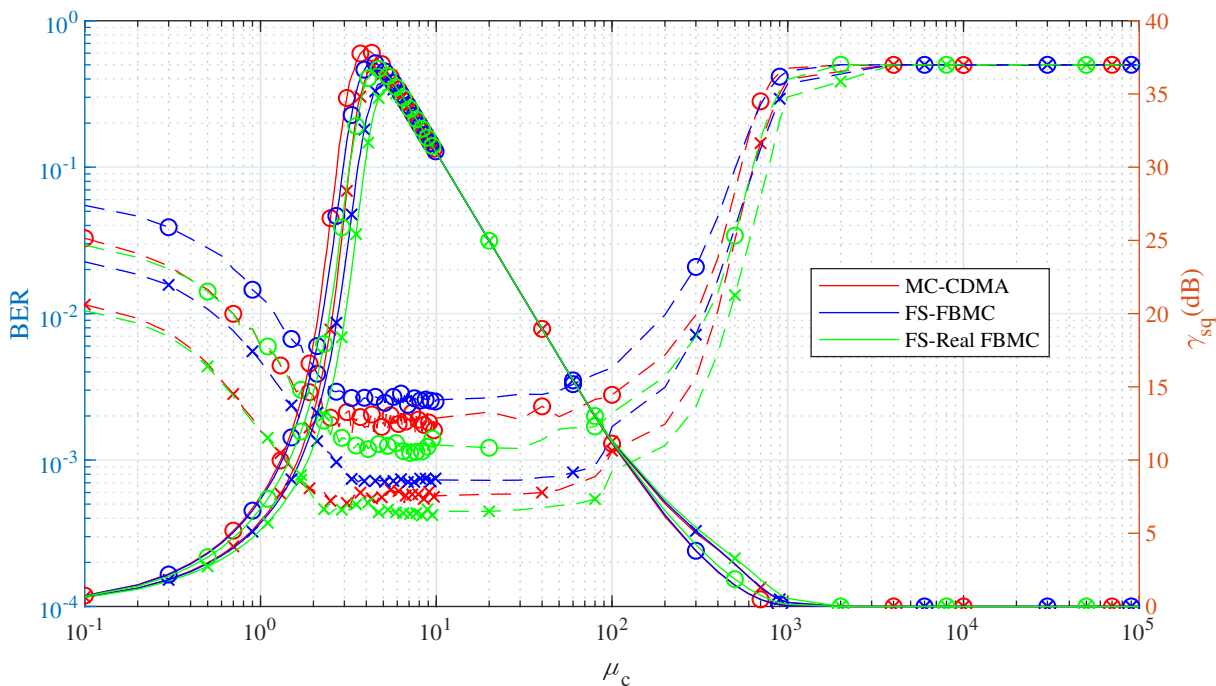
Figure 3.16: BER (dashed) and SQNR (solid) for FS uplink transmission under LOS (×) and NLOS (○) industrial channels, γ_{sn}=10dB
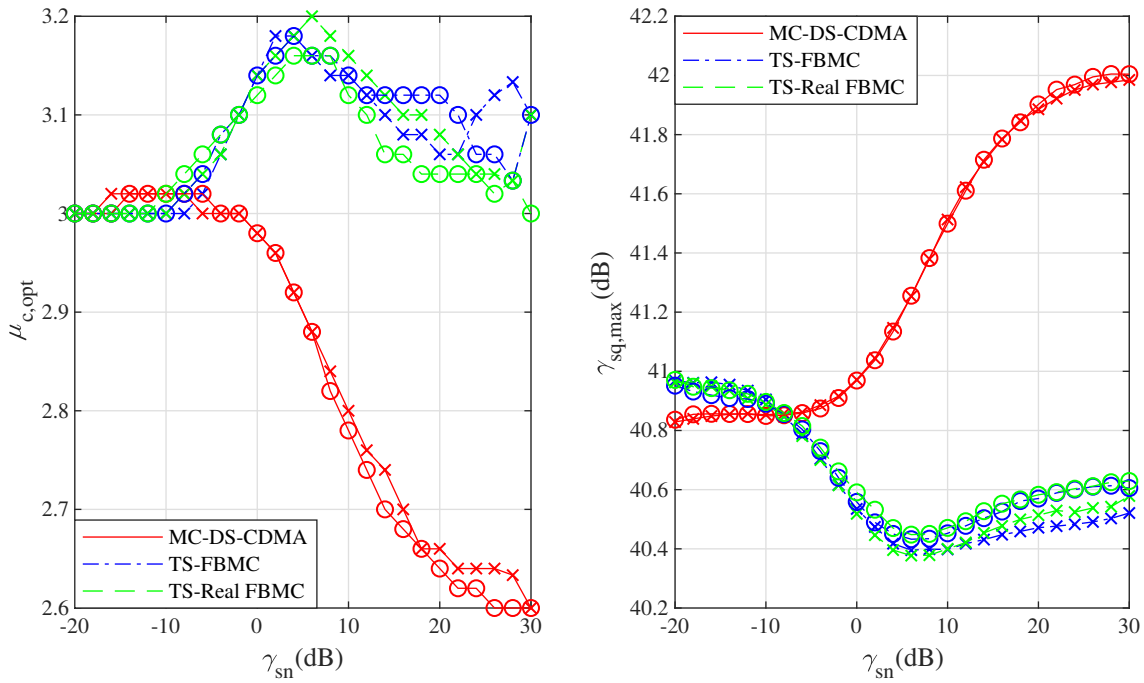
Figure 3.17: Optimal CF and maximum SQNR for TS uplink transmission under LOS (×) and NLOS (○) industrial channels
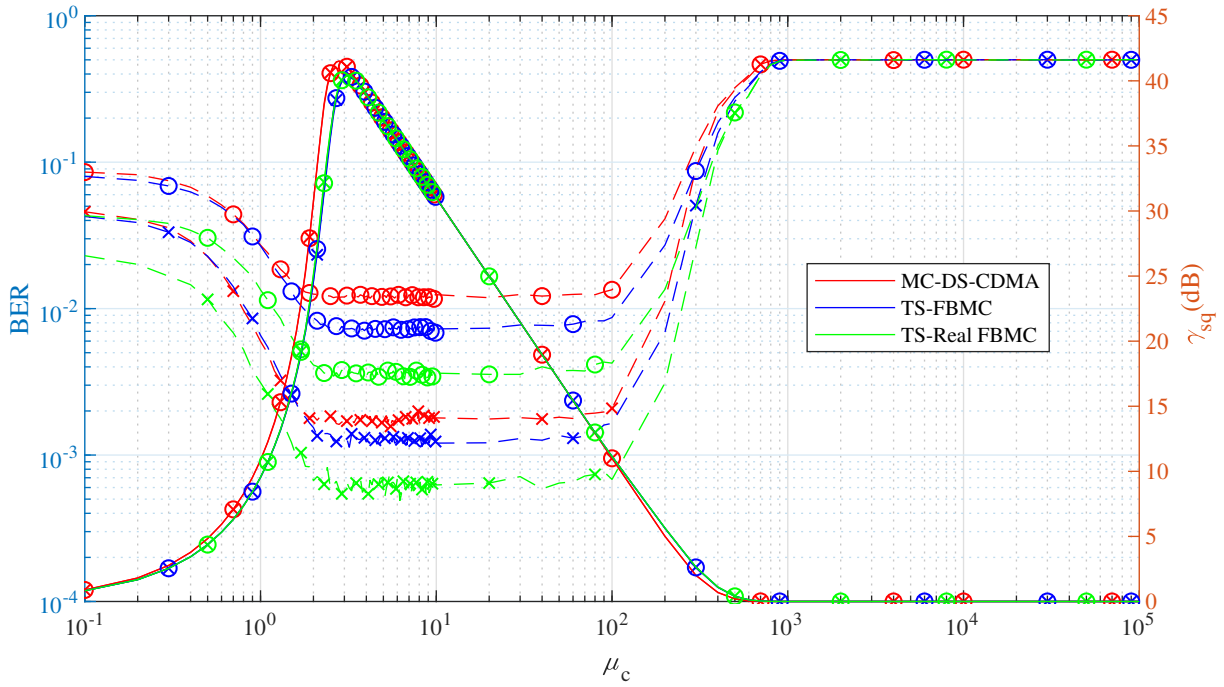
Figure 3.18: BER (dashed) and SQNR (solid) for TS uplink transmission under LOS (×) and NLOS (○) industrial channels, γ_{sn}=10dB
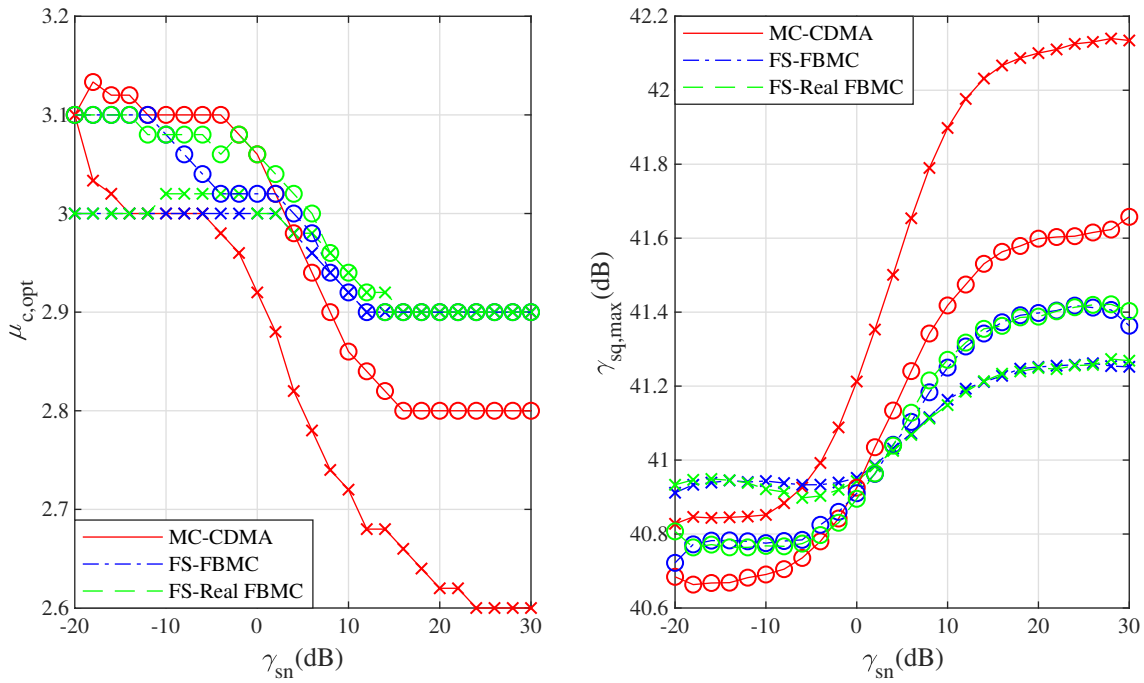
Figure 3.19: Optimal CF and maximum SQNR for FS maximum downlink transmission under LOS (×) and NLOS (○) industrial channels
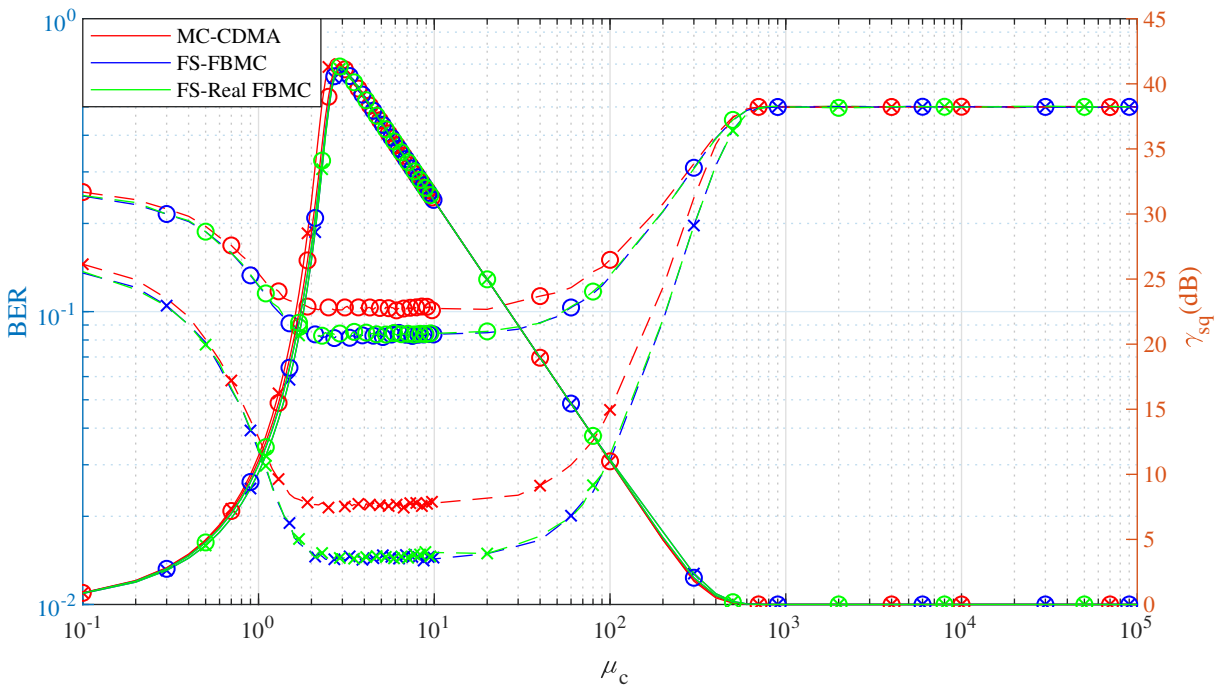
Figure 3.20: BER (dashed) and SQNR (solid) for FS maximum downlink transmission under LOS (×) and NLOS (○) industrial channels, γ_{sn}=10dB
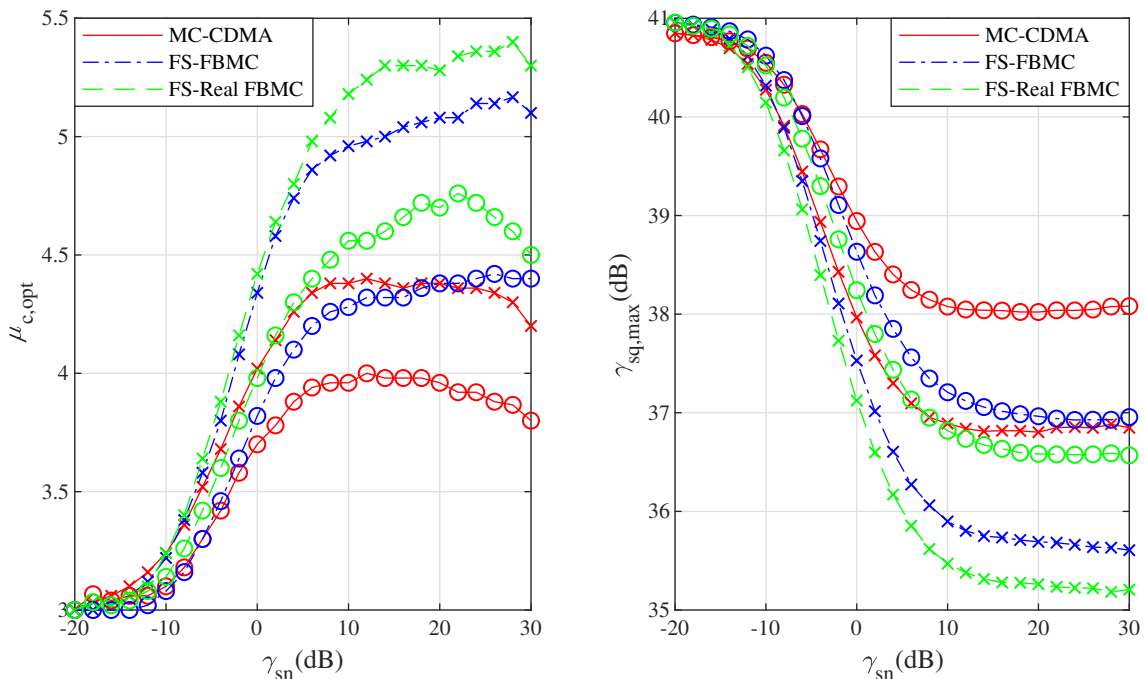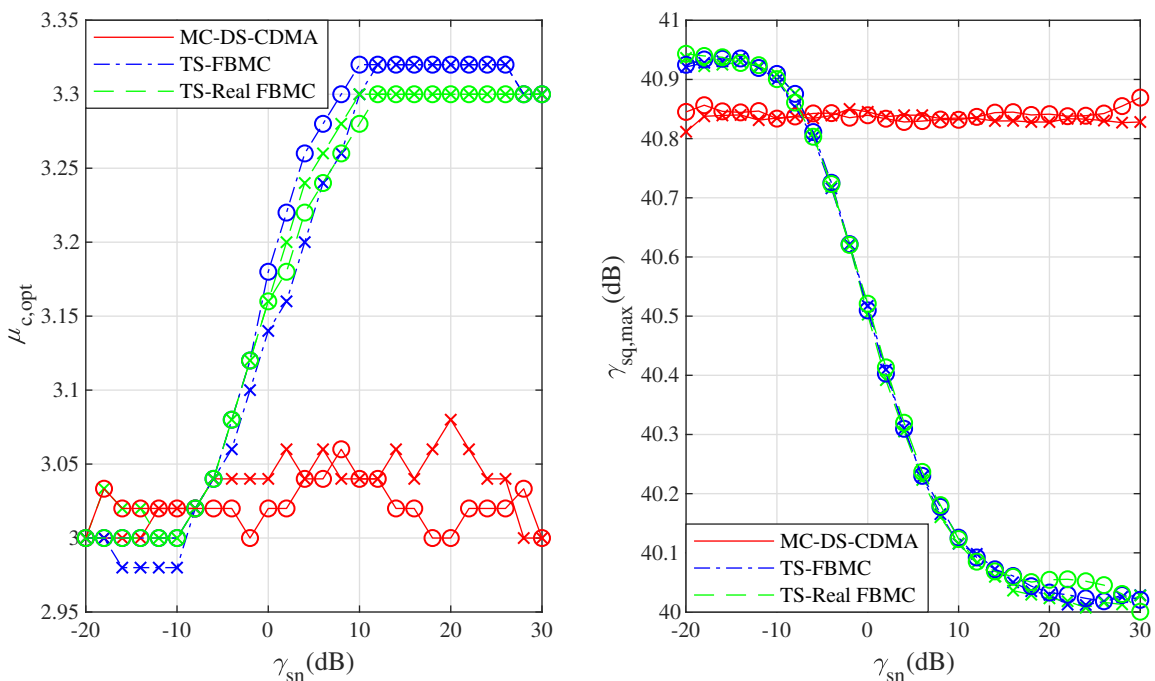
Figure 3.21: Optimal CF and maximum SQNR for TS maximum downlink transmission under LOS (×) and NLOS (○) industrial channels
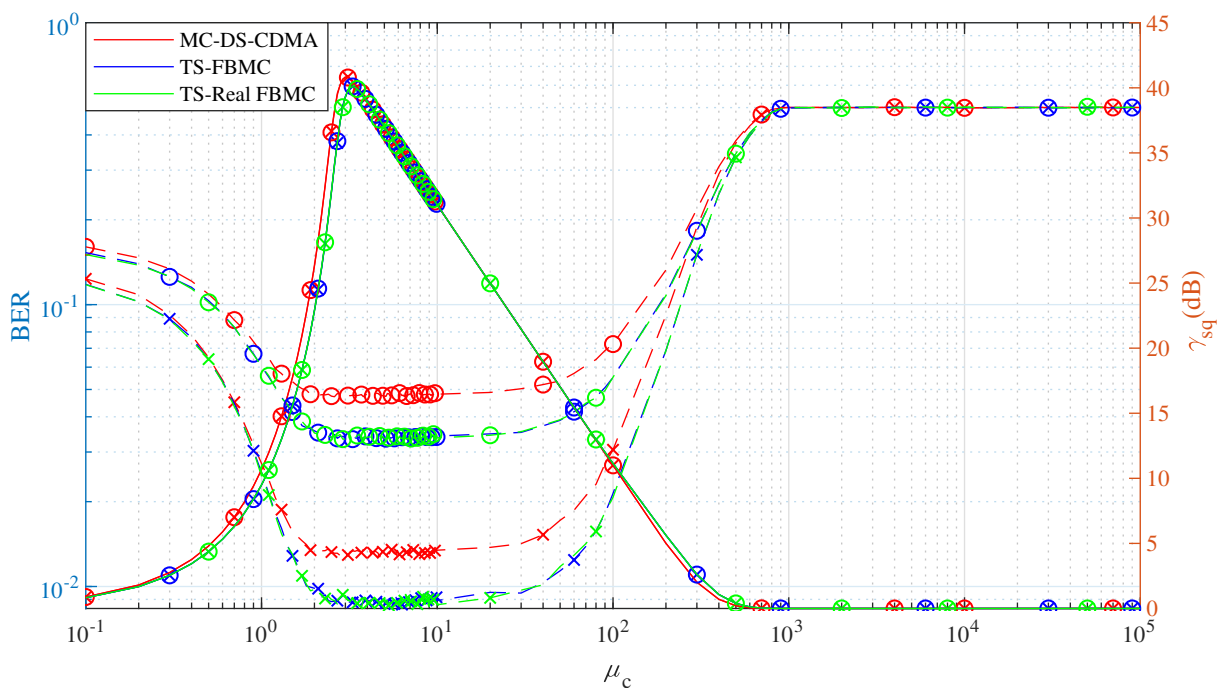
Figure 3.22: BER (dashed) and SQNR (solid) for TS maximum downlink transmission under LOS (×) and NLOS (○) industrial channels, γ_{sn}=10dB

3.4   Summary

This chapter started with a short review of the data conversion in the spread FBMC transmission chain. A short explanation of the DAC resolution and characteristics, which can be affected by several types of errors, was given. Later, it was shown that the PAPR of the PA input must be kept low to ensure a linear operation. The high PAPR, which is usual in the FBMC transmission, also needs a high DAC resolution to minimize the error in the resultant analog signal.

At the receiver, the clipping ADC and its relation to the AGC was explained in details. After the definition of the main quantization and clipping parameters (e.g. CF, SQNR,...), the quantization and clipping effects of the ADC on the spread FBMC transmission were simulated and compared to the performance of the spread OFDM variants without channel effects. These simulations were done for different spreading types, network sizes, SNRs, and ADC resolutions. The results were obtained by finding the average optimal CF for every SNR as well as the corresponding maximum SQNR. Moreover, for a fixed SNR of 10 dB, the performance of all transmission schemes were tested for a wide range of CFs to show how the ADC performance affects the BER. In these simulations, spread FBMC variants usually outperform spread OFDM schemes.

Afterwards, the quantization and clipping errors were investigated for the industrial propagation channels which were discussed in chapter 2. Several differences from the AWGN scenario were found as a result of the received signal distribution being affected by the channel. However, the behavior of optimal CF (and the corresponding maximum SQNR) vs SNR remains quite similar to the simulation without channel effects in most cases.

It was proven in this chapter that the quantization and clipping effects, especially with extreme low or high CF values, can cause a high BER. It was also proven that the importance of the suitable CF selection increases as the ADC resolution decreases and if the transmission is done through fading channels.

Chapter 4

Spread FBMC for Jamming Interference

In this chapter, the performance of spread FBMC transmission is investigated under the influence of jamming. To avoid the quantization error, which can cause a high BER if the clipping level is not properly selected, the receiver is set to operate on a CF that generates the first SQNR peak. Afterwards, the performance for noise jamming, where White Gaussian Noise (WGN) is used as the jamming signal, is discussed. In noise jamming, Barrage Noise Jamming (BNJ) is implemented as a wide band jamming technique while Partial Band jamming (PBJ) is discussed as a method of narrow band jamming. Next, several types of tone jamming are applied to the system to test its reliability. Tone jamming techniques are separated into continuous and time-variant techniques. Moreover, the effect of CFO between the system and the tone jamming signals is investigated.

4.1   System Model

As shown in Figure 4.1, the spread FBMC signal is sent through the system channel. At the spread FBMC receiver, the received spread FBMC signal is affected by two sources of interference. The AWGN $w(t)$ and the jamming signal $j(t)$ which is sent through the jammer channel with a CIR of $h_j(t)$. Therefore, the received signal can be described by:

$$r(t) = \underbrace{s(t) * h_s(t)}_{r_s(t)} + \underbrace{j(t) * h_j(t)}_{r_j(t)} + w(t) \,. \tag{4.1}$$

In this case, the JSR γ_{js} at the receiver can be mathematically represented as:

$$\gamma_{js} = \frac{\mathrm{E}\{|r_j(t)|^2\}}{\mathrm{E}\{|r_s(t)|^2\}} \,. \tag{4.2}$$
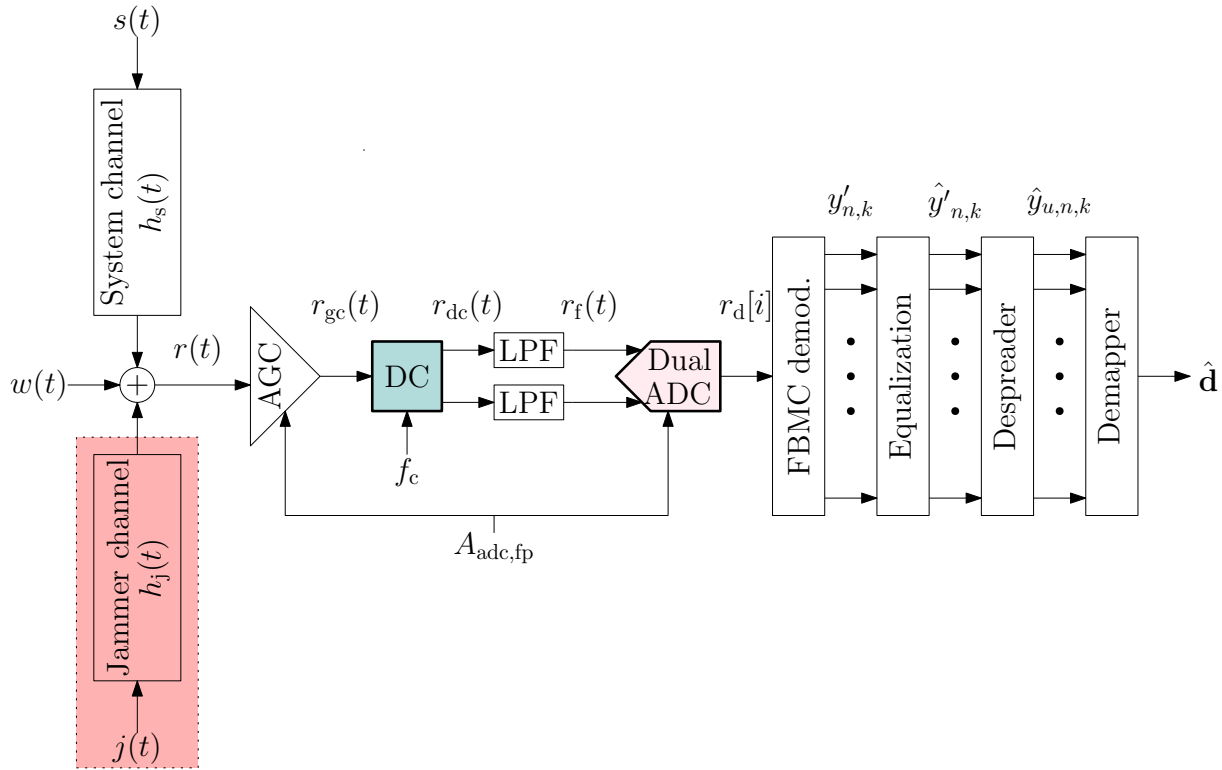
Figure 4.1: Spread FBMC receiver under the influence of jamming

As illustrated in Figure 4.2, it is possible to have a time offset Δk_{s} and a frequency offset Δn_{s} between the transmitter and the receiver. Offsets in time Δk_{j} and in frequency Δn_{j} can also be present between the jamming signal and the receiver. The effect of off-tone jamming, where a CFO is present between the system subcarriers and the jamming tones, on spread FBMC was investigated in [25] where both system and jamming signals were assumed to be timely synchronized with the receiver.

In this chapter, the performances of spread FBMC and spread OFDM variants are compared for several jamming techniques using the industrial propagation channels which were applied in the previous chapters. The simulation parameters are shown in Table 4.1.

Number of subcarriers	32	Number of symbols	32
Modulation type	QPSK	Spreading code	32 bit W-H
FBMC sampling frequency	20 MHz	Filter type	PHYDYAS
OFDM sampling frequency	10 MHz	CP duration	1/16 OFDM symbol
Overlapping factor	4	Number of iterations	10000
SNR	20dB	Equalization	1-tap ZF
System CFO (Δn_{s})	0	System TO (Δk_{s})	0

Table 4.1: Simulation parameters for spread FBMC for jamming interference
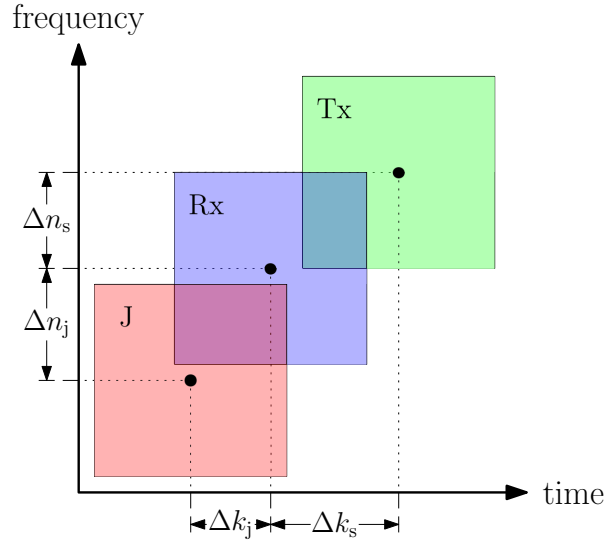
Figure 4.2: System and jammer offsets in time and frequency, Δk_s is the system time offset, Δk_j is the jammer time offset, Δn_s is the system frequency offset, and Δn_j is the jammer frequency offset

4.2   Performance under Noise Jamming

The most basic noise jammer is the BNJ where the jamming signal occupies the whole system bandwidth. When WGN is used as a jamming signal, the sampled BNJ output $j_\mathrm{bn}(k)$ is given by:

$$j_\mathrm{bn}(k) = \sqrt{\frac{P_\mathrm{bn}}{2}} \left[x_\mathrm{r}(k) + \mathrm{j}x_\mathrm{i}(k) \right] , \tag{4.3}$$

where P_bn is the power of the BNJ, $x_\mathrm{r}(k)$ and $x_\mathrm{i}(k)$ are zero-mean unity-variance Gaussian variables which represent the real and the imaginary noise components, respectively. The BNJ is considered as an ineffective jamming technique since its PSD $\breve{S}_\mathrm{bn}$ is inversely proportional to the total system bandwidth as:

$$\breve{S}_\mathrm{bn} = \frac{P_\mathrm{bn}}{B_\mathrm{s}} . \tag{4.4}$$

The wideband distribution as shown in Figure 4.3 can also waste the jammer power on guard subcarriers that do not contain any information. Therefore, as discussed in [18] and [145], PBJ focuses the jammer power on a selected bandwidth B_pb so that [18]:

$$\rho_\mathrm{pb} = \frac{B_\mathrm{pb}}{B_\mathrm{s}} , \tag{4.5}$$

where $0 < \rho_\mathrm{pb} \leq 1$ is the ratio between the PBJ bandwidth and the system bandwidth. According to Figure 4.3, f_h and f_l are the high and low frequency limits of the PBJ signal, respectively, so that $B_\mathrm{pb} = f_\mathrm{h} - f_\mathrm{l}$.
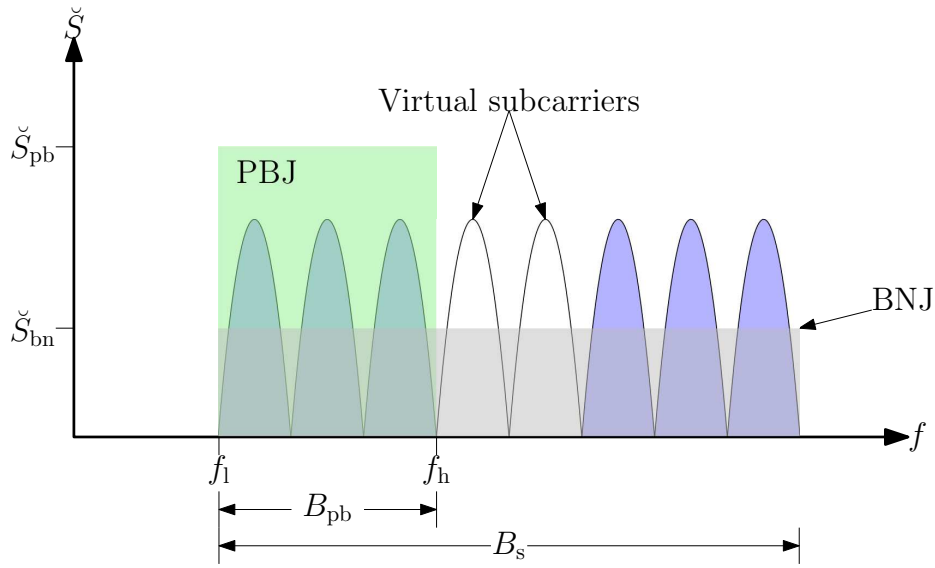
Figure 4.3: PSD of noise jamming variants

For a fixed noise jammer power $P_{nj} = P_{bn} = P_{pb}$, where P_{pb} is the PBJ power, the PSD of the PBJ $\breve{S}_{pb}$ increases by the factor of $\frac{1}{\rho_{pb}}$ compared to the BNJ as:

$$\breve{S}_{pb} = \frac{P_{pb}}{B_{pb}} = \frac{P_{nj}}{\rho_{pb}B_s} = \frac{\breve{S}_{bn}}{\rho_{pb}}. \tag{4.6}$$

The performance of the spread FBMC uplink under BNJ, which is shown Figure 4.4, shows that spreading in time or frequency enhances the reliability of the transmission significantly. When complex spreading is applied, the uplink becomes less reliable since the orthogonality is not perfectly restored as a different spreading code is used in each iteration. However, in the downlink operation, and as the network size increases to its maximum level, the reliability of complex spread FBMC improves to be comparable to real spread FBMC variants as shown in Figure 4.5. Moreover, real spread FBMC outperforms all other schemes under the industrial propagation channel models.

The worst case jamming for any JSR level is obtained by jamming a certain number of subcarriers so that the BER is maximized. When the worst case PBJ is applied as shown in Figure 4.6 for the uplink, and Figure 4.7 for the maximum-sized downlink network, it can be seen that the BER is higher than the BER caused by BNJ, especially when TS is applied without channel effect. In this case, MC-DS-CDMA becomes more reliable than TS-FBMC since the symbol overlapping causes more FBMC symbols to be interfered. Moreover, the perfect time localization of the OFDM symbols gives an advantage for OFDM when TS is applied. Under the effect of the LOS [22] and NLOS channels, real spread FBMC outperforms OFDM variants when the uplink case is tested. In the maximum-sized downlink, both spread FBMC variants are more reliable than the OFDM based schemes. For BNJ and PBJ simulations, $\Delta k_j = 0$ and $\Delta n_j = 0$.

(a) FS
(b) TS

Figure 4.4: Uplink BER for BNJ without channel effect (no marker), LOS (×) [22], and NLOS (○) as a function of the jammer-to-signal power ratio γ_{js}

(a) FS
(b) TS

Figure 4.5: Downlink BER for BNJ without channel effect (no marker), LOS (×) [22], and NLOS (○) as a function of the jammer-to-signal power ratio γ_{js}

(a) FS   (b) TS

Figure 4.6: Uplink BER for worst case PBJ without channel effect (no marker), LOS (×) [22], and NLOS (○) as a function of the jammer-to-signal power ratio γ_{js}

(a) FS   (b) TS

Figure 4.7: Downlink BER for worst case PBJ without channel effect (no marker), LOS (×) [22], and NLOS (○) as a function of the jammer-to-signal power ratio γ_{js}

4.3 Performance under Continuous Tone Jamming

The basic type of tone jamming, which is a continuous complex Single Tone Jamming (STJ) signal $j_{\mathrm{st}}(k)$ can be mathematically represented as:

$$j_{\mathrm{st}}(k) = \sqrt{\frac{P_{\mathrm{tj}}}{2}} \mathrm{e}^{\mathrm{j}\left[2\pi(k+\Delta k_{\mathrm{j}})\frac{(n_{\mathrm{j}}+\Delta n_{\mathrm{j}})}{N}+\theta_{n_{\mathrm{j}}}\right]}, \tag{4.7}$$

where P_{tj} is the power of the tone jamming, n_{j} is the index of the jammed subcarrier, and $\theta_{n_{\mathrm{j}}}$ is the phase of the jamming tone. For the case when all subcarriers are jammed, known as All Tone Jamming (ATJ), by the same amount of power, the ATJ signal $j_{\mathrm{at}}(k)$ is given by:

$$j_{\mathrm{at}}(k) = \sqrt{\frac{P_{\mathrm{tj}}}{2N}} \sum_{n_{\mathrm{j}}=0}^{N-1} \mathrm{e}^{\mathrm{j}\left[2\pi(k+\Delta k_{\mathrm{j}})\frac{(n_{\mathrm{j}}+\Delta n_{\mathrm{j}})}{N}+\theta_{n_{\mathrm{j}}}\right]}, \tag{4.8}$$

The ATJ is similar to the BNJ since it attacks all subcarriers by tones instead of noise. However, this can, from the jammer point of view, waste a significant amount of the jamming power by the jamming of unused subcarriers. Therefore, as shown in Figure 4.8, MTJ was implemented to attack a certain number of subcarriers starting from a low-index subcarrier n_{l} to a higher index subcarrier n_{h} as:

$$j_{\mathrm{mt}}(k) = \sqrt{\frac{P_{\mathrm{tj}}}{2N_{\mathrm{j}}}} \sum_{n_{\mathrm{j}}=n_{\mathrm{l}}}^{n_{\mathrm{h}}} \mathrm{e}^{\mathrm{j}\left[2\pi(k+\Delta k_{\mathrm{j}})\frac{(n_{\mathrm{j}}+\Delta n_{\mathrm{j}})}{N}+\theta_{n_{\mathrm{j}}}\right]}, \tag{4.9}$$

where $j_{\mathrm{mt}}(k)$ is the MTJ signal and N_{j} is the total number of jammed subcarriers. For MTJ, $N_{\mathrm{j}} = n_{\mathrm{h}} - n_{\mathrm{l}} + 1$. The ratio between the number of jammed tones to the number of the system subcarriers ρ_{mt} is given by [18]:

$$\rho_{\mathrm{mt}} = \frac{N_{\mathrm{j}}}{N}, \tag{4.10}$$

where $0 < \rho_{\mathrm{mt}} \leq 1$. In this case, the PSD of the MTJ $\breve{S}_{\mathrm{mt}}$ increases on the attacked subcarriers, when it is compared to ATJ, by $1/\rho_{\mathrm{mt}}$ as:

$$\breve{S}_{\mathrm{mt}} = \frac{P_{\mathrm{mt}}}{N_{\mathrm{j}}} = \frac{P_{\mathrm{tj}}}{N\rho_{\mathrm{mt}}} = \frac{\breve{S}_{\mathrm{at}}}{\rho_{\mathrm{mt}}}, \tag{4.11}$$

where $\breve{S}_{\mathrm{at}}$ is the PSD of the ATJ. Moreover, the N_{j} jamming tones can be randomly distributed in a subset $N'_{\mathrm{rj}} \subseteq \{0, \cdots, N-1\}$ of the system subcarriers as shown also in Figure 4.8. The Random MTJ (RMTJ) signal $j_{\mathrm{rmt}}(k)$ is obtained by:

$$j_{\mathrm{rmt}}(k) = \sqrt{\frac{P_{\mathrm{tj}}}{2N_{\mathrm{j}}}} \sum_{n_{\mathrm{j}} \in N'_{\mathrm{rj}}} \mathrm{e}^{\mathrm{j}\left[2\pi(k+\Delta k_{\mathrm{j}})\frac{(n_{\mathrm{j}}+\Delta n_{\mathrm{j}})}{N}+\theta_{n_{\mathrm{j}}}\right]}. \tag{4.12}$$
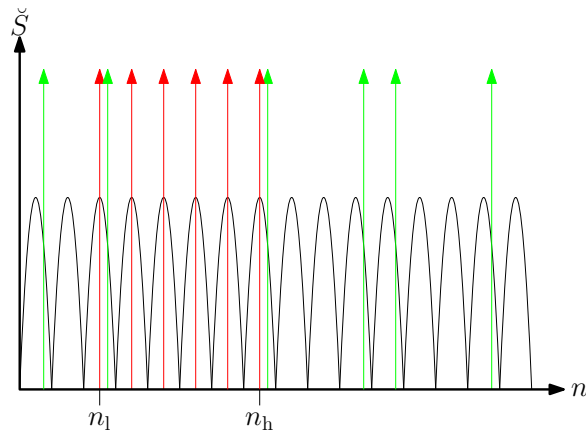
Figure 4.8: PSD of MTJ (orange) and off-tone RMTJ with a fixed $\Delta n_{\mathrm{j}} = 0.25$ (green)

When FS is applied in the uplink, real FS-FBMC outperforms MC-CDMA when both systems are attacked by ATJ as shown in Figure 4.9(a). However, when TS is applied, it can be seen that as the JSR increases, MC-DS-CDMA outperforms TS-FBMC variants as shown in Figure 4.9(b) because of the perfect time localization of OFDM. Similarly, when the downlink scenario is simulated for the maximum number of users as shown in Figure 4.10, FS-FBMC outperforms MC-CDMA while MC-DS-CDMA is usually more reliable than TS-FBMC variants when ATJ is applied with a moderate or high JSR.

Under the worst case MTJ, it is assumed that the jamming tones start from the center of the targeted channel. Compared to ATJ, MTJ usually causes a higher BER as shown in Figure 4.11 and Figure 4.12. FS-FBMC shows a better performance when it is compared to MC-CDMA unless when complex FS-FBMC is used in the uplink. When TS is applied in the uplink and in the maximum-sized downlink transmission, MC-DS-CDMA outperforms TS-FBMC as the JSR increases. Due to the positions of the jamming tones, the worst case MTJ results are slightly different from the results of [22] where it was assumed that the jamming tones are starting from the subcarrier with the lowest frequency.

The effect of the positions of the jamming tones can also be seen in Figure 4.13 and Figure 4.14. This can be found when the performance for the worst case RMTJ, where the jamming tones are randomly selected for each iteration, is compared to the worst case MTJ results for TS schemes. It is shown that a higher BER is caused by MTJ and the performance of RMTJ is more similar to the performance under ATJ when the JSR is high. As the JSR increases when TS is implemented, it can be proven that MC-DS-CDMA usually outperforms TS-FBMC variants. When FS is applied, the worst case performance under RMTJ is similar to the performance under MTJ. For tone jamming methods, the worst case jamming is achieved by targeting a certain number of subcarriers. This number is dependent on the JSR level and the applied jamming technique as discussed in [18]. All continuous tone jamming signals are assumed to have $\Delta k_{\mathrm{j}} = 0$ and $\Delta n_{\mathrm{j}} = 0$.

(a) FS

(b) TS
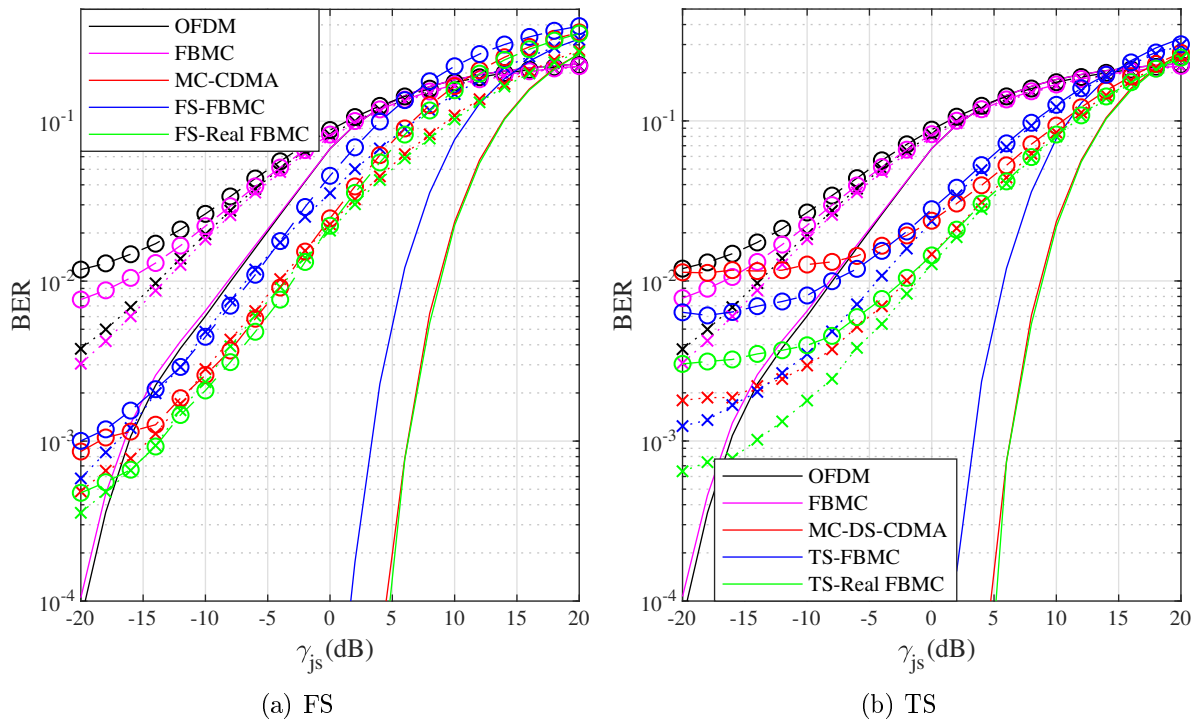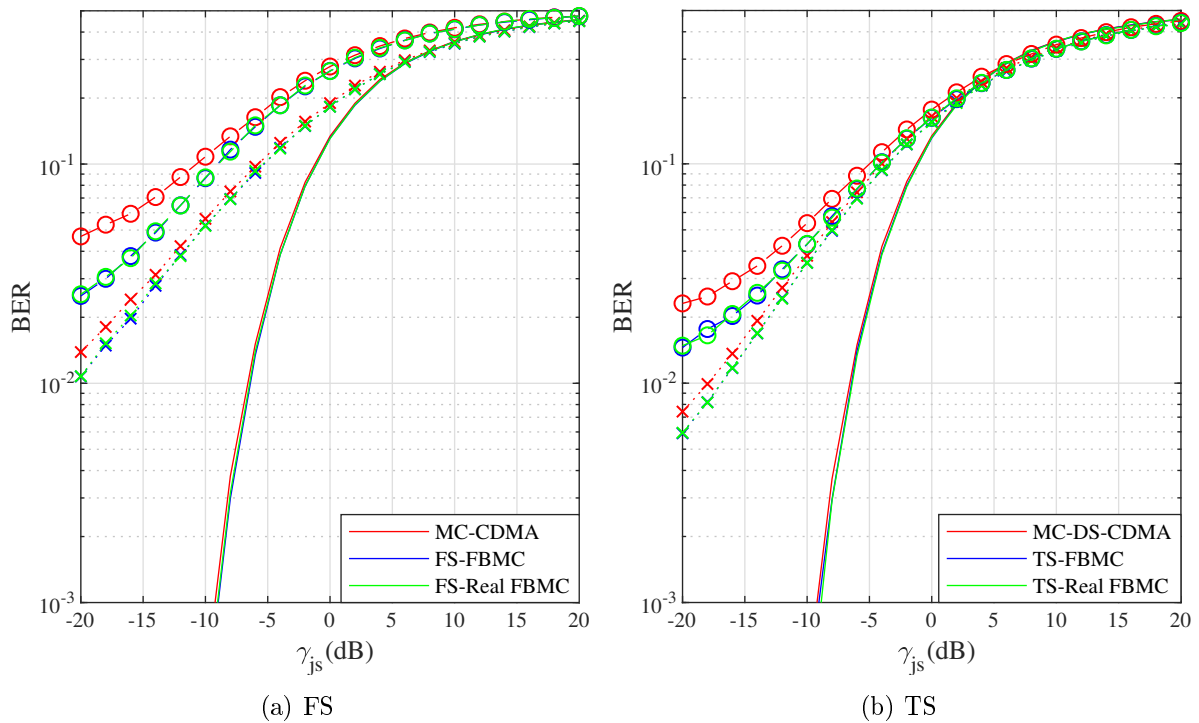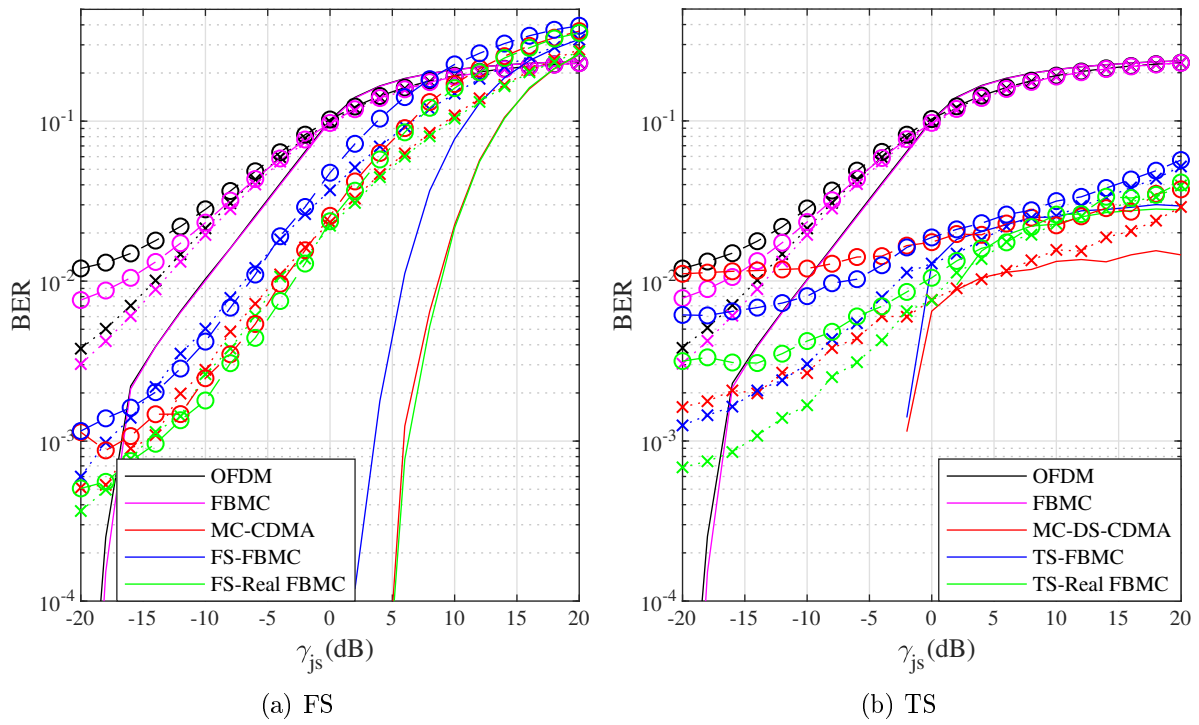
Figure 4.9: Uplink BER for ATJ without channel effect (no marker), LOS (×), and NLOS (○) as a function of the jammer-to-signal power ratio γ_{js}

(a) FS

(b) TS
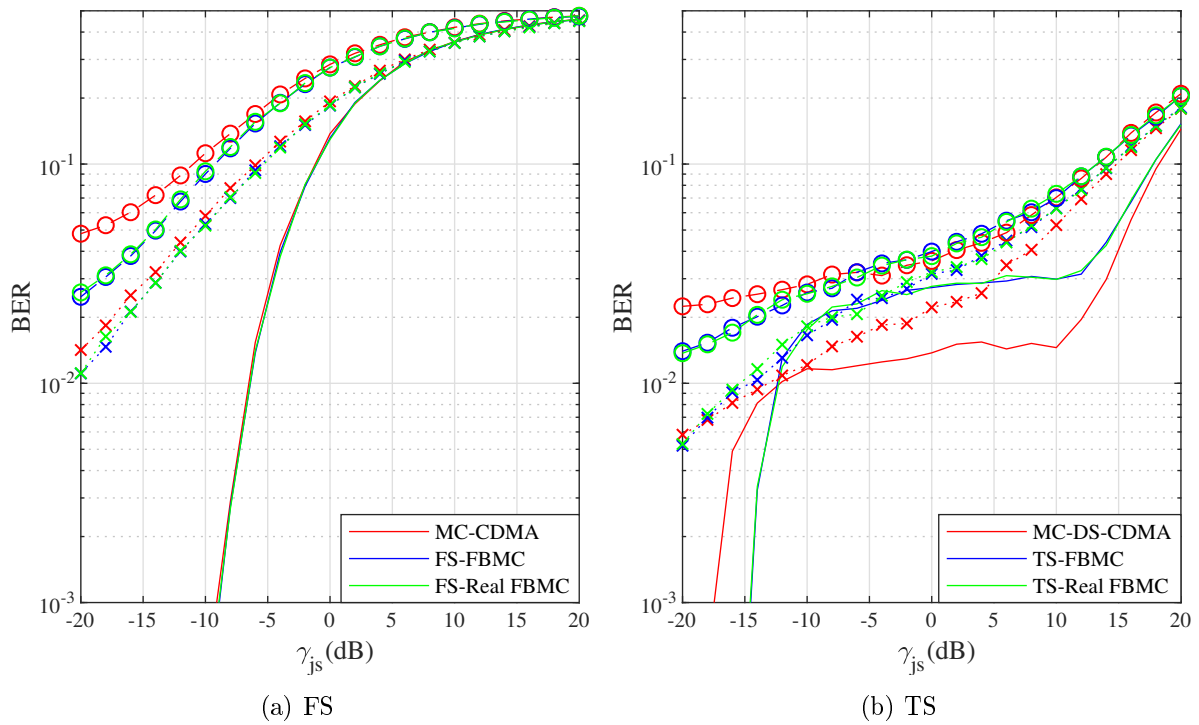
Figure 4.10: Downlink BER for ATJ without channel effect (no marker), LOS (×), and NLOS (○) as a function of the jammer-to-signal power ratio γ_{js}

(a) FS
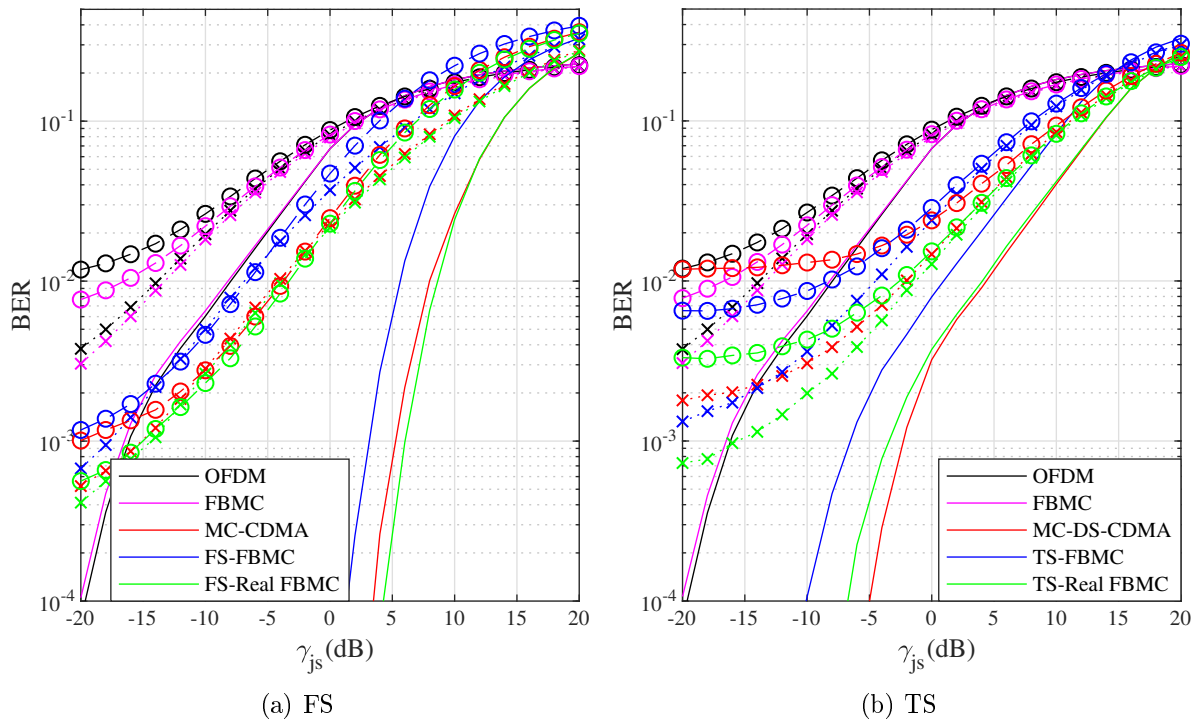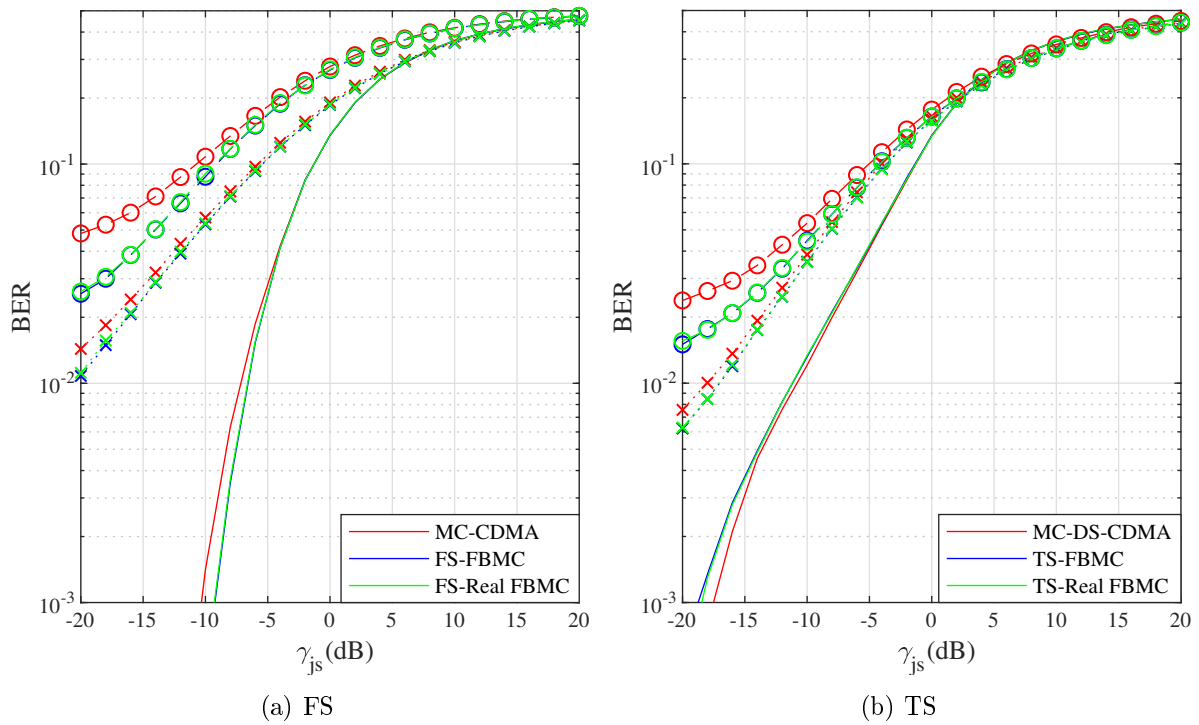
(b) TS

Figure 4.11: Uplink BER for worst case MTJ without channel effect (no marker), LOS (×), and NLOS (○) as a function of the jammer-to-signal power ratio γ_{js}

(a) FS

(b) TS

Figure 4.12: Downlink BER for worst case MTJ without channel effect (no marker), LOS (×), and NLOS (○) as a function of the Jammer-to-Signal power Ratio γ_{js}

Figure 4.13: Uplink BER for worst case RMTJ without channel effect (no marker), LOS ($\times$), and NLOS ($\circ$) as a function of the jammer-to-signal power ratio γ_{js}

Figure 4.14: Downlink BER for worst case RMTJ without channel effect (no marker), LOS ($\times$), and NLOS ($\circ$) as a function of the jammer-to-signal power ratio γ_{js}

4.4   Performance under Time-Variant Tone Jamming

In addition to the previous jamming techniques, the effects of Sweep Multitone Jamming (SMTJ) and Random Frequency Hopping Jamming (RHFJ) are investigated. From the jammer point of view, and since the jammer power is usually limited, time-variant jamming is an effective way to attack a wide range of frequencies with a significant decrease in the power consumption. It may also reduce the need of reactive jamming against systems with dynamic spectrum utilization. However, this type of jamming requires the optimization of the jamming bandwidth and duration to maximize the BER.

In the case of SMTJ, it is assumed that the jammer has an ascending linear sweep as shown in Figure 4.15(a). The SMTJ signal consists of N_{j} jamming tones where N_{j}/N assumed to be an integer. These tones have a duration of K_{j} FBMC samples. The output of the SMTJ $j_{\mathrm{smt}}(k)$ can be obtained by:

$$j_{\mathrm{smt}}(k) = \sqrt{\frac{P_{\mathrm{tj}}}{2N_{\mathrm{j}}}} \sum_{n_{\mathrm{j}}=\mathrm{mod}\left(\frac{\beta_{\mathrm{smt}}N_{\mathrm{j}}}{N}\right)}^{\mathrm{mod}\left[\frac{(\beta_{\mathrm{smt}}+1)N_{\mathrm{j}}-1}{N}\right]} \mathrm{e}^{\mathrm{j}\left[2\pi(k+\Delta k_{\mathrm{j}})\frac{\left(n_{\mathrm{j}}+\Delta n_{\mathrm{j}}\right)}{N}+\theta_{n_{\mathrm{j}}}\right]}, \qquad (4.13)$$

where $\beta_{\mathrm{smt}} = \lfloor \frac{k}{K_{\mathrm{j}}} \rfloor$ represents the SMTJ sweep index.

In the case of RFHJ, which is shown in Figure 4.15(b), the jammer transmits N_{j} random jamming tones every K_{j} FBMC samples. Each group of tones are randomly distributed in a subset $N'_{\mathrm{rfh},\beta_{\mathrm{rfh}}} \subseteq \{0,\cdots,N-1\}$ where $\beta_{\mathrm{rfh}} = \lfloor \frac{k}{K_{\mathrm{j}}} \rfloor$ is the RFHJ cycle index. The output of the RFHJ $j_{\mathrm{rfh}}(k)$ is given by:

$$j_{\mathrm{rfh}}(k) = \sqrt{\frac{P_{\mathrm{tj}}}{2N_{\mathrm{j}}}} \sum_{n_{\mathrm{j}}\in N'_{\mathrm{rfh},\beta_{\mathrm{rfh}}}} \mathrm{e}^{\mathrm{j}\left[2\pi(k+\Delta k_{\mathrm{j}})\frac{\left(n_{\mathrm{j}}+\Delta n_{\mathrm{j}}\right)}{N}+\theta_{n_{\mathrm{j}}}\right]}. \qquad (4.14)$$

Since most time-variant jamming applications do not attack the whole system bandwidth at a certain time, both jamming types were simulated to find the worst case jamming when up to 8 subcarriers are jammed with sweep or hopping tones. K_{j} is assumed to be 1 sample for all transmission schemes. Moreover, jamming signals are assumed to be perfectly synchronized in time and frequency with the attacked systems.

In Figure 4.16, SMTJ is used to attack the uplink transmission. It is shown that real spread FBMC variants usually outperform spread OFDM when the same spreading is applied in the tested industrial environments. When the effect of the transmission channel is neglected, MC-DS-CDMA usually outperforms TS-FBMC unless both systems are attacked by a high JSR($>$ 12dB).
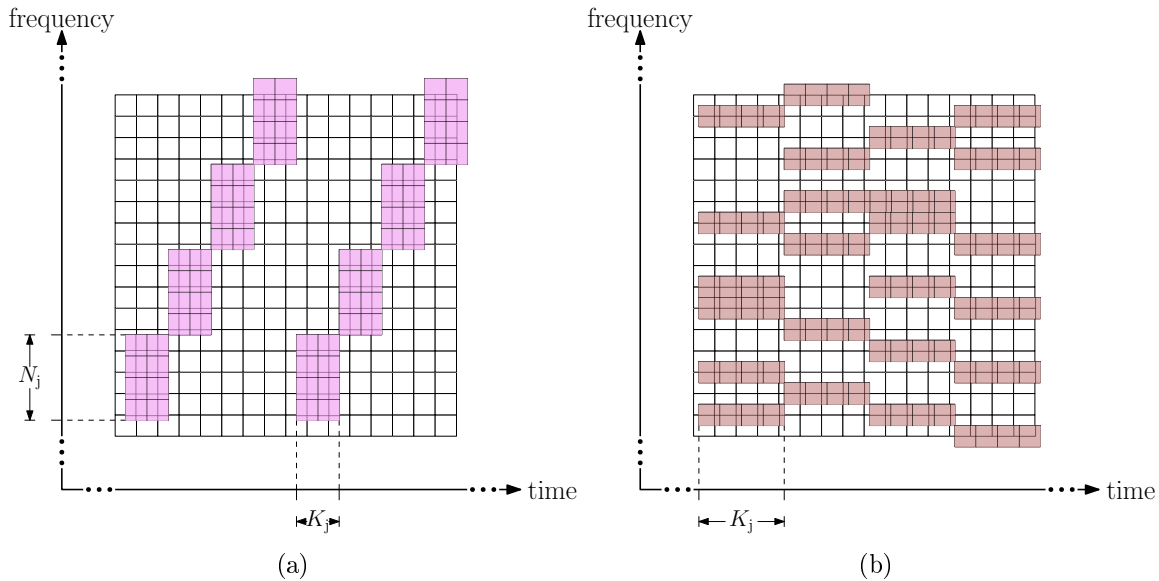
Figure 4.15: Time-variant tone jamming attacks on a multicarrier system with $N = 16$ subcarriers and $K = 16$ samples. (a) SMTJ, $N_j = 4$, $K_j = 2$, $\Delta n_j = 0.75$, and $\Delta k_j = 0.5$. (b) RFHJ, $N_j = 6$, $K_j = 4$, $\Delta n_j = 0.5$, and $\Delta k_j = 0.25$

Figure 4.17 shows the performance of the maximum-sized downlink under SMTJ attack. When no channel effect is taken in consideration, FS-FBMC slightly outperforms MC-CDMA. When TS is applied, MC-DS-CDMA is more reliable than TS-FBMC schemes when they are attacked by a low JSR interference. However, as the JSR increases, TS-FBMC outperforms MC-DS-CDMA.

When FS-FBMC is used in the uplink transmission under the influence of RFHJ, it is shown in Figure 4.18(a) that its performance is similar to the performance under SMTJ and real FS-FBMC is usually the most reliable transmission. However, when TS is applied as shown in Figure 4.18(b), and similar to the SMTJ attack without considering the channel effect, MC-DS-CDMA outperforms real TS-FBMC when the JSR < 6dB. Moreover, for BER = 10^{-3}, the spreading gain for TS-FBMC variants under RFHJ is lower than the spreading gain under SMTJ. Under the tested industrial channels, real TS-FBMC usually outperforms other schemes.

It can be obtained from the downlink performance with the maximum network size, shown in Figure 4.19, that spread FBMC outperforms spread OFDM variants if the industrial propagation channels are applied. Without the channel effect, FS-FBMC slightly outperforms MC-CDMA while TS-FMBC has a similar performance to MC-DS-CDMA. It can also be seen that RFHJ causes higher BER than SMTJ. The results under time-variant jamming show that spreading is less effective in the enhancement of the spread FBMC reliability when the transmission is attacked by SMTJ or RFHJ.
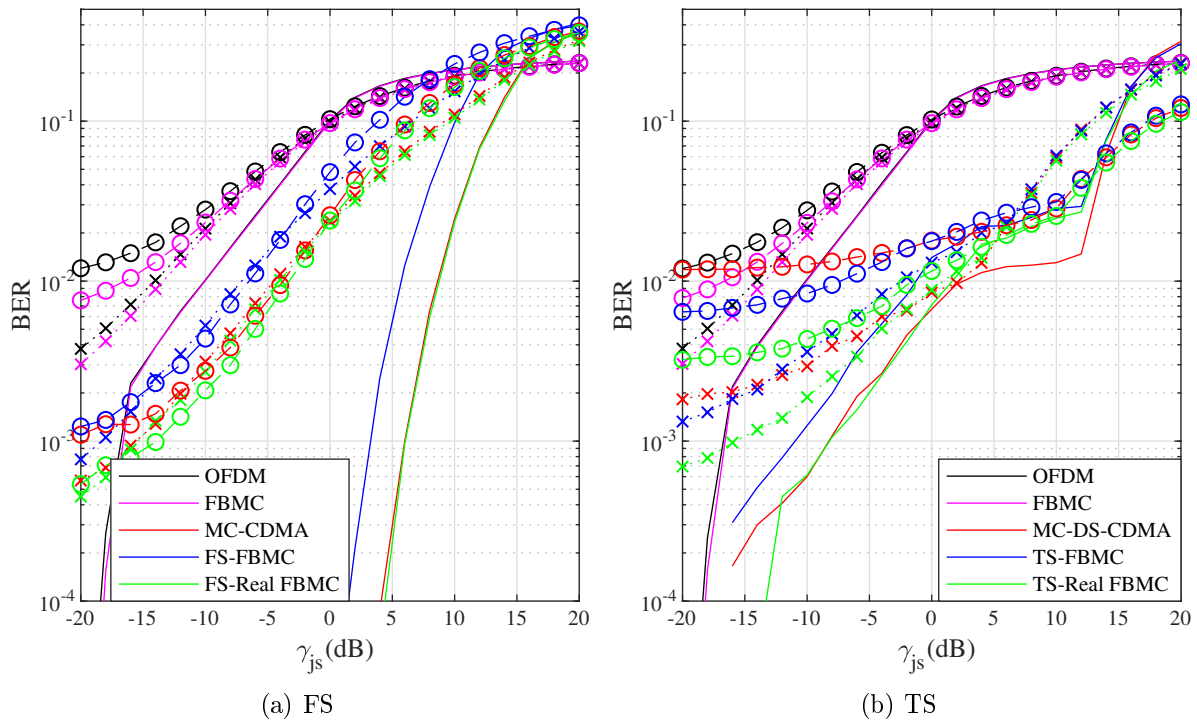
(a) FS

(b) TS
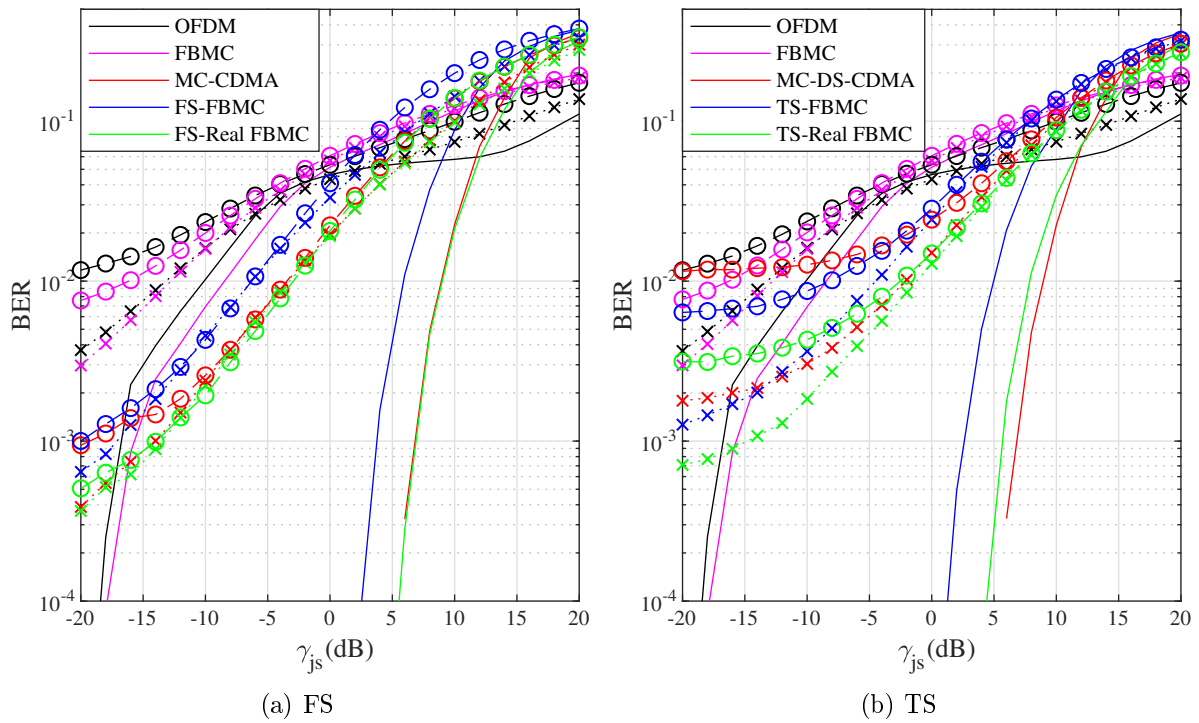
Figure 4.16: Uplink BER for worst case SMTJ without channel effect (no marker), LOS (×), and NLOS (○) as a function of the jammer-to-signal power ratio γ_{js}
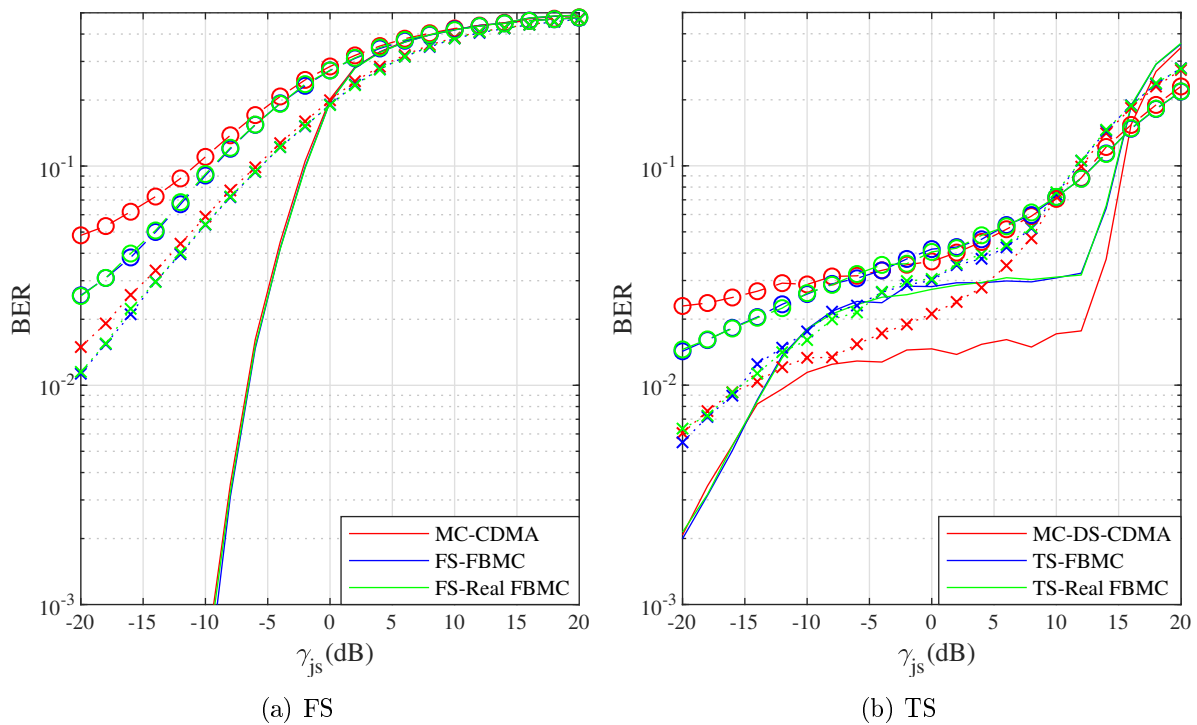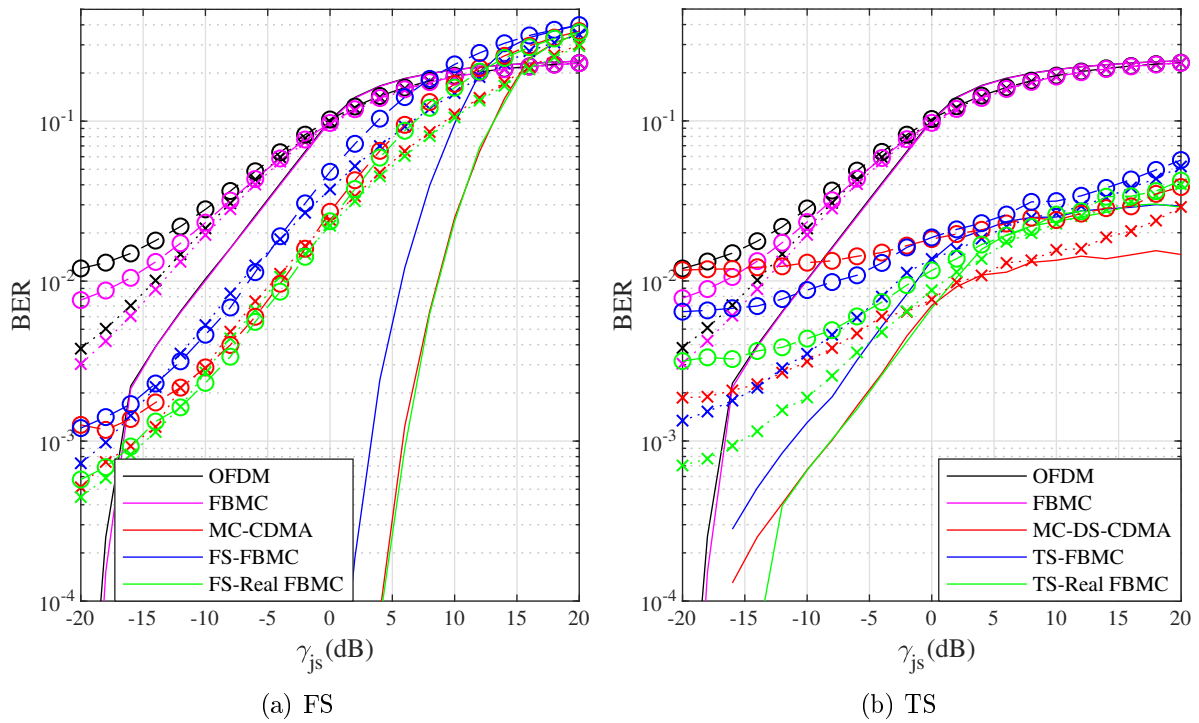

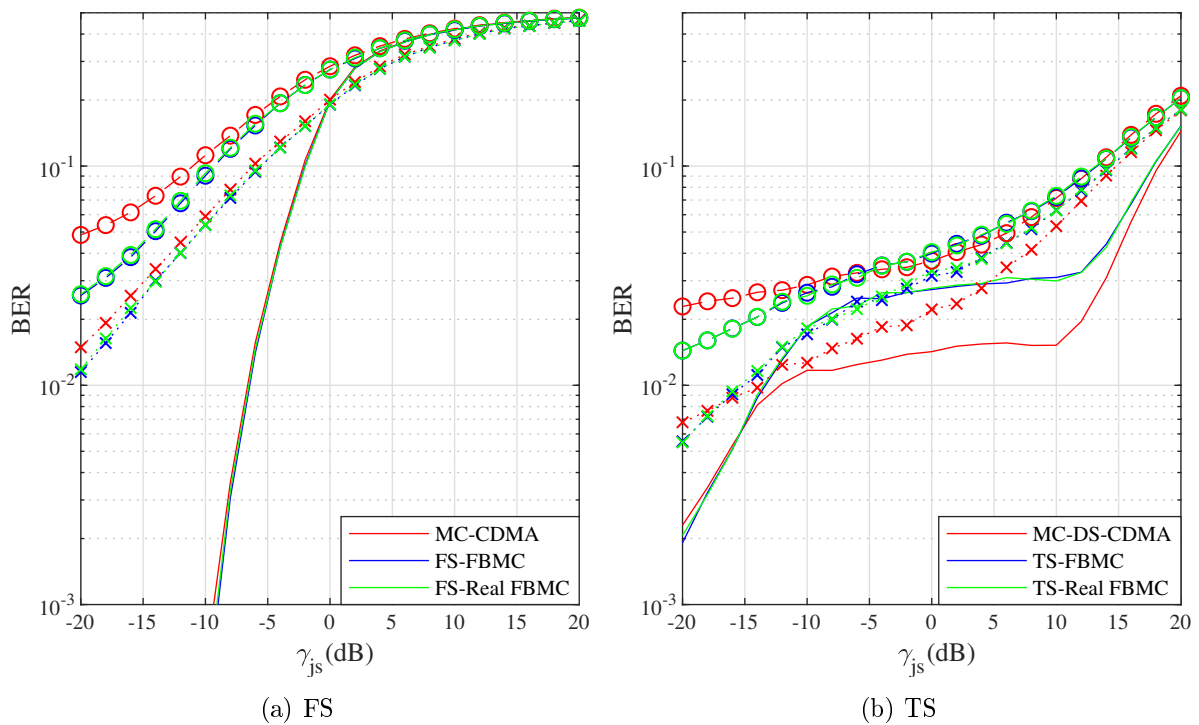
(a) FS

(b) TS
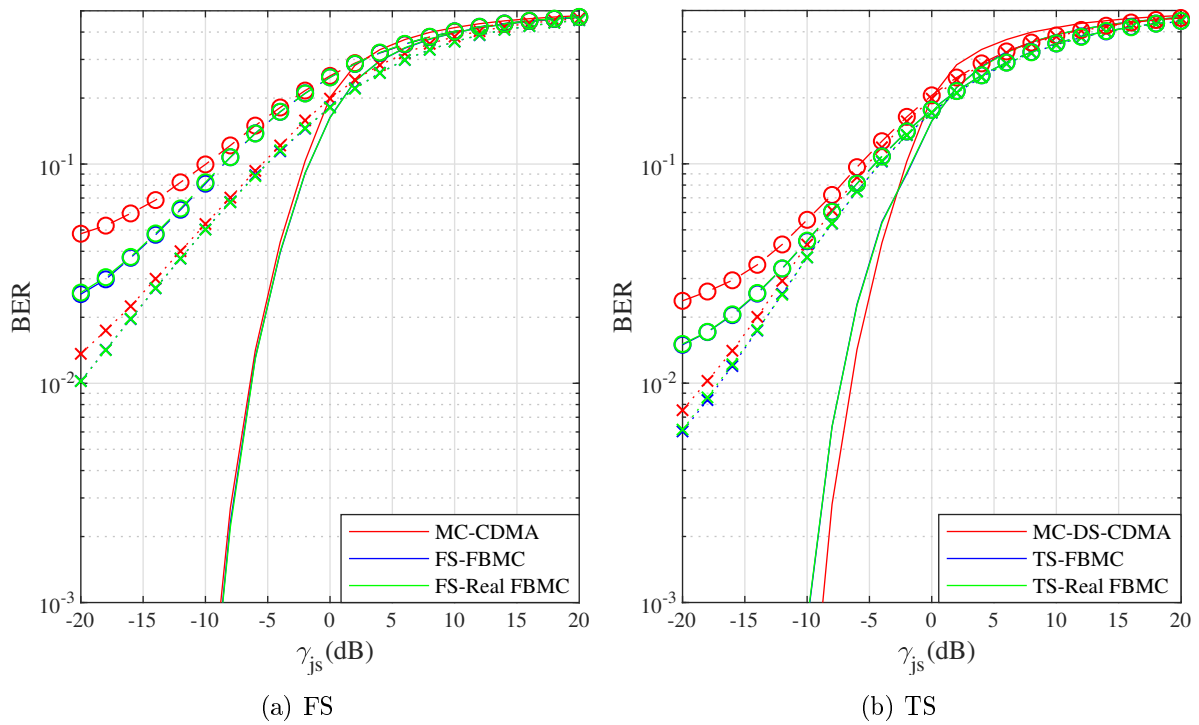
Figure 4.17: Downlink BER for worst case SMTJ without channel effect (no marker), LOS (×), and NLOS (○) as a function of the jammer-to-signal power ratio γ_{js}

(a) FS

(b) TS
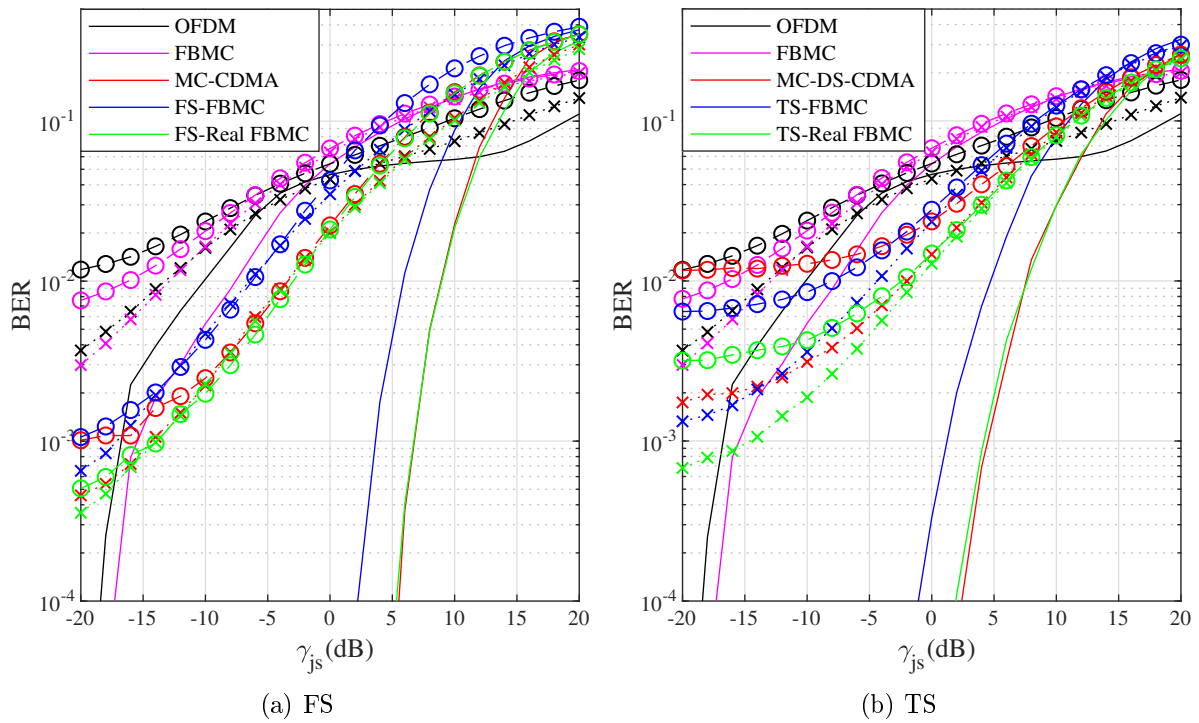
Figure 4.18: Uplink BER for worst case RFHJ without channel effect (no marker), LOS (×), and NLOS (○) as a function of the jammer-to-signal power ratio γ_{js}

(a) FS

(b) TS
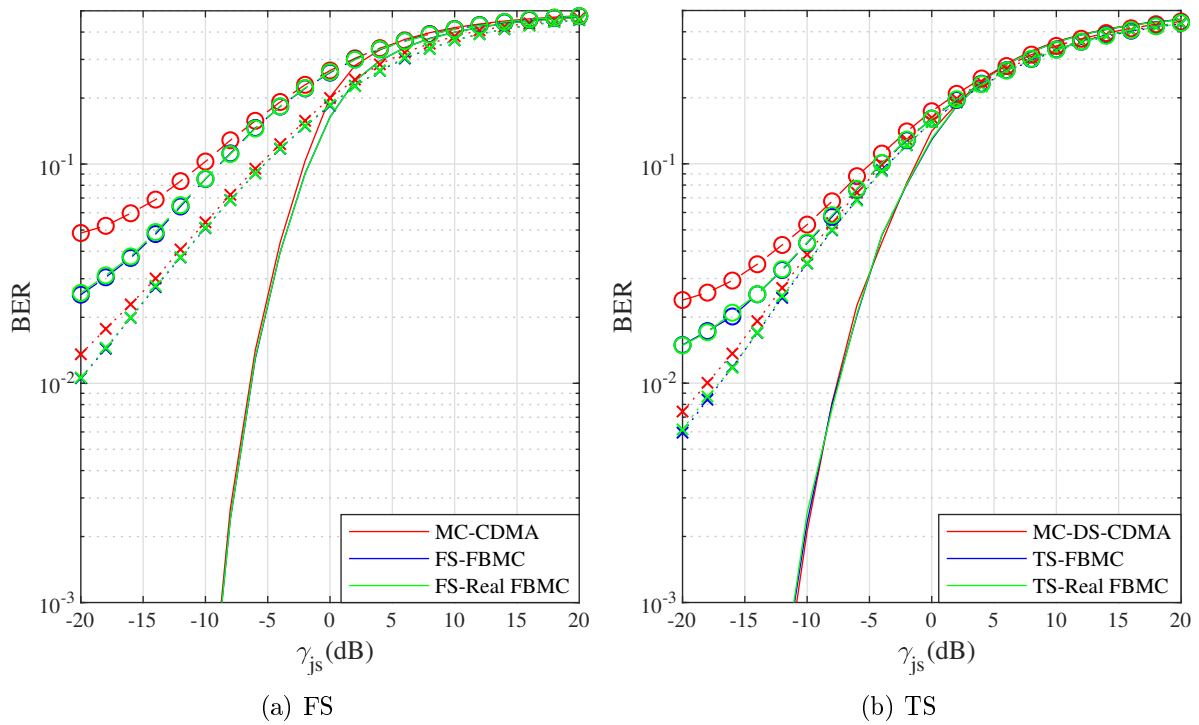
Figure 4.19: Downlink BER for worst case RFHJ for without channel effect (no marker), LOS (×), and NLOS (○) as a function of jammer-to-signal power ratio γ_{js}

As the previuos analysis was done under the assumption of perfect frequency alignment between the system subcarriers and the jamming tones, it is also demonstrated that spreading can enhance the reliability of the transmission chain when it is attacked by an off-tone jamming signal as shown in [25]. The CFO between the system subcarriers and the jammer tones is considered to be fixed for all tones. The comparison is done between FBMC and OFDM uplink variants under a fixed JSR of 5 dB. For spread FBMC, only real spreading is considered since complex spreading in the uplink has a higher BER than other spreading schemes.

Figure 4.20 shows the BER when the transmission chain is targeted by SMTJ with CFO. The results without spreading show that OFDM is more reliable under narrowband jamming with a low (or close to an integer) CFO. As the jamming bandwidth increases, OFDM outperforms FBMC even that FBMC is less sensitive to CFO than OFDM. When FS is applied, as shown in Figure 4.20(a), FS-FBMC outperforms MC-CDMA unless a narrowband SMTJ is applied with a low (or close to an integer) CFO. It can also be seen that MC-CDMA is less sensitive to CFO than OFDM. The sensitivity for CFO also decreases for OFDM when TS is applied as shown in Figure 4.20(b). Moreover, it is proven that TS-FBMC outperforms MC-DS-CDMA under SMTJ. The BER remains almost constant for the tested JSR levels except a slight increase in the case of TS-FBMC. The performance under the influence of RFHJ with CFO is shown in Figure 4.21 where the same simulation parameters of SMTJ are used. It is shown that OFDM outper-forms FBMC unless the CFO is relatively high ($\Delta n_j \to 0.5$). It is also shown, as the jamming bandwidth increases, that the performance without spreading under RFHJ is worse than the performance under SMTJ. This also holds when FS is applied as shown in Figure 4.21(a). Similar to the performance under SMTJ, FS-FBMC outperforms MC-CDMA unless the CFO is relatively low for narrow band jamming. By the application of spreading, the reliability of both FBMC and OFDM improves significantly as the num-ber of jammed subcarriers increases. Moreover, the sensitivity to the CFO variation is reduced through spreading. In Figure 4.21(b), it is shown that TS-FBMC outperforms MC-DS-CDMA in terms of BER. Both TS schemes are almost not sensitive to the change in the number of jammed subcarriers and the CFO.

As discussed previously for both types of spreading, it is proven that for time-variant jamming with CFO, spreading becomes more beneficial as the number of jammed resource blocks increases. Moreover, as mentioned in [25], it is proven that the advantage of the perfect time localization for MC-DS-CDMA has a limited effect under time-variant jamming with CFO.

(a) FS

(b) TS
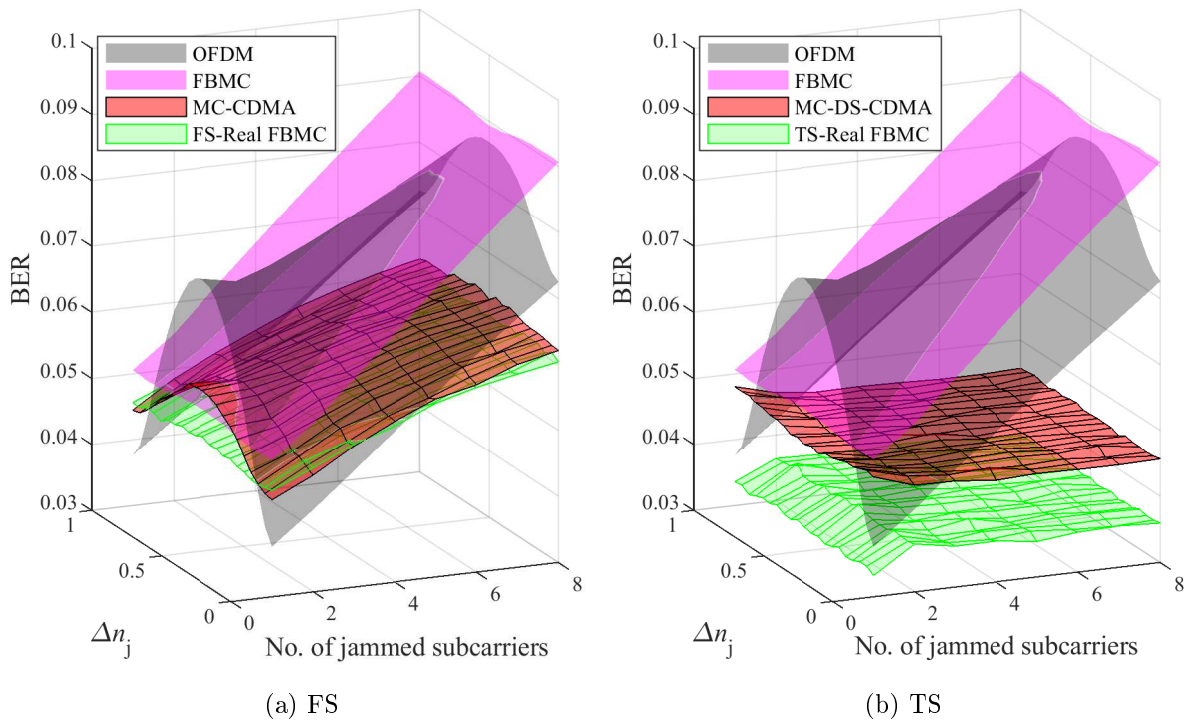
Figure 4.20: Uplink BER for SMTJ as a function of the number of jammed subcarriers and the normalized CFO Δn_{j} using NLOS channel, $\gamma_{\mathrm{js}} = 5\mathrm{dB}$

(a) FS

(b) TS
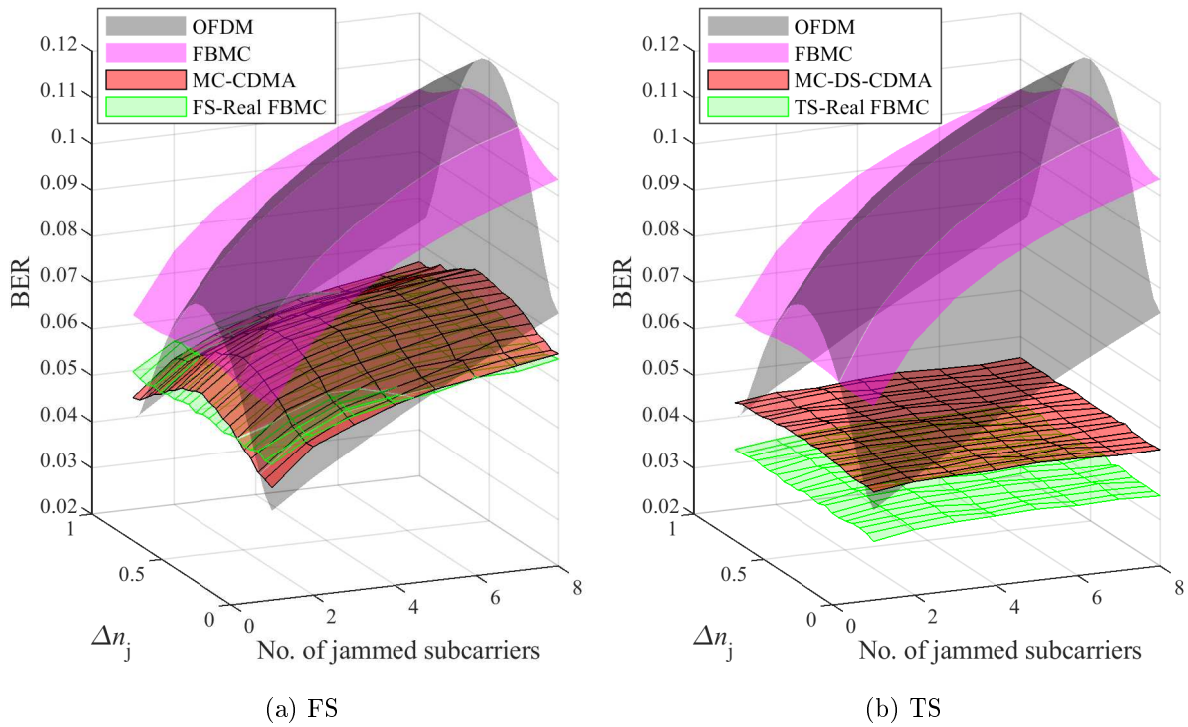
Figure 4.21: Uplink BER for RFHJ as a function of the number of jammed subcarriers and the normalized CFO Δn_{j} using NLOS channel, $\gamma_{\mathrm{js}} = 5\mathrm{dB}$

4.5   Summary

The reliability of spread FBMC was tested under several types of jammers in this chapter. At the beginning, a short description about the applied model was given. This included the method used for the maximization of the ADC performance and the simulation parameters. This was followed by the discussion of the noise jamming techniques. The performance in the chosen industrial propagation channels shows that real spread FBMC usually outperforms spread OFDM variants under the influence of BNJ and PBJ.

The chapter then continues with the performance analysis under tone jamming. When continuous tone jamming was applied to attack the simulated transmission, real FS-FBMC outperforms MC-CDMA under the effect of ATJ, MTJ, and RMTJ. However, MC-DS-CDMA usually outperforms real TS-FBMC as the JSR increases due to the perfect time localization of the OFDM transmission.

Later on, SMTJ and RFHJ were applied as time-variant tone jamming methods to interfere the spread FBMC transmission. In this case, the maximum number of jammed subcarriers was set to 25% of the total number of subcarriers. Due to the limited number of attacked resource blocks, spreading is less significant in the enhancement of the reliability of the system. Real spread FBMC was the most reliable scheme under the effect of the industrial propagation channels.

Finally, the effects of SMTJ and RFHJ with a CFO between the subcarriers of the system and the jamming tones were investigated. For a fixed JSR of 5 dB, it was proven that spreading becomes more effective in the robustness of the system as the number of jamming tones increases. Furthermore, it was shown that real FS-FBMC outperforms MC-CDMA unless both schemes are attacked by a narrow band jamming signal with a low CFO. Moreover, the performance of real TS-FBMC was slightly better than MC-DS-CDMA for the tested simulation parameters.

Chapter 5

Practical Implementation using USRP Radios

This chapter describes the practical implementation of the spread FBMC transmission chain under jamming using USRP radios. As proposed in [146], a frequency domain based approach is used for time synchronization and frequency offset estimation at the receiver. The chapter starts with a description of the implemented model followed by the lab setup and some implementation issues. A comparison between theoretical and practical results is described afterwards to show the effect of spreading in the enhancement of the reliability of FBMC. The work done in this chapter was published in [44].

5.1   USRP Overview

The implementation of SDRs allows the modification of several parameters without the replacement of any components. One of the most common low-cost SDRs in the field of research is the USRP. As described in [44], the USRP is made of a motherboard containing a Field Programmable Gate Array (FPGA) to run the mathematical and logical operations. The motherboard also contains the ADC and the DAC chips. Moreover, the RF front end operations are performed by the daughterboard.

Figure 5.1 shows a simplified structure for a USRP-2922 [147], which is used in this work, as an example. It mainly consists of an N200 motherboard [148] with an SBX daughterboard [149] so that the device can operate in the frequency range between 400 MHz and 4.4 GHz. On the transmitter side, the generated digital data from the FPGA are converted by the 16-bit DAC (AD9777). The high resolution of the DAC is important to transmit MC signals which have a high PAPR as discussed in chapter 2.

Following the DAC conversion, the analog signal, which is split into real and imaginary components, is sent to the daugterboard as an input of the In-phase/Quadrature (I/Q) modulator (ADL5375). In the I/Q modulator, the signal is upconverted by the carrier frequency which is controlled by the user interface. The I/Q signal is then amplified through a controllable power amplification stage which is also controlled by the user interface. The amplification level is controlled by an attenuator (HMC624LP4) which allows a dynamic range of 31.5 dB with a gain step of 0.5 dB [150]. The amplified signal is low-pass filtered before it is sent through the channel. The transmitter output connector can also be used as a receiver input since the two paths are connected by an RF switch (AS225). The other RF input connector is dedicated for the reception path only. The assignment of the RF ports is done by the LabView user interface.

The receiver front end in the SBX daugterboard starts with a controllable amplification stage using the HMC624LP4 digital attenuator. The amplified signal is used as an input to the I/Q demodulator (ADL5380) where the frequency downconversion is also done. The two branches of the demodulated signal are fed to an ADC driver (ADA4927). The purpose of the ADC driver is to provide an acceptable input level to the 14-bit ADC (ADS62P44) which is placed on the motherboard of the USRP. This is to ensure the utilization of the dynamic range of the ADC by maximizing the ENOB to avoid quantization errors. The high ADC resolution and the perfect utilization of the ADC dynamic range are essential to increase the maximum achievable SQNR. In this case, the BER caused by the quantization error is minimized. It is also important to note that several parts are omitted from the previous description for simplicity.
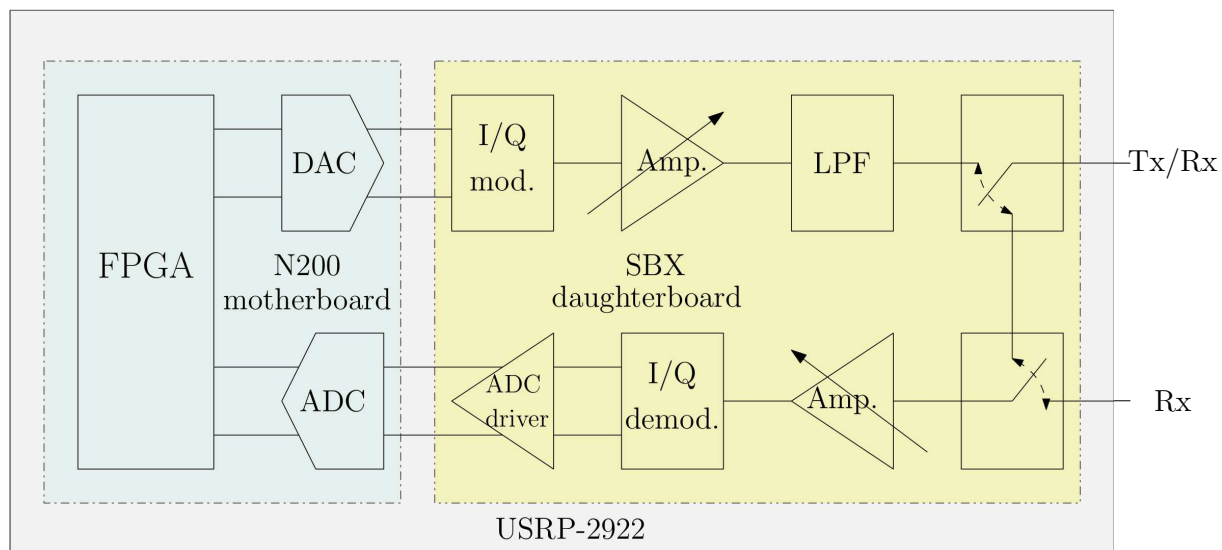
Figure 5.1: A simplified block diagram for USRP-2922 [44]

5.2   Applied System Model

The initial work for the applied system model using the pilot-aided synchronization and channel estimation based on frequency domain analysis was introduced in [146]. The main motivation behind this approach was to develop a method which is more suitable to operate than the time domain analysis in shared spectrum environmments. This is because these environments require a highly flexible resource allocation. The dissertation [151] also included a practical implementation using USRP radios to verify the performance of this approach.

In general, it was proven in [151] that this approach achieves a similar performance to the time domain synchronization at a lower computational cost when both are tested under shared spectrum scenarios. However, this approach has some drawbacks such as the possible need of an additional synchronization stage and the limited performance under relatively high offsets. This work was extended in [152] to allow a 2×2 MIMO operation. Spread FBMC practical implementation of the above mentioned method was done in [153].

The transmitter of the practical system, shown in Figure 5.2 for the downlink, is similar to the default transmitter discussed in section 2.4. However, a synchronization block is added to the payload so that it starts at sample k_{sync} as shown in Figure 5.3. It can also be attached as a preamble before the data transmission so that $k_{\text{sync}} = 0$. The synchronization block $a_{\text{sync},n,k}$, which is assumed to occupy the full system bandwidth, is given by [146]:

$$a_{\text{sync},n,k} = \begin{cases} s_{\text{p},n}, & k = k_{\text{sync}} \\ -s_{\text{p},n}, & k = k_{\text{sync}} + 2 \\ 0, & \text{Otherwise} , \end{cases} \tag{5.1}$$

where $s_{\text{p},n}$ is an arbitrary known sequence. Moreover, zero-amplitude guard symbols are used to reduce the interference between pilots for $k = k_{\text{sync}} + 1$ and the interference between the synchronization block and the payload for $k = k_{\text{sync}} + 3$. Therefore, in this case where 2 pilot symbols and 2 guard symbols are attached, the frame duration is extended to $K' = K + 4$. Each synchronization block contains a certain number of pilot symbols which are divided equally on both utilized samples. For any even subcarrier $n_{\text{e}} \in N_{\text{e}}$, the two pilot resource blocks $P_{\text{T},n_{\text{e}},1}$ and $P_{\text{T},n_{\text{e}},2}$ are given by [146]:

$$\begin{aligned} P_{\text{T},n_{\text{e}},1} &= a_{\text{sync},n_{\text{e}},k_{\text{sync}}} = s_{\text{p},n_{\text{e}},k_{\text{sync}}} , \\ P_{\text{T},n_{\text{e}},2} &= a_{\text{sync},n_{\text{e}},k_{\text{sync}}+2} = -s_{\text{p},n_{\text{e}},k_{\text{sync}}+2} . \end{aligned} \tag{5.2}$$
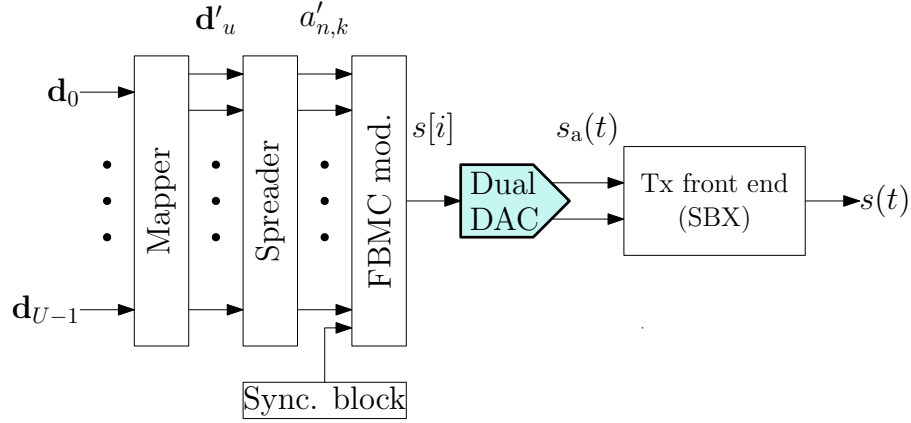
Figure 5.2: Spread FBMC transmitter with added pilots [44]

More pilot and guard symbols can be added if more accurate synchronization and channel estimation are needed such as in MIMO-FBMC shown in [152]. The modified data $a'_{n,k}$, consisting of the payload and the synchronization block are FBMC modulated. Afterwards, the modulated data are converted by the DAC and transmitted through the system channel by the RF front end.

At the receiver shown in Figure 5.4, the output of the ADC is processed by the frequency domain analysis block explained in [146]. In this block, both CFO and TO are measured and corrected using a pilot-based estimation. The CTF is also estimated and passed to the equalizer after the analysis block to compensate the channel effect.

As described in [146], the synchronization is done as shown in the same analysis block where the start of the frame $\hat{k}$ is detected at the maximum of the normalized auto-correlation function in the frequency domain by [146]:

$$\hat{k} = \underset{k}{\operatorname{argmax}} \left\{ \frac{\left| \sum_{n_e \in N_e} \left(-r_{n_e,k} r^*_{n_e,k+2} \right) \right|}{\frac{1}{2} \sum_{n_e \in N_e} \left(|r_{n_e,k}|^2 + |r_{n_e,k+2}|^2 \right)} \right\} > \Gamma, \tag{5.3}$$

where $0 < \Gamma < 1$ is a given threshold. Afterwards, the received pilots $P'_{n_e,1}$ and $P'_{n_e,2}$ are extracted. The normalized weights of the extracted pilots w_{p,n_e} at the even subcarriers are proportoinal to the energy of the extracted pilot symbols as [146]:

$$w_{p,n_e} = \frac{|P'_{n_e,1}|^2 + |P'_{n_e,2}|^2}{\sum_{n'_e \in N_e} \left(|P'_{n'_e,1}|^2 + |P'_{n'_e,2}|^2 \right)} . \tag{5.4}$$

Then, the normalized weights of the pilots are used to estimate the CFO $\hat{\Delta} n'_s$ as [146]:

$$\hat{\Delta} n'_s = \frac{1}{2\pi} \angle \left[\sum_{n_e \in N_e} w_{p,n_e} \frac{-P'_{n_e,2}}{P'_{n_e,1}} \right], \tag{5.5}$$
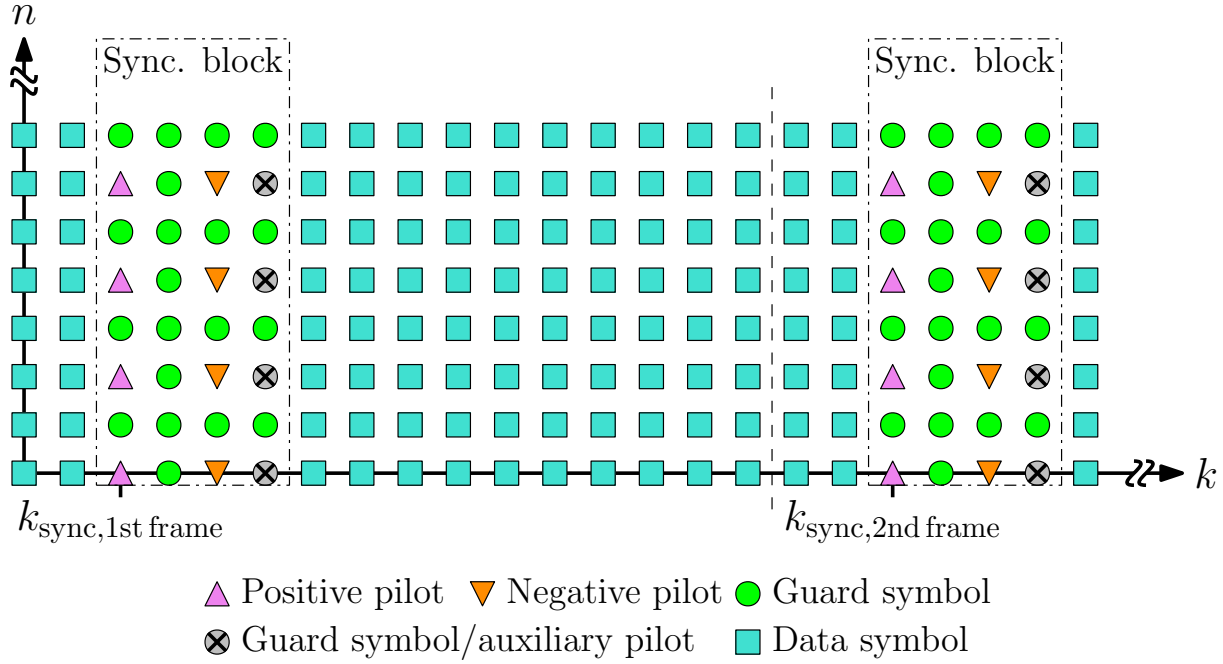
Figure 5.3: The frame structure of the applied synchronization and frequency estimation for $N = 8$, $K = 12$, $K' = 16$, and $k_{\mathrm{sync}} = 2$

where $\angle$ is the phase angle of the complex number. The estimated CFO, which is assumed to be fixed for all subcarriers, is used afterwards to correct the input of the analysis block. The received pilots are also used for the channel estimation. Assuming that the channel is time-invariant during the time between the period of pilots T_{s}, the CTF for the even subcarriers $H'_{\mathrm{s},n_{\mathrm{e}}}$ is given by [146]:

$$ H'_{\mathrm{s},n_{\mathrm{e}}} = \frac{1}{2} \left(\frac{P'_{n_{\mathrm{e}},1}}{P_{\mathrm{T},n_{\mathrm{e}},1}} + \frac{P'_{n_{\mathrm{e}},2}}{P_{\mathrm{T},n_{\mathrm{e}},2}} \right) . \tag{5.6} $$

Furthermore, the CTF of the odd subcarriers $H'_{\mathrm{s},n_{\mathrm{o}}}$ where $n_{\mathrm{o}} \in N_{\mathrm{o}}$ can be obtained by the interpolation between the preceding even subcarrier $n_{\mathrm{o}} - 1$ and the following one $n_{\mathrm{o}} + 1$ so that [152]:

$$ H'_{\mathrm{s},n_{\mathrm{o}}} = \frac{H'_{\mathrm{s},n_{\mathrm{o}}-1} + H'_{\mathrm{s},n_{\mathrm{o}}+1}}{2} . \tag{5.7} $$

Similarly, the pilot weights of the odd subcarriers $w_{\mathrm{p},n_{\mathrm{o}}}$ are obtained. If the previous process is not sufficient to correct the CFO and the TO, a further stage based on the cross-correlation between the corrected signal and the synchronization block, which is assumed to be known, is done to correct the TO. As the fractional TO correction is limited to $N/2$, the estimated TO $\hat{\Delta}k_{\mathrm{s}}$ is obtained by an iteration loop on $\Delta k_{\mathrm{s}} \in [-N/4, -N/4 + 1, \cdots, N/4 - 1]$ as [146]:

$$ \hat{\Delta}k_{\mathrm{s}} = \underset{\Delta k_{\mathrm{s}}}{\mathrm{argmax}} \left\{ \frac{\left| \sum_{n=0}^{N-1} \sum_{\check{p} \in [0,2]} \sqrt{w_{\mathrm{p},n}} r'_{n,\hat{k}+k_{\mathrm{sync}}+\check{p}} a^*_{\mathrm{sync},n,k_{\mathrm{sync}}+\check{p}} \mathrm{e}^{\mathrm{j}2\pi\frac{n}{N}\Delta k_{\mathrm{s}}} \right|}{\frac{1}{2} \sum_{n=0}^{N-1} \sum_{\check{p} \in [0,2]} \left(|r'_{n,\hat{k}+k_{\mathrm{sync}}+\check{p}}|^2 + |a_{\mathrm{sync},n,k_{\mathrm{sync}}+\check{p}}|^2 \right)} \right\} . \tag{5.8} $$
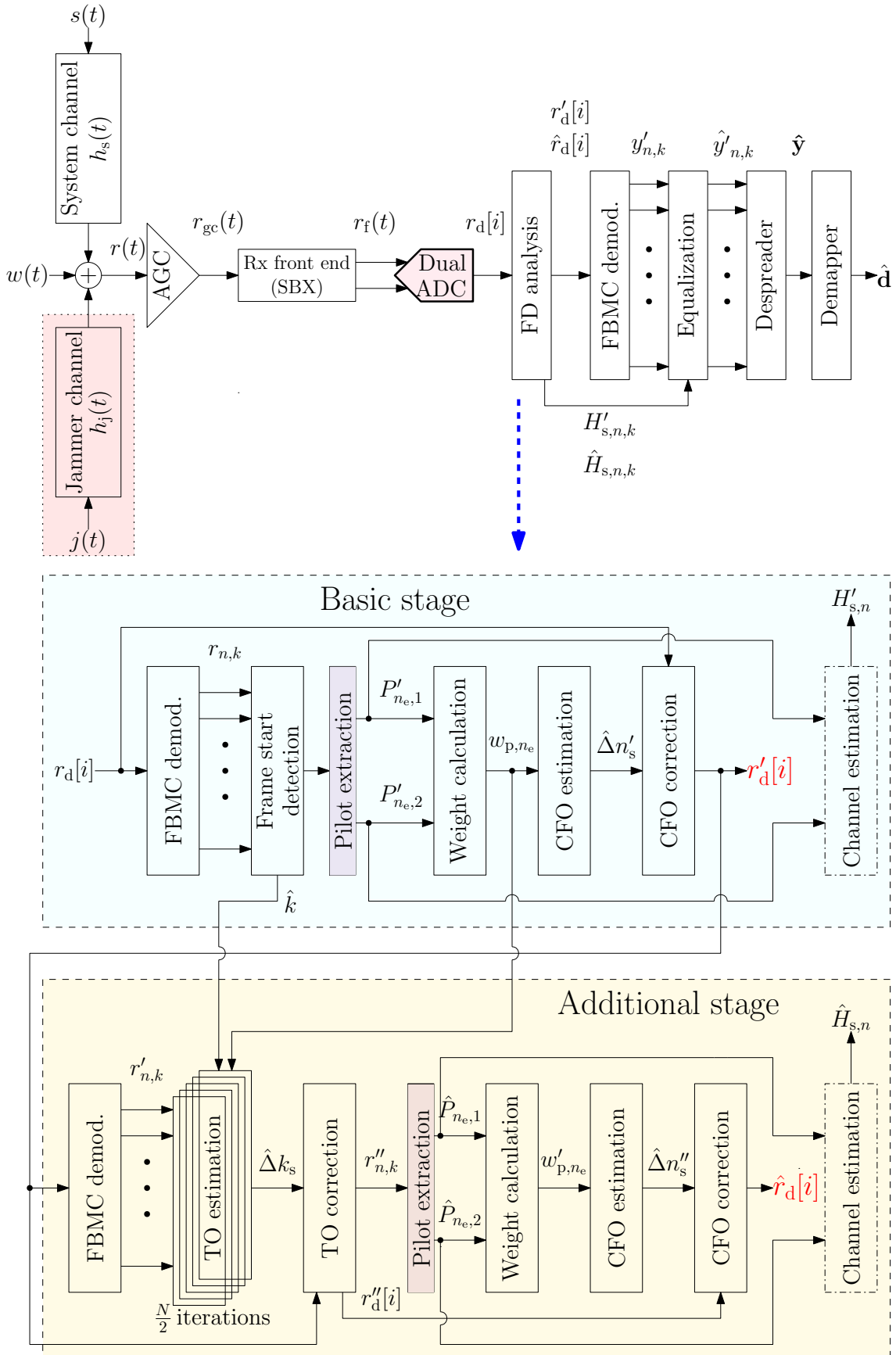
Figure 5.4: Spread FBMC receiver with a detailed frequency domain analysis block [44]

Then, the TO is used to correct the frequency-corrected signal which was obtained from the first stage. From the resultant timely-corrected signal $r''_{n,k}$, the corrected pilots $\hat{P}_{n_e,1}$ and $\hat{P}_{n_e,2}$ are used to do another stage of CFO correction as [146]:

$$\hat{\Delta} n''_s = \frac{1}{2\pi} \angle \left[\sum_{n_e \in N_e} w'_{p,n_e} \frac{-\hat{P}_{n_e,2}}{\hat{P}_{n_e,1}} \right], \tag{5.9}$$

where w'_{p,n_e} are the corrected pilot weights. The final output $\hat{r}_d[i]$ of the analysis block is corrected by the overall CFO $\hat{\Delta} n_s = \hat{\Delta} n'_s + \hat{\Delta} n''_s$. Moreover, if the additional stage is needed, a more accurate CTF estimation $\hat{H}_s$ is done by the replacement of extracted pilots in equations (5.6) and (5.7) by the corrected pilots [146].

5.3   Lab Setup

The transmission chain implementation in [153] is used to measure the robustness of spread FBMC under jamming as shown in Figure 5.5. In addition to the single user operation in uplink, the transmitter can operate as a downlink when the multiuser mode is selected.

To minimize the wireless channel effect which can cause several variations that degrade the accuracy of the lab measurements, wired connections are used between all devices. WGN is added at the receiver with a fixed power level so that the SNR remains constant [44]. Although wire connections are used, the channel estimator is still important to compensate the effects caused by the elements of the RF front ends [44].

At the receiver, a two-stage analysis block is implemented to maximize the accuracy of the synchronization and the channel estimation. As the frame start is determined by the auto-correlation function given in equation 5.3, the need for the external synchronization clock between the transmitter and the receiver can be neglected when the SNR is high. This also requires a suitable selection of the threshold Γ as discussed in [151] and [152]. As the SNR decreases, the threshold needs to be lowered. However, the miss-detection rate increases rapidly as the SNR decreases below 0 dB as proven in [152].

To have a synchronized transmission, a single window is used to transmit signals with the same sampling rate. Another solution is to rely on the Global Positioning System (GPS) clock as a reference clock when the devices have a GPS receiver. If multiple devices are operated, a clock distributor (CDA-2990) which receives an external clock signal from another source, can be implemented. Moreover, the synchronization can be achieved by the assignment of any of the devices as a reference clock generator.

An external AGC was implemented to precisely regulate the incoming signal to the receiver. Therefore, an external simple closed-loop AGC design in [154] was implemented using a Variable Gain Amplifier (VGA) ADL5330 which output feeds the input of a logarithmic amplitude detector (AD8318). Since the output voltage of the detector is related to its input signal by a negative linear-in-dB function as described in [155], the output of the detector is utilized to control the gain of the VGA. A fixed operation point for the detector is determined by the controller PC and sent to the Arduino Uno micro-controller. The micro-controller sends a serial clocked signal through the data bus to the DAC which converts it to the corresponding voltage output. The output of the DAC is used as the set voltage of the detector. The controller can also generate a clock signal that can be used as an external synchronization clock between all devices if needed. Moreover, it was proven in [156–158] that the AGC can be utilized to detect and estimate the interference. Furthermore, a step attenuator was used to control the jammer output. This achieves more flexibility to test a wider JSR range than controlling the gains of the transmitter and the receiver from the LabVIEW user interface.
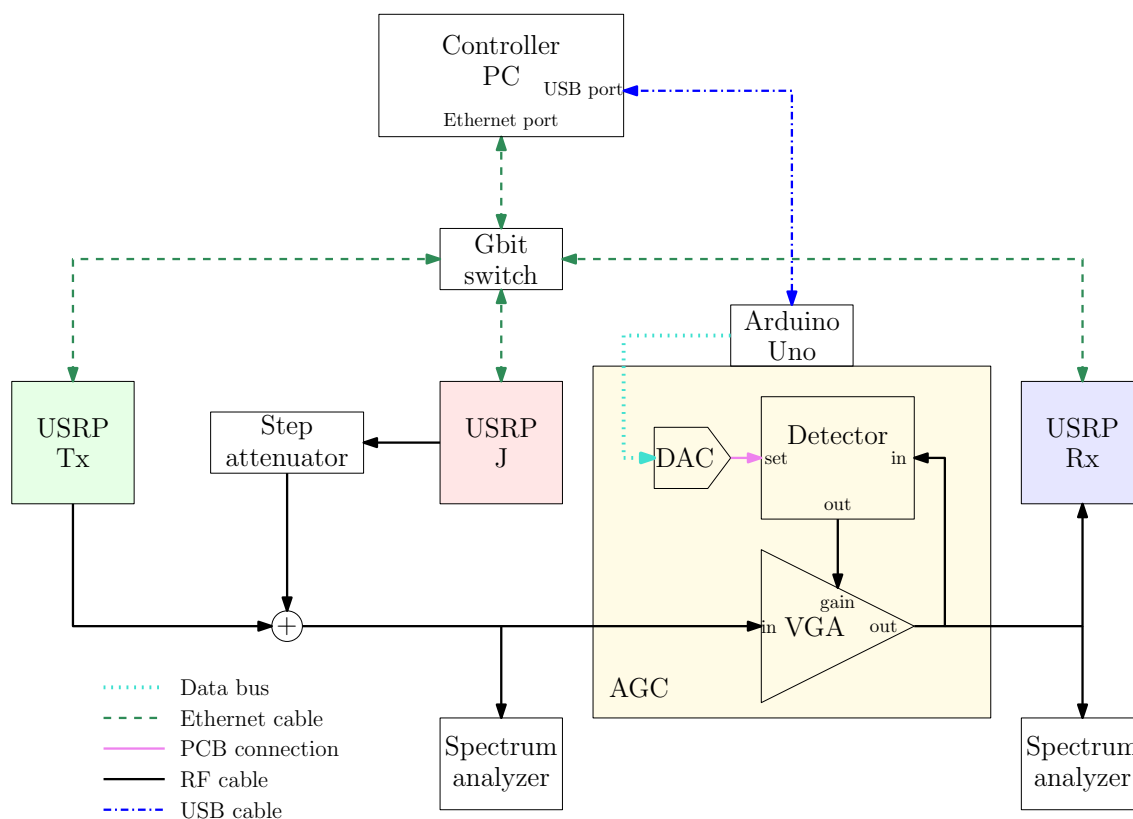
Figure 5.5: Block diagram of the lab setup, USRP Tx is the transmitter of the desired signal, USRP J is the transmitter of the jamming signal, and USRP Rx is the receiver [44]

5.4   Implementation Issues

Several previous works discussed the implementation of FBMC on USRP radios to measure its performance in practice. In [159], which was focused on the synchronization and equalization in FBMC, a transmission chain was implemented using USRP radios which were controllable by software. When the measured performance of the FBMC was compared to the theoretical performance under AWGN, it showed a slight degradation in terms of MMSE. USRP radios were also used in [160], alongside the ZynqSDR radio. This was done to validate the co-existence between FM radio broadcast channels as the primary spectrum user and an FBMC network operated by MATLAB and Simulink as the secondary user [160]. In this dissertation, several issues were found during the practical implementation of the system.

5.4.1   Unintentional Jamming

Since one of the main targets of this dissertation is to investigate the reliability of the spread FBMC transmission, which requires verification by practical measurements, a reasonable test is required to find the jamming effect on the transmitted payload. However, many jamming attacks can cause more severe distortion to the signal by targeting the applied synchronization or equalization techniques as discussed widely in [17] for conventional OFDM. Since the applied jamming signal uses a generalized form that is not designed to attack the applied transmission scheme or the selected receiver implementation, these errors are not classified as results of protocol-aware attacks. A more accurate classification is to say that it is an unintentional synchronization or equalization jamming attack.

One of the most common errors caused by the jammer is to cause a false frame start. This can be caused by a set of jamming tones that have a higher auto-correlation at the receiver than the synchronization block. This attack may also interrupt the reception of a frame that was detected correctly. A possible solution for this problem is to change the size and/or the structure of the synchronization block according to the type of the interference. However, the spectral efficiency of the transmission scheme decreases when the synchronization block size increases.

Another error that occurs frequently is the pilot jamming attack, which can be caused by a jamming signal that affects the pilot subcarriers. If the jamming is destructive, the noise floor at the pilot subcarriers is raised and in some rare cases, this can cause pilot nulling as mentioned in [44]

Furthermore, it was also seen, in case of tone jamming, that a high amount of noise is generated alongside the jamming tones. Therefore, it is important to consider that the SNR is variable for every JSR level. Another option is to assume that the SNR is fixed and the system is attacked by a combination of MTJ and BNJ.

5.4.2   Implementation of TS-FBMC

In the previous chapters, it was clear that TS-FBMC outperforms FS-FBMC for frequency selective channels and/or several jamming attacks. However, as the practical implementation is the point of concern, TS-FBMC is not an attractive variant to deploy in Ultra Reliable Low Latency Communications (URLLC) WSANs. One of the main reasons is that the receiver needs to wait for all spread data to be correctly received before despreading is done. This delay scales the transmission time by a factor of L_{c}.

Moreover, as discussed in [44] the long transmission time may be harshly affected by a number of common errors such as missed detections at the receiver. In this case, the spread data cannot be despread correctly by the same spreading code applied at the transmitter especially when the used code phase varies rapidly [44]. Although the spreading may be sufficient to correct a limited number of missed detections in some cases, the error remains present for the next spread blocks unless a new frame start is detected.

5.4.3   AGC Limitations

Several limitations were observed for the implemented simple AGC loop which was shown previously in Figure 5.5. However, the information obtained by the channel estimator alongside the expected signal power may be also useful to recalculate the set voltage which results in an adaptive AGC operation. In this case, the AGC performance depends on the transition speed between different set levels. Since a fast AGC operation needs to reduce the output capacitance which controls the low-pass cutoff frequency, the bandwidth of the AGC is negatively affected [44]. Therefore, short duration pulsed jamming is usually applied to attack the AGC operation at the receiver.

Since wideband transmission is used, an additional power amplifier may be added to the AGC input to ensure an acceptable input power. Instead of the implemented simple AGC loop, more complex AGC schemes which are discussed widely in [161] can improve the AGC operation significantly. In the latest USRP models, the built-in AGC can also be utilized.

5.5   Results and Analysis

To measure the effect of spreading as done in [44], the lab measurements were done for FBMC and FS-FBMC under MTJ where the jamming tones were equally spaced in frequency domain. To allow a correct channel estimation, only odd subcarriers were targeted by the jamming signal. The parameters shown in Table 5.1, were applied:

Number of subcarriers	512	Symbols per frame	50
Modulation type	QPSK	Spreading code	32 bit W-H
Data subcarriers	510	Internal guard subcarriers	2
Carrier frequency	1.9 GHz	Sampling frequency	512 kHz
Filter type	PHYDYAS	Overlapping factor	4
Number of pilot symbols	2	ADC resolution	14 bit (fixed)
SNR	20dB	Jamming tones	32

Table 5.1: Practical implementation parameters for spread FBMC under jamming [44]

Figure 5.6 shows the enhancement in the reliability of FBMC transmission after FS was applied. The measurement results for both FBMC and real FS-FBMC show a slight difference to the simulation results as the JSR increases. This is due to the lower detection rate of the frame start even though the threshold level was lowered. The simulations were based on a combination of MTJ and BNJ to consider the effects of the signal generated by the jammer. At BER= 0.1, the measured spreading gain is approximately 10dB compared to a gain of 12dB obtained by simulation. While the JSR varies, the input power P_{in} of the receiver was fixed to -40 dBm.

Moreover, it was proven that spreading can help to overcome some of the problems caused by the RF section as seen in Figure 5.7. The measurements were done for a fixed JSR=4dB and a variable input power level at the receiver. In this case, the Error Vector Magnitude (EVM) of the I/Q demodulator increases as the input power decreases. As mentioned in [162], the EVM increases rapidly when the received signal is extremely high due to the non-linear distortion, or if the received signal is extremely low where the noise becomes the dominant part of the received signal. Through the application of FS, it is shown that the receiver can operate with a lower input power level than unspread FBMC.
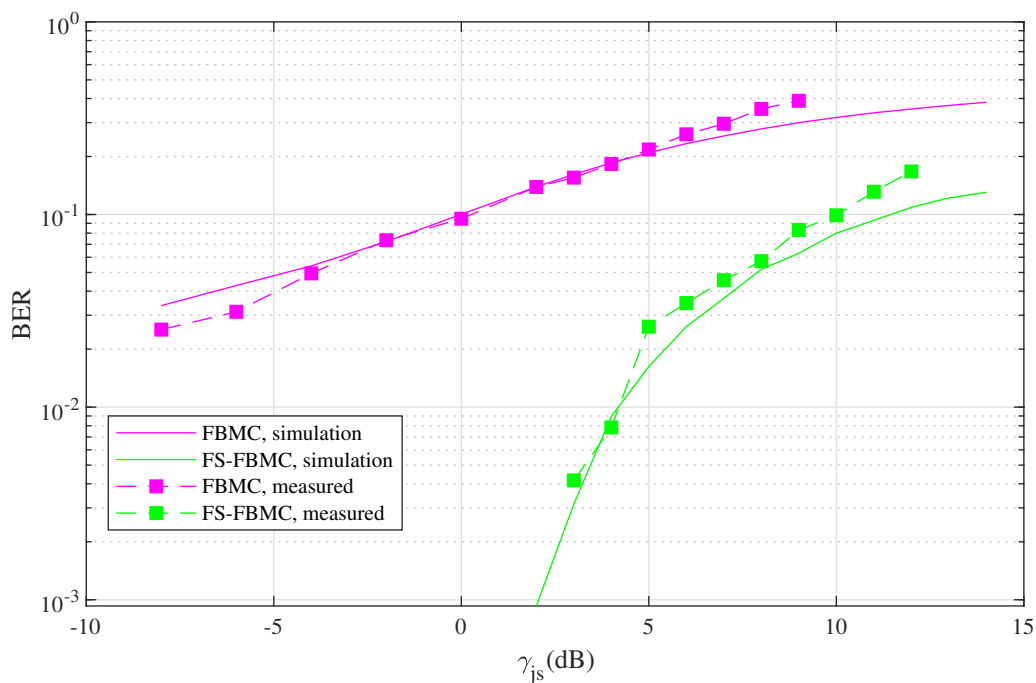
Figure 5.6: BER for FBMC and real FS-FBMC as a function of the jammer-to-signal power ratio γ_{js}, $P_{in} = -40$dBm [44]
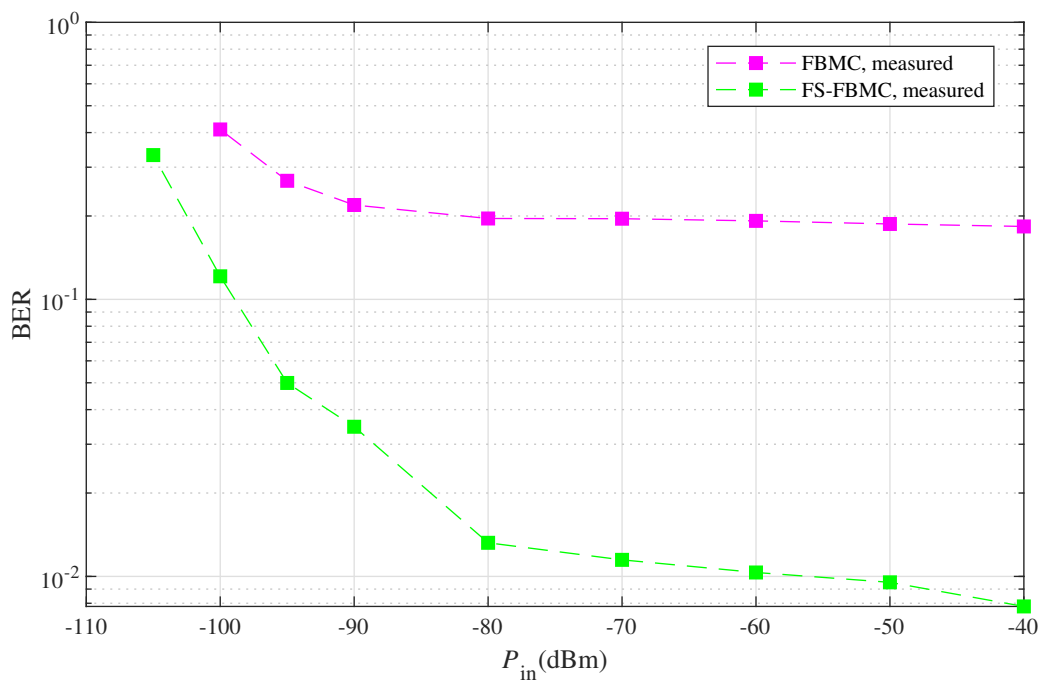
Figure 5.7: Measured BER for FBMC and real FS-FBMC for different receiver input power P_{in} levels, $\gamma_{js} = 4$dB [44]

5.6   Summary

In this chapter, the practical implementation of FS-FBMC using USRP devices was discussed. The chapter started with a short outline of the USRP device which was used in the implementation. This was followed by an explanation of the frequency domain approach shown in [146] which was utilized for the synchronization and the channel estimation.

After the lab setup was explained, some issues that affect the practical implementation using USRP radios, which involves the transmission chain and the jammer, were discussed. For TS-FBMC, although the theoretical results show it may outperforms FS, it was discussed how the problem of missed detections can degrade the operation significantly. Moreover, several limitations caused by the AGC were mentioned.

When the practical experiments were done by a fixed moderate input power and a variable JSR, the results verify the simulations results and show that the reliability of FBMC is enhanced by spreading. Moreover, it was shown that the performance of FBMC transmission degraded as the input power decreases due to the high EVM of the I/Q demodulator. By the application of FS, it was possible to operate with a lower input power level.

Chapter 6

Conclusion & Future Work

This dissertation shows that spread FBMC is a promising technique which can be deployed in reliable WSANs. Several conclusions were drawn from the aspects that were covered theoretically and practically in the previous chapters while many other issues remain open for future research to enhance this work.

6.1 Conclusions

Chapter 2 started with a description of MC transmission as a solution to overcome the frequency selectivity of the transmission channel. This was followed by an explanation of OFDM as a special case of MC modulation that uses DFT/IDFT to simplify the implementation. As OFDM suffers from several drawbacks such as the high OOB emissions and the need for the CP that reduces the spectral efficiency, FBMC was introduced. To enhance the reliability of FBMC, spreading was additionally implemented. The performance of spread FBMC variants with and without the effects of the industrial propagation channels shows a significant improvement in terms of BER. However, spread FBMC has a higher PAPR than spread OFDM when the same spreading type is applied.

In chapter 3, the ADC quantization and clipping effects on spread FBMC were discussed. It was proven that these effects cause high BER in two cases. First, when the input power is large so that the received signal is clipped frequently. The second case is when the input power is low, causing the reduction of the utilized quantization levels. Thus, creating a low ENOB. It was also shown that the significance of the clipping level selection increases as the ADC resolution decreases. Moreover, it was also proven that spread FBMC usually outperforms spread OFDM variants in terms of BER even when OFDM variants can reach a higher maximum SQNRs at lower optimal CFs due to the lower PAPR.

The jamming effects on spread FBMC were discussed in chapter 4. Based on the results of the previous chapter, the ADC was adapted to reduce the quantization error with a reasonable computational cost. Several types of jamming were implemented to test the robustness of the transmission. This includes BNJ and PBJ as noise jamming techniques as well as several tone jamming methods which are ATJ, MTJ, RMTJ, SMTJ, and RFHJ. It was shown that spreading increases the reliability of FBMC transmission under the influence of jamming. However, spreading was less effective as time-variant jamming with a limited number of resource blocks was applied to attack the transmission. In most cases under the simulated industrial propagation channels, real spread FBMC outperforms spread OFDM variants.

The practical implementation of spread FBMC under jamming using USRP radios, which was discussed in chapter 5, shows that a significant enhancement in the robustness of the FBMC transmission can be achieved by spreading. Several implementation issues which can affect the practical measurements were explained. Moreover, it was proven that spreading can also be a useful technique to overcome the errors caused by the RF front end elements.

6.2   Future Work

Some future aspects that can enhance the work done in this dissertation are organized as the topics of the previous chapters. In the area of spread FBMC, which was discussed widely in chapter 2, the following research subjects can be suggested:

- advanced despreading techniques such as weighted or adaptive despreading,

- adaptive bit loading on spread FBMC,

- optimal W-H code selection on the OQAM pre-processor,

- co-existence of spread FBMC wireless networks,

- effects of PAPR reduction methods on spread FBMC systems.

With a focus on the quantization and clipping effects on spread FBMC transmission, some ideas to enhance the work done in chapter 3 are as follows:

- peak restoration of clipped signal periods in a spread FBMC receiver,

- utilization of clipped symbols as an indication for the presence of high-power jamming signals,

- spread FBMC operation with single-bit or low-resolution ADCs,

- investigation of the transmitter IFFT/DAC resolutions effects on spread FBMC,

- ADC errors and their drawbacks on the performance of spread FBMC such as non-linearity, sampling errors, missing codes, etc.

As Chapter 4 focused on the jamming effects on the spread FBMC networks, several issues are still open for more investigation which are:

- pulsed jamming effects on spread FBMC,

- optimal resource allocation to avoid jammed subcarriers,

- enhance the spread FBMC performance under jamming by coding and interleaving,

- protocol-aware jamming attacks on spread FBMC,

- jamming effects on DFT-spread FBMC.

In chapter 5, the practical implementation of spread FBMC using USRP radios, by the application of a pilot-aided synchronization and channel estimation, can be also expanded in many ways such as:

- implementation of various detection/estimation methods in time or frequency domains,

- application of different pilot structures,

- evaluation of spread FBMC reliability in various realistic environments,

- expand the practical system to support MIMO transmission,

- implementation of time-variant jamming techniques,

- utilization of the estimated channel parameters in the AGC loop,

- evaluation of the internal AGC performance under jamming.

Bibliography

[1] I. F. Akyildiz and I. H. Kasimoglu, "Wireless sensor and actor networks: research challanges," in *Ad Hoc Networks 2*, pp. 351–367, 2004.

[2] C. Shahriar, "Resilient waveform design for OFDM-MIMO communication systems," Ph.D. dissertation, Virginia Polytechnic Institute and State University, Arlington, VA, USA, Sep. 2015.

[3] K. Fazel, "Performance of CDMA/OFDM for mobile communication system," in *Proc. IEEE Int. Conf. Universal Pers. Commun.*, Ottawa, Canada, Oct. 1993, pp. 975–979.

[4] C. Lélé, P. Siohan, R. Legouable, and M. Bellanger, "OFDM/OQAM for spread spectrum transmission," in *Proc. 6th Int. Workshop Multi-Carrier Spread Spectrum (MC-SS)*, Herrsching, Germany, May 2007, pp. 157–166.

[5] C. Lélé, P. Siohan, R. Legouable, and M. Bellanger, "CDMA transmission with complex OQAM/OFDM," in *EURASIP J. Wireless Commun. and Netw.*, vol. 2008, Article ID: 748063, 2008.

[6] C. Lélé, P. Siohan, and R. Legouable, "The Alamouti scheme with CDMA-OFDM/OQAM," in *EURASIP J. Wireless Commun. and Netw.*, 2010.

[7] D. Na and K. Choi, "Intrinsic ICI-free Alamouti coded FBMC," in *IEEE Commun. Lett.*, vol. 20, no. 10, pp. 1971–1974, Jul. 2016.

[8] M. Renfors, T. Ihalainen, and T. H. Stitz, "A block-Alamouti scheme for filterbank based multicarrier transmission," in *Eur. Wireless Conf. (EW)*, Lucca, Italy, Apr. 2010, pp. 1031–1037.

[9] F. Rafiee-Nia and H. Zamiri-Jafarian, "A new filterbank-based complex CDMA system for transmission in underwater acoustic channels," in *Proc. 22nd Iranian Conf. Elect. Eng.*, Tehran, Iran, May 2014, pp. 1511–1515.

[10] M. Al-Attraqchi, S. Boussakta and S. Le Goff, "An enhanced OFDM/OQAM system exploiting Walsh-Hadamard transform," in *IEEE 73rd Veh. Technol. Conf. (VTC Spring)*, Budapest, Hungary, Feb. 2011, pp. 1–5.

[11] R. Nissel, J. Blumenstein and M. Rupp, "Block frequency spreading: A method for low-complexity MIMO in FBMC-OQAM," in *IEEE 18th Int. Workshop Signal Process. Adv. in Wireless Commun. (SPAWC)*, Sapporo, Japan, Jun. 2017, pp. 1–5, doi: 10.1109/SPAWC.2017.8227812.

[12] R. Zakaria and D. Le Ruyet, "A novel filter-bank multicarrier scheme to mitigate the intrinsic interference: application to MIMO systems," in *IEEE Trans. Wireless Commun.*, vol. 11, no. 3, pp. 1112–1123, Feb. 2012.

[13] R. Zakaria and D. Le Ruyet, "Theoretical analysis of the power spectral density for FFT-FBMC signals," in *IEEE Commun. Lett.*, vol. 20, no. 9, pp. 1748–1751, Jul. 2016.

[14] R. Nissel and M. Le Ruyet, "Pruned DFT spread FBMC-OQAM: low-PAPR, low latency, high spectral efficiency," in *IEEE Trans. Commun.*, vol. 66, no. 10, pp. 4811–4825, Oct. 2018.

[15] R. A. Poisel, *Modern Communications Jamming: Principles and Techniques*, Norwood, MA, USA: Artech House, 2011.

[16] K. Grover, A. Lim, and Q. Yang, "Jamming and anti-jamming techniques in wireless networks: a survey," in *Int. J. Ad Hoc and Ubiquitous Comput.*, vol. 17, no. 4, pp. 197–215, Dec. 2014.

[17] C. Shahriar et al., "PHY-Layer resiliency in OFDM communications: a tutorial," in *IEEE Commun. Surv. and Tut.*, vol. 17, no. 1, pp. 292–314, First quarter 2015.

[18] J. Luo, J. H. Adrian, and C. Zhou, "Bit error rate analysis of jamming for OFDM systems," in *Wireless Telecommun. Symp. (WTS)*, vol. 1, Pomona, CA, USA, Apr. 2007, pp. 1–8.

[19] J. Park, D. Kim, C. Kang, and D. Hong, "Effect of partial band jamming on OFDM based WLAN in 802.11g," in *Proc. of IEEE Int. Conf. Acoust., Speech, and Signal Process. (ICASSP)*, vol. 2, Hong Kong, China, Apr. 2003, pp. 560–563.

[20] D. W. Chi and P. Das, "Effects of nonlinear amplifier and partial band jammer in OFDM with application to 802.11n WLAN," in *Proc. IEEE Mil. Commun. Conf. (MILCOM)*, Orlando, FL, USA, 2007, pp. 1–8, doi: 10.1109/MILCOM.2007.4455161.

[21] S. Chao, W. Ping, and S. Guozhong, "Performance of OFDM in the presence of multitone jamming," in *IEEE Symp. Robot. and Appl. (ISRA)*, Kuala Lumpur, Malaysia, 2012, pp. 118–121, doi: 10.1109/ISRA.2012.6219135.

[22] H. Aldoseri, L. Häring, and A. Czylwik, "A reliable industrial wireless sensor and actor network based on CDMA-OQAM-OFDM," in *IEEE 31st Annu. Int. Symp. Pers., Indoor, and Mobile Radio Commun. (PIMRC)*, London, United Kingdom, Aug. 2020, pp. 1714–1718.

[23] I. Harjula, J. Pinola, and J. Prokkola, "Performance of IEEE802.11 based WLAN devices under various jamming signals," in *Proc. IEEE Mil. Commun. Conf. (MILCOM)*, Baltimore, MD, USA, Nov. 2011, pp. 2129–2135.

[24] C. Shahriar, S. Sodagari, R. W. McGwier and T. C. Clancy, "Performance impact of asynchronous off-tone jamming attacks against OFDM," in *Proc. IEEE Int. Conf. Commun. (ICC)*, Budapest, Hungary, 2013, pp. 2177–2182, doi: 10.1109/ICC.2013.6654850.

[25] H. Aldoseri, L. Häring, and A. Czylwik, "On the reliability of spread FBMC systems for off-tone jamming," in *IEEE 32nd Annu. Int. Symp. Pers., Indoor, and Mobile Radio Commun. (PIMRC)*, Oulu, Finland, Sep. 2021, pp. 1329–1333.

[26] M. Lichtman et al., "A communications jamming taxomony," in *IEEE Secur. and Privacy*, vol. 14, no. 1, pp. 47–54, Jan.-Feb. 2016, doi: 10.1109/MSP.2016.13.

[27] D. L. Adamy, *EW 101: A First Course in Electronic Warfare*, Norwood, MA, USA: Artech House, 2001.

[28] M. LaPan, T. C. Clancy, and R. W. McGwier, "Jamming attacks against OFDM timing synchronization and signal aquisition," in *Proc. IEEE Mil. Commun. Conf. (MILCOM)*, Orlando, FL, USA, Oct. 2012, pp. 1–7.

[29] M. LaPan, T. C. Clancy, and R. W. McGwier, "Phase warping and differential scrambling attacks against OFDM frequency synchronization," in *Proc. IEEE Int. Conf. Acoust., Speech, and Signal Process. (ICASSP)*, Vancouver, Canada, May 2013, pp. 2886–2890.

[30] T. C. Clancy, "Efficient OFDM denial: pilot jamming and pilot nulling," in *Proc. IEEE Int. Conf. Commun. (ICC)*, Kyoto, Japan, Jun. 2011, pp. 1–5.

[31] A. L. Scott, "Effects of cyclic prefix jamming versus noise jamming in OFDM signals," M.S. thesis, Air Force Institute of Technology, Wright-Patterson Air Force Base, OH, USA, 2011.

[32] M. Lichtman, J. H. Reed, T. C. Clancy, and M. Norton, "Vulnerability of LTE to hostile interference," in *IEEE Global Conf. Signal and Inf. Process.*, Dec. 2013, pp. 285–288, doi: 10.1109/GlobalSIP.2013.6736871.

[33] R. Krenz and S. Brahma, "Jamming LTE signals," in *IEEE Int. Black Sea Conf. Commun. and Netw. (BlackSeaCom)*, Constanta, Romania, May. 2015, pp. 72–76, doi: 10.1109/BlackSeaCom.2015.7185089.

[34] H. Schmidt and K.-D. Kammeyer, "Quantization and its effects on OFDM concepts for wireless indoor applications," in *Proc. 4th Int. OFDM Workshop (InOWo)*, Hamburg, Germany, Sep. 1999.

[35] D. Dardari, "Joint clip and quantization effects characterization in OFDM receivers," in *IEEE Trans. Circuits and Syst. I: Regular Papers*, vol. 53, no. 8, pp. 1741–1748, Aug. 2006.

[36] M. Sawada, H. Okada, T. Yamazato, and M. Katayama, "Influence of ADC nonlinearity on the performance of an OFDM receiver," in *IEICE Trans. Commun.*, vol. E89-B, no. 12, pp. 3250–3256, Dec. 2006.

[37] H. Ehm, S. Winter, and R. Weigel, "Analytic quantization modeling of OFDM signals using normal Gaussian distribution," in *Asia-Pacific Microw. Conf.*, Yokohama, Japan, Dec. 2006, pp. 847–850.

[38] H. Yang, T. C. W. Schenk, P. F. M. Smulders and E. R. Fledderus, "Joint impact of quantization and clipping on single- and multi-carrier block transmission systems," in *IEEE Wireless Commun. and Netw. Conf. (WCNC)*, Las Vegas, NV, USA, Mar. 2008, pp. 548–553.

[39] H. Aldoseri, L. Häring, and A. Czylwik, "Analysis of ADC quantization and clipping effects on CDMA-OQAM-OFDM based WSAN," in *Int. J. of Interdisciplinary Telecommun. and Netw. (IJITN)*, vol. 14, no. 1, 2022.

[40] R. Nissel, "Filter bank multicarrier modulation for future wireless systems," Ph.D. dissertation, TU Wien, Vienna, Austria, Dec. 2017.

[41] K. W. Barlee, R. W. Stewart, L. H. Crockett, and N. C. MacEwen, "Rapid prototyping and validation of FS-FBMC dynamic spectrum radio with simulink and ZynqSDR," in *IEEE Open J. Commun. Soc.*, vol. 2, pp. 113–131, Jan. 2021, doi: 10.1109/OJCOMS.2020.3039928.

[42] A. Kaushik et al., "Spectrum sharing for 5G wireless systems (spectrum sharing challenge)," in *Proc. IEEE Int. Symp. Dynamic Spectr. Access Netw. (DySPAN)*, Stockholm, Sweden, Oct. 2015, pp. 1–2.

[43] F. Wunsch, S. Koslowski, S. Müller, N. Cuervo, and F. K. Jondral, "A cognitive overlay system based on FBMC," in *Proc. IEEE Int. Symp. Dynamic Spectr. Access Netw. (DySPAN)*, Baltimore, MD, USA, Mar. 2017, pp. 1–2.

[44] H. Aldoseri, T. Wu, and A. Czylwik, "A practical implementation of spread FBMC in a multitone jamming scenario using USRP radios," in *15th Int. Congr. Ultra Modern Telecommun. and Control Syst. and Workshops (ICUMT)*, Ghent, Belgium, Nov. 2023, pp. 81–84.

[45] M. L. Doelz, E. T. Heald, and D. L. Martin "Binary data transmission techniques for linear systems," in *Proc. IRE*, vol. 45, May 1957. pp. 656–661.

[46] J. G. Proakis, *Digital Communications*, McGraw-Hill, NY, USA, 2008.

[47] R. W. Chang, "Synthesis of band-limited orthogonal signals for multichannel data transmission," in *Bell Syst. Tech. J.*, vol. 45, pp. 1775–1796, Dec. 1966.

[48] B. R. Saltzberg, "Intersymbol interference error bounds with application to ideal bandlimited signaling," in *IEEE Trans. Inf. Theory*, vol. IT-14, pp. 563–568, Dec. 1968.

[49] A. Goldsmith, *Wireless Communications*, Cambridge, UK: Cambridge University Press, 2005.

[50] C. Chang, "Spectrally precoded OFDM," in *IEEE Trans. Commun.*, vol. 54, no. 12, pp. 2173–2185, Dec. 2006.

[51] A. Czylwik, "Adaptive OFDM for wideband radio channels," in *Proc. IEEE Global Commun. Conf. (GLOBECOM)*, vol. 1, London, UK, Nov. 1996, pp. 713–718.

[52] B. Le Floch, M. Alard, and C. Berrou, "Coded orthogonal frequency division multiplex," in *Proc. IEEE*, vol. 83, No. 6, pp. 982–996, Jun. 1995.

[53] S. -W. Lei and V. K. N. Lau, "Performance analysis of adaptive interleaving for OFDM systems," in *IEEE Trans. Veh. Technol.*, vol. 51, no. 3, pp. 435–444, May 2002.

[54] Z. Iqbal, S. Nooshabadi, abd H. Lee, "Analysis and design of coding and interleaving in a MIMO-OFDM communication system," in *IEEE Trans. Consum. Electron.*, vol. 58, no. 3, pp. 758–766, Aug. 2012.

[55] R. van Nee and R. Prasad, *OFDM for Wireless Multimedia Communications*, Norwood, MA, USA: Artech House, 2000.

[56] R. R. Moiser and R. G. Clabaugh, "Kineplex: a bandwidth efficient binary transmission system," in *AIEE Trans.*, vol. 76, pp. 723–728, Jan. 1958.

[57] M. S. Zimmermann and A. L. Kirsch, "The AN/GSC-10 (KATHRYN) variable rate data modem for HF radio," in *IEEE Trans. Commun.*, vol. COM-15, pp. 197–205, Apr. 1967.

[58] G. C. Porter, "Error distribution and diversity performance of a frequency differential PSK HF radio," in *IEEE Trans. Commun.*, vol. COM-16, pp. 567–575, Aug. 1968.

[59] "Orthogonal frequency division multiplexing," U.S. Patent No. 3,488,4555, Jan. 1970.

[60] S. B. Weinstein and P. M. Ebert, "Data transmission by frequency domain multiplexing using the discrete Fourier transform," in *IEEE Trans. Commun.*, vol. COM-19, pp. 628–634, Oct. 1971.

[61] R. E. Blahut, *Fast Algorithms for Digital Signal Processing*, Reading, MA, USA: Addison Wesley Longman, Sep. 1985.

[62] B. Muquet, Z. Wang, G. B. Giannakis, M. de Courville, and P. Duhamel, "Cyclic prefixing or zero padding for wireless multicarrier transmissions?," in *IEEE Trans. Commun.*, vol. 50, no. 12, pp. 2136–2148, Dec. 2002.

[63] B. Muquet, M. de Courville, P. Duhamel, G. B. Giannakis, and P. Magniez, "Turbo demodulation of zero-padded OFDM transmissions," in *IEEE Trans. Commun.*, vol. 50, no. 11, pp. 1725–1728, Nov. 2002.

[64] P. D. Papadimitriou and C. N. Georghiades, "Zero-padded OFDM with improved performance over multipath channels," in *IEEE Consum. Commun. and Netw. Conf. (CCNC)*, Las Vegas, NV, USA, Jan. 2004, pp. 31–34.

[65] W. Ozan, R. Grammenos, and I. Darwazeh, "Cyclic prefixing or zero padding: evaluation for non-orthogonal signals," in *IEEE Commun. Lett.*, vol. 24, no. 3, pp. 690–694, Mar. 2020.

[66] Y. S. Cho, J. Kim, W. Y. Yang, C. G. Kang, *MIMO-OFDM Wireless Communications with MATLAB*, Singapore: Wiley & Sons (Asia), 2010.

[67] R. W. Lucky, "Automatic equalization for digital communication," in *Bell Syst. Tech. J.*, vol. 44, pp. 547–588, Dec. 1965.

[68] A. Peled and A. Ruiz, "Frequency domain data transmission using reduced computational complexity algorithms," in *Proc. IEEE Int. Conf. Acoust., Speech, and Signal Process. (ICASSP)*, Denver, CO, USA, Apr. 1980, vol. 5, pp. 964–967.

[69] F. Classen and H. Meyr, "Frequency synchronization algorithm for OFDM system suitable for communication over frequency selective fading channels," in *IEEE 44th Veh. Technol. Conf. (VTC)*, Stockholm, Sweden, Jun. 1994, vol. 3, pp. 1655–1659.

[70] P. H. Moose, "A technique for orthogonal frequency division multiplexing frequency offset correction," in *IEEE Trans. Commun.*, vol. 42, pp. 2908–2914, Oct. 1994.

[71] M. H. Hsieh and C. H. Wei, "A low complexity frame synchronization and frequency offset compensation scheme for OFDM systems over fading channels," in *IEEE Trans. Commun.*, vol. 48, no. 12, pp. 1596–1609, Sep. 1999.

[72] H. Bölcskei, "Blind estimation of symbol timing and carrier frequency offset in wireless OFDM systems," in *IEEE Trans. Commun.*, vol. 49, no. 6, pp. 988–999, Jun. 2001.

[73] T. M. Schmidl and D. C. Cox, "Robust time and frequency synchronization for OFDM," in *IEEE Trans. Commun.*, vol. 45, no. 12, pp. 1613–1621, Dec. 1997.

[74] F. Daffara and O. Adami, "A new frequency detector for orthogonal multicarrier transmission techniques," in *IEEE 45th Veh. Technol. Conf. (VTC)*, Chicago, IL, USA, Jul. 1995, vol. 2, pp. 804–809.

[75] K. G. Patterson and V. Tarokh, "On the existence and construction of good codes with low peak-to-average power ratios ," in *IEEE Trans. Inf. Theory*, vol. 46, no. 6, pp. 1974–1987, Sep. 2000.

[76] T. A. Wilkinson and A. E. Jones, "Minimization of the mean-to-peak envelope power ratio of multicarrier transmission scheme by block coding," in *IEEE 45th Veh. Technol. Conf. (VTC)*, Chicago, IL, USA, Jul. 1995, vol. 2, pp. 825–829.

[77] X. Li and L. J. Cimini, "Effects of clipping and filtering on the performance of OFDM," in *IEEE 47th Veh. Technol. Conf. (VTC)*, Phoenix, AZ, USA, May 1997, vol. 3, pp. 1634–1638.

[78] D. Galda and H. Rohling, "A low complexity transmitter structure for OFDM-FDMA uplink systems," in *IEEE 55th Veh. Technol. Conf. (VTC Spring)*, Birmingham, AL, USA, May 2002, vol. 55, no. 4, pp. 1737–1741.

[79] D. Chen, Y. Tian, D. Qu, and T. Jiang, "OQAM-OFDM for wireless communications in future internet of things: a survey on key technologies and challenges," in *IEEE Internet of Things J.*, vol. 5, no. 5, pp. 3788–3809, Oct. 2018.

[80] B. Farhang-Boroujeny, "OFDM versus filter bank multicarrier," in *IEEE Signal Process. Mag.*, vol. 28, no. 3, pp. 92–112, May 2011.

[81] B. R. Saltzberg, "Performance of an efficient parallel data transmission system," in *IEEE Trans. Commun. Technol.*, vol. 15, no. 6, pp. 805–811, Dec. 1967.

[82] M. Bellanger and J. Daguet, "TDM-FDM transmultiplexer: digital polyphase and FFT," in *IEEE Trans. Commun.*, vol. 22, no. 9, pp. 1199–1205, Sep. 1974.

[83] R. Bruce Kieburtz, "Introduction to papers on TDM/FDM transmultiplexers," in *IEEE Trans. Commun.*, vol. 26, no. 5, pp. 697–698, May 1978.

[84] A. Şahin, İ. Güvenç, and H. Arslan "A survey on multicarrier communications: prototype filters, lattice structures, and implementation aspects," in *IEEE Commun. Surv. and Tut.*, vol. 16, no. 3, pp. 1312–1338, Third Quarter 2014.

[85] B. Boashash, Ed., *Time-Frequency Signal Analysis and Processing: A Comprehensive Reference*, UK: Elsevier Academic Press, 2015.

[86] M. Vitterli, J. Kovacevic, and V. K. Goyal, *Foundations of Signal Processing*, UK: Cambridge University Press, 2014.

[87] J. Du and S. Signell, "Pulse shape adaptivity in OFDM/OQAM systems," in *Proc. Int. Conf. Adv. Infocomm Technol. (ICAIT)*, Shen Zhen, China, Jul. 2008, pp. 109–113.

[88] R. Haas and J.-C. Belfiore, "A time-frequency well-localized pulse for multiple carrier transmission,," in *Wireless Pers. Commun.*, vol. 5, no. 1, pp. 1–18, Jul. 1997.

[89] B. Hirosaki, "An orthogonally multiplexed QAM system using the discrete Fourier transform," in *IEEE Trans. Commun.*, vol. 29, no. 7, pp. 982–989, Jul. 1981.

[90] H. Bölcskei, "Orthogonal frequency division multiplexing based on offset QAM," in *Advances in Gabor Analysis*, H.G. Feichringer, T. Strohmer, Eds. Boston, MA: Birkhäuser, 2003, pp. 351–352.

[91] B. Farhang-Boroujeny, "Multicarrier modulation with blind detection capability using cosine modulated filter banks," in *IEEE Trans. Commun.*, vol. 51, no. 12, pp. 2057–2070, Dec. 2003.

[92] T. Jiang, D. Chen, C. Ni, and D. Qu, "Orthogonal frequency division multiplexing based on offset QAM," in *OQAM/FBMC for Future Wireless Communications: Principles, Technologies and Applications*, Cambridge, MA, USA: Elsevier, 2017.

[93] A. Viholainen, M. Bellanger, and M. Huchard, "Deliverable 5.1: prototype filter and structure optimization," Physical layer for Dynamic spectrum access and cognitive radio (PHYDYAS), Jan. 2009.

[94] P. Siohan, C. Siclet, and N. Lacialle, "Analysis and design of OFDM/OQAM systems based on filterbank theory," in *IEEE Trans. Signal Process.*, vol. 50, pp. 1170–1183, May 2002.

[95] A. Viholainen, T. Ihalainen, T. H. Stitz, M. Renfors, and M. Bellanger, "Prototype filter design for filter bank based multicarrier transmission," in *17th Eur. Signal Process. Conf. (EUSIPCO)*, Glasgow, Scotland, UK, Aug. 2009. pp. 1359–1363.

[96] H. Bölcskei, P. Duhamel, and R. Hleiss, "Design of pulse shaping OFDM/OQAM systems for high data-rate transmission over wireless channels," in *Proc. IEEE Int. Conf. Commun. (ICC)*, vol. 1, Vancouver, Canada, Jun. 1999, pp. 559–564.

[97] H. M. Abdel-Atty, W. A. Raslan, A. T. Khalil, "Evaluation and analysis of FBM-C/OQAM systems based on pulse shaping filters," in *IEEE Acsess*, vol. 8, pp. 55750–55772, Mar. 2020.

[98] C. Roche and P. Siohan, "A family of extended Gaussian functions with a nearly optimal localization property," in *Proc. Int. Workshop Multi- Carrier Spread-Spectrum (MC-SS)*, Germany, Apr. 1997, pp. 179–186.

[99] P. Siohan and C. Roche, "Cosine-modulated filterbanks based on extended gaussian functions," *IEEE Trans. Signal Process.*, vol. 48, pp. 3052–3061, Nov. 2000.

[100] J. Du, "Pulse shape adaptation and channel estimation in generalised frequency division multiplexing," Ph.D. dissertation, KTH Royal Institute of Technology, Stockholm, Sweden, Dec. 2008.

[101] K. Martin, "Small side-lobe filter design for multitone data communication applications," in *IEEE Trans. Circuits and Syst. II: Analog and Digital Signal Process.*, vol. 45, no. 8, pp. 1155–1161, Aug. 1998.

[102] M. G. Bellanger, "Specification and design of a prototype filter for filter bank based multicarrier transmission," in *Proc. IEEE Int. Conf. Acoust., Speech, and Signal Process. (ICASSP)*, Salt Lake City, UT, USA, vol. 4, May 2001, pp. 2417–2420.

[103] S. Mirabbasi and K. Martin, "Design of prototype filter for near-perfect-reconstruction overlapped complex-modulated transmultiplexers," in *Proc. IEEE Int. Symp. Circuits and Syst. (ISCAS)*, Phoenix, AZ, USA, vol. 1, 2002, pp. 821–824.

[104] S. Mirabbasi and K. Martin, "Overlapped complex-modulated transmultiplexer filters with simplified design and superior stopbands," in *IEEE Trans. Circuits and Syst. II: Analog and Digital Signal Process.*, vol. 50, no. 8, pp. 456–469, Aug. 2003.

[105] A. Vahlin and N. Holte, "Optimal finite duration pulses for OFDM," in *Proc. IEEE Global Commun. Conf. (GLOBECOM)*, San Francisco, CA, USA, Nov. 1994, pp. 258–262.

[106] G. Nigam, R. Singh, and A. Chaturvedi, "Finite duration root Nyquist pulses with maximum in-band fractional energy," in *IEEE Commun. Lett.*, vol. 14, no. 9, pp. 797–799, Sep. 2010.

[107] P. R. Chevillat and G. Ungerboeck, "Optimum FIR transmitter and receiver filters for data transmission over band-limited channels," in *IEEE Trans. Commun.*, vol. 30, pp. 1909–1915, Aug. 1982.

[108] M. Bellanger, "FS-FBMC: An alternative scheme for filter bank based multicarrier transmission," in *Proc. 5th Int. Symp. Commun., Control and Signal Process.*, Rome, Italy, May 2012, pp. 1–5.

[109] M. Bellanger, "FBMC Physical layer: a primer," Physical layer for Dynamic spectrum access and cognitive radio(PHYDYAS), Jun. 2010.

[110] M. Bellanger, "Efficiency of filter bank multicarrier techniques in burst radio transmission," in *Proc. IEEE Global Commun. Conf. (GLOBECOM)*, Miami, FL, USA, Dec. 2010, pp. 1–4.

[111] M. J. Abdoli, M. Jia, and J. Ma, "Weighted circularly convolved filtering in OFDM/OQAM," in *IEEE 24th Annu. Int. Symp. Pers., Indoor, and Mobile Radio Commun. (PIMRC)*, London, UK, Sep. 2013, pp. 657–661.

[112] B. Hirosaki, "An analysis of automatic equalizers for orthogonally multiplexed QAM systems," in *IEEE Trans. Commun.*, vol. 28, no. 1, pp. 73–83, Jan. 1980.

[113] G. Lin, L. Lundheim, and N. Holte, "On efficient equalization for OQAM/OFDM systems," in *Proc. Int. OFDM Workshop (InOWo)*, Hamburg, Germany, Aug. 2005, pp. 1–5.

[114] R. Nissel, S. Schwarz, and M. Rupp, "Filter bank multicarrier modulation schemes for future mobile communications," in *IEEE J. Selected Areas in Commun.*, vol. 35, no. 8, pp. 1768–1782, Aug. 2017.

[115] T. Ihalainen, T. H. Stitz, M. Rinne, and M. Renfors, "Channel equalization in filter bank based multicarrier modulation for wireless communications," in *EURASIP J. Adv. in Signal Process.*, vol. 2007, pp. 1–18, Dec. 2006, doi: 10.1155/2007/49389.

[116] D. S. Waldhauser, L. G. Baltar, and J. A. Nossek, "MMSE subcarrier equalization for filter bank based multicarrier systems," in *IEEE 9th Workshop Signal Process. Adv. in Wireless Commun. (SPAWC)*, Recife, Brazil, Jul. 2008, pp. 525–529.

[117] M. Caus, A. I. Perez-Neira, and A. Kliks, "Characterization of the effects of multi-tap filtering on FBMC/OQAM systems," in *EURASIP J. Adv. in Signal Process.*, vol. 2014, pp. 1–15, Jun. 2014.

[118] L. Marijanovic, S. Schwarz, and M. Rupp, "MMSE equalization for FBMC transmission over doubly-selective channels," in *IEEE 13th Int. Symp. Wireless Commun. Syst. (ISWCS)*, Poznan, Poland, Sept. 2016, pp. 170–174.

[119] R. Nissel, M. Rupp, and R. Marsalek, "FBMC-OQAM in doubly-selective channels: A new perspective on MMSE equalization," in *IEEE 9th Workshop on Signal Process. Adv. in Wireless Commun. (SPAWC)*, Hokkaido, Japan, Jul. 2017, pp. 1–5.

[120] H. Lin, C. Lélé, and P. Siohan, "Equalization with interference cancellation for Hermitian symmetric OFDM/OQAM systems," in *IEEE Int. Symp. Power Line Commun. and its Appl. (ISPLC)*, Jeju, South Korea, Apr. 2008, pp. 363–368.

[121] J.-P. Javaudin, D. Lacroix, and A. Rouxel, "Pilot-aided channel estimation for OFDM/OQAM," in *IEEE 55th Veh. Technol. Conf. (VTC Spring)*, vol. 3, Jeju, South Korea, Apr. 2008, pp. 1581–1585.

[122] C. Lélé, J. Javaudin, R. Legouable, A. Skrzypczak, and P. Siohan, 'Channel estimation methods for preamble-based OFDM/OQAM modulations" in *Eur. Trans. Telecommun.*, vol. 19, no. 7, pp. 741–750, Sep. 2008.

[123] J.-M. Choi, Y. Oh, H. Lee, and J.-S. Seo, "Pilot-aided channel estimation utilizing intrinsic interference for FBMC/OQAM systems," in *IEEE Trans. Broadcast*, vol. 63, no. 4, pp. 644–655, Dec. 2017.

[124] H. Bölcskei, P. Duhamel, and R. Hleiss, "A subspace-based approach to blind channel identification in pulse shaping OFDM/OQAM systems," in *IEEE Trans. Signal Process.*, vol. 49, no. 7, pp. 1594–1598, Jul. 2001.

[125] V. Savaux, J. Palicot, and F. Bader, "OFDM/OQAM blind equalization using CNA approach," in *IEEE Trans. Signal Process.*, vol. 64, no. 9, pp. 2324–2333, May 2016.

[126] R. Nissel and M. Rupp, "Enabling low-complexity MIMO in FBMC-OQAM," in *IEEE Global Commun. Conf. (GLOBECOM) Workshops*, Washington DC, USA, Dec. 2016, pp. 1–6.

[127] R. Nissel, E. Zöchmann, M. Lerch, S. Caban, and M. Rupp, "Low-latency MISO FBMC-OQAM: it works for millimeter waves!," in *IEEE/MTT-S Int. Microw. Symp. (IMS)*, Honolulu, Hawaii, Jun. 2017, pp. 673–676.

[128] K. Fazel and S. Kaiser, *Multi-Carrier and Spread Spectrum Systems: From OFDM and MC-CDMA to LTE and WiMAX*, Chichester, UK: Wiley, 2008.

[129] F. Perez Fontan and P. Marino Espineira, *Modelling the Wireless Propagation Channel: A Simulation Approach with MATLAB*, Chichester, UK: Wiley, 2008.

[130] A. A. M. Saleh and R. A. Valenzuela, " A statistical model for indoor multipath propagation," in *IEEE J. Sel. Areas in Commun.*, vol. 5, no. 2, pp. 128–137, Feb. 1987.

[131] Y. Ai, M. Cheffena, and Q. Li, "Power delay profile analysis and modeling of industrial indoor channels," in *9th Eur. Conf. Antennas and Propag. (EuCAP)*, Portugal, Apr. 2015, pp. 1–5.

[132] M. Kyrö, K. Haneda, J. Simola, K.-i. Takizawa, H. Hagiwara, and P. Vainikainen, "Statistical channel models for 60 GHz radio propagation in hospital environments," in *IEEE Trans. Antennas and Propag.*, vol. 60, no. 3, pp. 1569–1577, Mar. 2012.

[133] E. Tanghe, W. Joseph, J. D. Bruyne, L. Verloock, and L. Martens, "The industrial indoor channel: Statistical analysis of the power delay profile," in *AEU-Int. J. Electron. and Commun.*, vol. 64, no. 9, pp. 806–812, Sep. 2010.

[134] D. Na and K. Choi, "Low PAPR FBMC," in *IEEE Trans. Wireless Commun.*, vol. 17, no. 1, pp. 182–193, Jan. 2018.

[135] *Analog-Digital Conversion*, Analog Devices, USA, Mar. 2004.

[136] M. Bi et al., "Study of FFT/IFFT precision in optical OQAM-OFDM system with limited resolution DAC/ADC," in *Asia Commun. and Photon. Conf. (ACP)*, Wuhan, China, Nov. 2016, pp. 1–3.

[137] N. Varghese, J. Chunkath, and V. S. Sheeba, "Peak-to-average power ratio reduction in FBMC-OQAM system," in *4th Int. Conf. Adv. in Comput. and Commun.*, Cochin, India, Aug. 2014, pp. 286–290.

[138] S. Eldessoki, J. Dommel, K. Hassan, L. Thiele, and R. F. H. Fischer, "Peak-to-average-power reduction for FBMC-based systems," in *20th Int. ITG Workshop on Smart Antennas (WSA)*, Munich, Germany, Mar. 2016, pp. 1–6.

[139] S. S. K. C. Bulusu, "Performance analysis and PAPR reduction techniques for filter-bank based multi-carrier systems with non-linear power amplifiers," Ph.D. dissertation, Conservatoire National des Arts et Metiers (CNAM), Paris, France, Apr. 2016.

[140] Z. Kollar, L. Varga, and K. Czimer, "Clipping-based iterative PAPR-reduction techniques for FBMC," in *17th Int. OFDM Workshop 2012 (InOWo)*, Essen, Germany, Aug. 2012, pp. 1–7.

[141] M. Smolnikar, M. Mohorcic, H. Gacanin, and F. Adachi, "Impact of quantization on channel estimation in OFDM communication system," in *12th Int. Symp. Wireless Pers. Multimedia Commun. (WPMC 09)*, Sendai, Japan, Sep. 2009.

[142] B. M. Murray and I. B. Collings, "AGC and quantization effects in a zero-forcing MIMO wireless system," in *2006 IEEE 63rd Veh. Technol. Conf.*, vol. 4, Melbourne, Australia, May 2006, pp. 1802–1806.

[143] R. Rietman and J.-P. Linnartz, "Peak restoration in OFDM receiver with clipping A/D converter," in *IEEE Trans. Wireless Commun.*, vol. 7, no. 12, pp. 5177–5181, Dec. 2008.

[144] A. Gersho and R. M. Gray, *Vector Quantization and Signal Compression*, Norwell, MA, USA: Kluwer, 1992.

[145] R. F. Ormondroyd and E. Al-Susa, "Impact of multipath fading and partial-band interference on the performance of a COFDM/CDMA modulation scheme for robust wireless communications," in *Proc. IEEE Mil. Commun. Conf. (MILCOM)*, Boston, MA, USA, vol. 2, Oct. 1998, pp. 673–678.

[146] C. Thein, M. Fuhrwerk, and J. Peissig, "Frequency-domain processing for synchronization and channel estimation in OQAM-OFDM systems," in *IEEE 14th Int. Workshop Signal Process. Adv. in Wireless Commun. (SPAWC)*, Toronto, ON, Canada, Jun. 2013, pp. 634–638.

[147] National Instruments, "Product Flyer - USRP Software Defined Radios" Aug. 2019.[Online]. Available: https://ni.com/pdf/product-flyers/usrp-software-defined-radio.pdf

[148] Ettus Research, 2017.[Online]. Available: https://files.ettus.com/schematics/n200

[149] Ettus Research, Nov. 2019.[Online]. Available: https://kb.ettus.com/SBX

[150] Hittite Microwave Corporation, "HMC624LP4/624LP4E: 0.5 dB LSB GaAs MMIC 6-bit digital attenuator, DC - 6 GHz," HMC624LP4/624LP4E Datasheet, 2017.

[151] C. Thein, "A frequency domain approach to synchronization of filterbank multicarrier systems in practice," Dr.-Ing. dissertation, Gottfried Wilhelm Leibniz Universität, Hannover, Germany, 2015.

[152] H. Almujahed, "MIMO OQAM-OFDM-based radio transmission system using LabVIEW," M.-Ing. thesis, Nachrichtentechnische Systeme (NTS), Universität Duisburg-Essen, Duisburg, Germany, Jan. 2019.

[153] T. Wu, "Implementation of CDMA-OQAM-OFDM transmission chain using USRP radios," M.-Ing. thesis, Nachrichtentechnische Systeme (NTS), Universität Duisburg-Essen, Duisburg, Germany, Aug. 2019.

[154] Analog Devices, Appl. Note-1507, Oct. 2004 [Revised Nov. 2017].

[155] Analog Devices, "AD8318: 1 MHz to 8 GHz, 70dB logarithmic controller/detector," AD8318 Datasheet, Jul. 2004 [Revised Dec. 2017].

[156] F. Bastide, D. Akos, C. Macabiau, and B. Roturier, "Automatic gain control (AGC) as an interference assessment tool," in *16th Int. Tech. Meeting Satell. Division Inst. of Navigation*, Portland, OR, USA, Sep. 2003, pp. 2042–2053.

[157] T. Lotz, "Adaptive analog-to-digital conversion and pre-correlation interference mitigation techniques for a GNSS receiver," Diplomarbeit, Technische Universität Kaiserslautern, Kaiserslautern, Germany, Nov. 2008.

[158] R. J. R. Thompson, E. Cetin, and A. G. Dempster, "Detection and jammer-to-noise estimation of interferers using the automatic gain control," in *Int. Global Navigation Satell. Syst. (IGNSS) Symp.*, Sydney, Australia, Nov. 2011.

[159] S. Koslowski, "Synchronisation und entzerrung in filterbank multicarrier-empfängern," (in German), Dr.-Ing. dissertation, Inst. für Nachrichtentechnik, Karlsruher Institut für Technologie, Karlsruhe, Germany, May 2018.

[160] K. W. Barlee, "Design and implementation of real-time cognitive dynamic spectrum radio, targeting the FM radio band with PHYDYAS FS-FBMC," Ph. D. dissertation, Dept. Electron. and Elect. Eng., University of Strathclyde, Strathclyde, Scotland, UK, Jan. 2021.

[161] J. P. A. Pérez, S. C. Pueyo, and B. C. Lopez, *Automatic Gain Control: Techniques and Architectures for RF Receivers*, New York, NY, USA: Springer, 2001.

[162] Analog Devices, "ADL5380: 400 MHz to 6 GHz quadrature demodulator," ADL5380 Datasheet, Jul. 2009 [Revised Dec. 2014].

List of Abbreviations

ADC	Analog-to-Digital Converter
AGC	Automatic Gain Control
ATJ	All Tone Jamming
AWGN	Additive White Gaussian Noise
BER	Bit Error Ratio
BNJ	Barrage Noise Jamming
BPF	Bandpass Filter
CCDF	Complementary Cumulative Distribution Function
CDMA	Code Division Multiple Access
CF	Clipping Factor
CFO	Carrier Frequency Offset
CIR	Channel Impulse Response
CP	Cyclic Prefix
CTF	Channel Transfer Function
DAC	Digital-to-Analog Converter
DC	Downconversion
DFT	Discrete Fourier Transform
DoS	Denial of Service
DSB	Double Sideband
DS	Direct Sequence
EGF	Extended Gaussian Function
ENOB	Effective Number Of Bits
EVM	Error Vector Magintude
EW	Electronic Warefare
FBMC	Filter Bank Multicarrier
FFT	Fast Fourier Transform
FPGA	Field Programmable Gate Array
FS	Frequency Spreading

GPS	Global Positioning System
HF	High Frequency
IBO	Input Back-Off power ratio
ICI	Inter Carrier Interference
IDFT	Inverse Discrete Fourier Transform
IFFT	Inverse Fast Fourier Transform
IoT	Internet of Things
IOTA	Isotropic Orthogonal Transform Algorithm
ISI	Inter Symbol Interference
JSR	Jammer-to-Signal Power Ratio
LOS	Line-Of-Sight
LPF	Low-Pass Filter
LTE	Long Term Evolution
MAI	Multiple Access Interference
MC	Multicarrier
MIMO	Multiple-Input Multiple-Output
ML	Maximum Likelihood
MMSE	Minimum Mean Squared Error
MOTJ	Multi Off-Tone Jamming
MTJ	Multitone Jamming
NLOS	Non-Line-Of-Sight
OBO	Output Back-Off power ratio
OFDM	Orthogonal Frequency Division Multiplexing
OFDP	Optimal Finite Duration Pulse
OOB	Out-Of-Band
OQAM	Offset Quadrature Amplitude Modulation
PA	Power Amplifier
PAM	Pulse Amplitude Modulation
PAPR	Peak-to-Average Power Ratio
PBJ	Partial Band Jamming
PDF	Probability Density Function
PHY	Physical
PHYDYAS	Physical layer for Dynamic spectrum Access and cognitive radio
P-N	Pseudo-Noise
P/S	Parallel-to-Serial

PSD	Power Spectral Density
PSF	Pulse Shaping Filter
PSK	Phase Shift Keying
PUCCH	Physical Uplink Control Channel
QAM	Quadrature Amplitude Modulation
QPSK	Quadrature Phase Shift Keying
RC	Raised Cosine
RF	Radio Frequency
RFHJ	Random Frequency Hopping Jamming
RMS	Root Mean Square
RMTJ	Random Multitone Jamming
RRC	Root Raised Cosine
SC-FDMA	Single Carrier Frequency Division Multiple Access
SDR	Software Defined Radio
SEFDM	Spectrally Efficient Frequency Division Multiplexing
SIR	Signal-to-Interference power Ratio
SMTJ	Sweep Multitone Jamming
SNR	Signal-to-Noise power Ratio
SOTJ	Single Off-Tone Jamming
S/P	Serial-to-Parallel
SQNR	Signal-to-Quantization Noise power Ratio
STJ	Single Tone Jamming
S-V	Saleh-Valenzuela
TO	Time Offset
TS	Time Spreading
UC	Upconversion
URLLC	Ultra Reliable Low Latency Communications
USRP	Universal Software Radio Peripheral
VGA	Variable Gain Amplifier
VSB	Vestigial Sideband
W-H	Walsh-Hadamard
WGN	White Gaussian Noise
WSAN	Wireless Sensor and Actuator Network
ZF	Zero Forcing
ZP	Zero Padding

List of Symbols

Latin

A_{adc}	ADC clipping amplitude
A_{agc}	AGC clipping amplitude
A_{dac}	DAC clipping amplitude
A_{g}	Ambiguity function
$a_{n,k}$	Spread FBMC data
B_{c}	Coherence bandwidth of the channel
B_{s}	System bandwidth
b_{adc}	ADC resolution
b_{dac}	DAC resolution
$\mathbf{c}$	Spreading code vector
D	Number of quantization levels
D_{g}	Delay of the prototype filter
$\mathbf{d}$	Binary data vector
$\mathbf{d}'$	QAM-modulated data vector
$e_{\mathrm{q}}[i]$	Quantization error
f_{c}	Carrier frequency
$G[z]$	Frequency response of the prototype filter
$g[i]$	Impulse response of the prototype filter
H_{s}	System channel transfer function
H_{j}	Jammer channel transfer function
h_{s}	System channel impulse response
h_{j}	Jammer channel impulse response
i	Digital sample index
$j(t)$	Jamming signal
K	Number of OQAM Samples

K_g	Overlapping factor
k	OQAM sample index
L_c	Spreading code length
L_g	Prototype filter length
M	Number of QAM Samples
m	QAM sample index
N	Number of subcarriers
N_e	Set of even subcarriers
N_j	Number of jammed subcarriers
N_o	Set of odd subcarriers
n	Subcarrier index
$P_{\mathrm{T},n_\mathrm{e}}$	Transmitted pilot
P'_{n_e}	Extracted pilot in basic stage
$\hat{P}_{n_\mathrm{e}}$	Extracted pilot in additional stage
p	Walsh-Hadamard matrix order
Q_ad	Quantization function
R	Throughput
$r(t)$	Received signal
$r_\mathrm{d}[i]$	ADC sampled output
$r_\mathrm{dc}(t)$	Downconverted RF received signal
$r_\mathrm{f}(t)$	Filtered downconverted received signal
$r_\mathrm{gc}(t)$	AGC output
$s[i]$	Digital baseband signal
$s(t)$	Transmitted signal
$s_\mathrm{a}(t)$	DAC output
$s_\mathrm{uc}(t)$	Upconverted RF transmitted signal
T_s	Sampling time
T_sym	Symbol time
U	Number of users
u	User index
$w(t)$	AWGN

Greek

α	W-H row (column) index
γ_{js}	JSR
γ_{sn}	SNR
γ_{sq}	SQNR
Δf	Subcarrier spacing
Δn_{s}	FBMC System CFO
Δn_{j}	Jammer CFO
Δk_{s}	FBMC System TO
Δk_{j}	Jammer TO
δ	Kroenecker delta function
η	PAPR
μ_{c}	ADC clipping factor
$\mu_{\mathrm{c,opt}}$	Optimal ADC clipping factor
$\phi_{n,k}$	OQAM phase shift

Mathematical Operators

j	$\sqrt{-1}$
$\|\,\|$	Absolute value
$\angle$	Arctan
$\|\|\,\|\|$	Euclidean Norm
$\circledast$	Circular convolution
$*$	Convolution
$\{\,\}^*$	Complex conjugate
$\mathrm{E}\{\,\}$	Expectation
$\lfloor\,\rfloor$	Floor
$\Im\{\,\}$	Imaginary part
$\mathrm{mod}\,(\,)$	Modulo
$\Pr\{\,\}$	Probability
$\Re\{\,\}$	Real part
$\mathrm{rect}\,(\,)$	Rectangular function
$\{\,\}^T$	Transpose

DuEPublico

Duisburg-Essen Publications online